University of Nevada, Reno

Geophysical Modeling of the Dixie Meadows Geothermal Prospect: Dual Analysis of Gravity and Magnetic Data towards Identifying Structural Controls

A thesis submitted in partial fulfillment of the
requirements for the degree of
Master of Science in Geophysics

by

Paul C. Schwering

Dr. Robert E. Karlin, Thesis Advisor

May, 2013

UNIVERSITY OF NEVADA, RENO

THE GRADUATE SCHOOL

We recommend that the thesis

prepared under our supervision by

Paul C. Schwering

entitled

Geophysical Modeling of the Dixie Meadows Geothermal Prospect: Dual Analysis of

Gravity and Magnetic Data towards Identifying Structural Controls

be accepted in partial fulfillment of the

requirements for the degree of

MASTER OF SCIENCE

Robert E. Karlin, Ph.D., Advisor

Wendy M. Calvin, Ph.D., Committee Member

Patricia H. Cashman, Ph.D., Committee Member

Benjamin T. King, Ph.D., Graduate School Representative

Marsha H. Read, Ph.D., Dean, Graduate School

May, 2013

Preface

The primary findings of this study, detailed in Chapter 2 of this thesis document, will be submitted as an article to the Journal of Volcanology and Geothermal Research. The article will be submitted with the same title as this thesis document. Authors on the paper will be: Paul C. Schwering, Robert E. Karlin, and Patricia H. Cashman of the Department of Geological Sciences and Engineering, University of Nevada, Reno; Wendy M. Calvin of the Great Basin Center for Geothermal Energy, University of Nevada, Reno; Benjamin T. King of the Department of Chemistry, University of Nevada, Reno; and Ashton N. McGill of ARANZ Geo Limited, Christchurch, New Zealand. The article will essentially be a condensed version of Chapter 2. The overall article content will be similar to the content of Chapter 2, although changes are expected as a result of the peer-review process.

~

Abstract

The northern Great Basin has abundant geothermal systems. Studies have shown these systems are structurally controlled by extensional faults. The faults, and sometimes systems themselves, often have little or no surface expression and must therefore be characterized by geophysical methods. The Dixie Meadows geothermal prospect, located within the Humboldt Structural Zone in central Dixie Valley, Nevada, was investigated in this study in order to delineate basin and fault structure that likely control hydrothermal fluid flow in the subsurface. The study focused on dual interpretation and modeling of gravity and magnetic geophysical data, but was also supported by geological reconnaissance and assessment of surficial hydrothermal expressions. Results indicate a concealed piedmont fault zone separates a deep basin from a relatively shallow intra-basin adjacent to the rangefront. Geophysically delineated faults are located in the intra-basin and piedmont fault zones, and have little or no surface expressions. Rangefront, intra-basin, and piedmont faults are interpreted to be moderately- to steeply-dipping. Faults strike in multiple directions, revealing a network of interlinking and interacting faults. Interpreted structural, geophysical, and hydrothermal patterns along the intrabasin and rangefront demarcate a primary geothermal target area and two secondary targets. The primary target area is characterized by advanced argillic alteration at the surface and upflow indicated by two fumarole zones. Fault intersection appears to be the key structural pattern controlling upflow in the target areas, but fault splaying and step-over are also contributing factors. Integration of dual gravity and magnetic models with geological observations indicates three discrete phases of extension have occurred in Cenozoic time. The superposition of normal faults from these extensional phases appears

to be a key component in generating the fault patterns that are controlling hydrothermal fluid flow in the subsurface. The findings of this study are intended to influence further exploration and potential development of the Dixie Meadows geothermal prospect, as well as exemplifying approaches that may aid in discovery, exploration, and development of other prospects in the Humboldt Structural Zone and the Great Basin.

~

Acknowledgements

~

Dedication

This thesis document is dedicated to my wife, Tessa, and to my daughter, Emma. Tessa: the greatest friend, companion, and love of my life. She consistently motivates me to surpass even my own expectations in all of my pursuits, and I am continually inspired by the grace and wisdom she impeccably exhibits in her many achievements. My deepest thanks for the continued love and support during my pursuit of a Master's degree; I could not have done it without you. Emma: the greatest wonder of my life so far. Her arrival profoundly re-invigorated my passion for enjoying the discoveries and mysteries of the human experience. Thank you both for the memories I will cherish forever, and I look forward to all those to come. I love you both with all of my heart, and I always will.

~

Table of Contents

~

List of Figures

~

List of Tables

~

"I think it's much better to start out on something that you're not at all sure that you can do. If you overcome and you manage to defeat the obstacles, the satisfaction is so much greater."

Edmund Hillary

Chapter 1: Introduction

Ongoing expansion of geothermal energy usage in the USA highlights the need for expansion and refinement of geophysical exploration techniques towards geothermal resource development. Historically, geothermal energy production has been limited to locations with discernible surface expressions (e.g., hot springs, fumaroles, sinter terraces) emanating from the underlying geothermal system. However, the utilization of geothermal resources from concealed and enhanced geothermal systems offers immense potential for expanding geothermal production in the USA (Coolbaugh et al., 2006; Faulds et al., 2011; Tester et al., 2006). These resources, and the critical structures that control them, require remote geophysical detection and monitoring techniques prior to, and during, drilling operations and energy production. Geophysical techniques are thus being improved and more widely applied in the geothermal industry in order to discover new resources and enhance productivity from known systems.

The Great Basin, located in the western USA, is abundant in geothermal systems. Great Basin geothermal systems occur primarily in groups of northeast-oriented belts (Faulds et al., 2004) (Figure 1.1). Crustal heat flow in the region is promoted by extensional tectonism. Great Basin geothermal systems, such as Dixie Valley, Rye Patch, Brady's, and Desert Peak (Figure 1.1), are typically controlled by moderately- to steeply- dipping normal faults (Faulds et al., 2011). Detailed geothermal exploration studies of the

Great Basin reveal patterns of extensional and transtensional structures that are most conducive to hosting geothermal systems (Faulds et al., 2011). Furthermore, there is mounting evidence indicating potentially large amounts of undiscovered geothermal reserves (e.g., resources with little or no surface expression) exist in the Great Basin (Coolbaugh et al., 2006; Faulds et al., 2011).
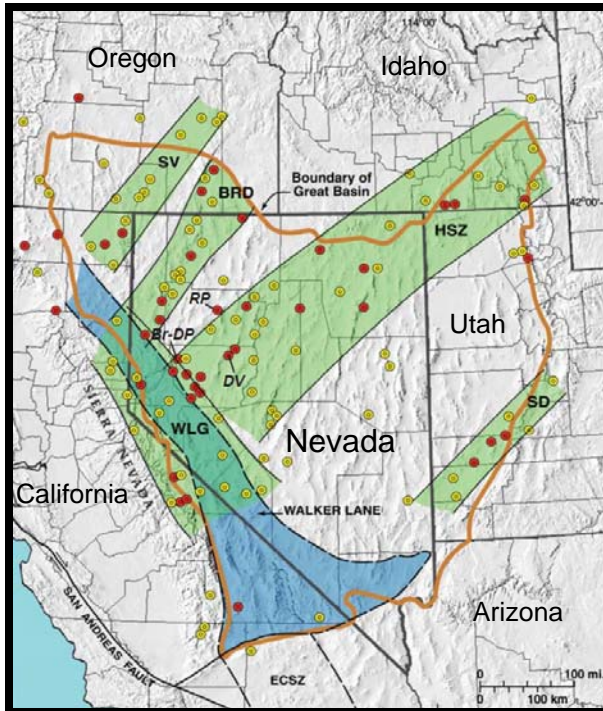
Figure 1.1. Geothermal systems of the Great Basin on a shaded topographic relief map of the western USA, adapted from Faulds et al., 2004. Geothermal systems: yellow and red circles indicating maximum temperatures of 100-160°C and >160°C, respectively. Geothermal belts (green): BRD = Black Rock Desert, HSZ = Humboldt Structural Zone, SD = Sevier Desert, SV = Surprise Valley, WLG = Walker Lane. The Walker Lane structural zone is in blue. Note the location of the Dixie Valley geothermal system (DV) being utilized by the Dixie Valley power plant. Other geothermal systems: Br-DP = Brady's-Desert Peak, RP = Rye Patch.

Dixie Valley is one of the premier study areas of geothermal exploration in the Great Basin, due in large part to anomalously high crustal heat flow expressed by abundant geothermal features. Hot springs, fumaroles, sinter deposits, hydrothermally altered minerals, and active faulting have prompted multiple studies and exploration projects in Dixie Valley since the 1950s. A 60+ MW geothermal power plant (Figures 1.1 and 1.2), in operation since 1988, was established following exploration and development in northern Dixie Valley (Benoit, 1992; Benoit, 1999). The geothermal reservoir is

anomalously hot (285°C @ 3 km depth), relative to other Great Basin geothermal systems (Blackwell et al., 2007). Evolving understanding of the structural controls, significantly aided by contributions from geophysical surveys, has played a critical role in the successful delineation and utilization of this resource (Benoit, 1999; Blackwell et al., 2007; Honjas et al., 1997; Louie et al., 2011; Wannamaker et al., 2007).

Figure 1.2. Picture of the Dixie Valley power plant, looking approximately to the northwest.

The value of geophysical techniques in interpreting the subsurface structure controlling the high-enthalpy system discovered in northern Dixie Valley motivates further exploratory studies in Dixie Valley. Geophysical studies are being utilized to delineate fault structures of geothermal prospects that have little or no surface expression, such as Pirouette Mountain and Eleven Mile Canyon, in southern Dixie Valley (Devriese et al., 2012; Mankhemthong, 2008). Geophysical data is also being integrated into a case study for enhanced/engineered geothermal system exploration in northern Dixie Valley (Iovenitti et al., 2012; Iovenitti et al., 2013).

The following study was conducted on the Dixie Meadows geothermal prospect (Figure 1.3), located in central Dixie Valley, Nevada. Data from gravity and magnetic geophysical surveys, in addition to geologic reconnaissance and hydrothermal surface expression investigation, were interpreted and modeled to delineate subsurface basin geometry and fault architecture. This work provides a testable geologic model and demonstrates the effectiveness of geophysical methods in the identification of geothermal targets and structural controls in the subsurface. Furthermore, it emphasizes the importance of integrated methods in geothermal exploration practices and the role of structural superposition in enhancing geothermal favorability.

Figure 1.3. Picture overlooking the Dixie Meadows geothermal prospect, looking approximately to the east from the Stillwater Mountains. The author is in the foreground. The Dixie Hot Springs are the hottest springs in Dixie Valley, and the Humboldt Salt Marsh is the lowest elevation. The Clan Alpine Mountains form the eastern boundary of the valley.

~

"We like the novelty of giving up what we know, and we like the novelty of coming to know something we did not know. Otherwise, we would just hold on to what we have, and that's not very interesting."

Jasper Johns

Chapter 2: Journal of Volcanology and Geothermal Research Paper

2.1 Introduction

The northern Great Basin is a significant source of renewable geothermal energy. Studies are being performed across the Great Basin to identify the favorable structural settings associated with developed geothermal systems, undeveloped geothermal prospects, and undiscovered potential geothermal resources (e.g., Faulds et al., 2004 and Faulds et al., 2011). Recent studies demonstrate that Great Basin structural controls, even entire geothermal systems/prospects, often have little or no discernible surface expressions (e.g., Coolbaugh et al., 2006 and Faulds et al., 2011). These subsurface resources necessarily must be discovered and assessed remotely. Geophysical methods are key components of the exploration strategies required to characterize subsurface structural controls, chiefly because they are capable of resolving geologic structure in 3D and significantly reduce exploration risks/costs by providing data utilized to guide drilling operations.

The Dixie Meadows geothermal prospect contains various geothermal surface expressions that appear to be controlled by subsurface faults. The prospect is located in the northern Great Basin, ~150 km east-northeast of Reno, Nevada, USA. Hydrothermal

surface expressions include the Dixie Comstock Mine, the Dixie Hot Springs, extensive hydrothermal alteration mineralogy, and two fumarole zones. The Dixie Comstock Mine is an epithermal gold deposit that resulted from Quaternary-aged, intermittent influxes of ore-bearing, hydrothermal fluids (Vikre, 1994). The Dixie Hot Springs are the highest-temperature springs in Dixie Valley and exhibit evidence of structural controls on fluid flow (Bohm et al., 1980; Goff et al., 2002). Argillic and advanced argillic alteration is prevalent in the prospect (Kennedy-Bowdoin et al., 2004; Lamb et al., 2011). The fumaroles are indicative of hydrothermal upflow localized by fault intersections (Kennedy-Bowdoin et al., 2004; Schwering and Karlin, 2012). Previous broad-scale gravity and magnetic geophysical studies indicate that intersecting faults, basinward from the rangefront, are promoting and controlling geothermal fluid flow at Dixie Meadows (Schaefer, 1983; Smith et al., 2002; Smith et al., 2001).

Gravity and magnetic methods are the primary focus of this study. Gravity and magnetic surveys are relatively swift, cost-effective, and environmentally sound means of geophysical data acquisition. They can be executed in the field with relatively mobile equipment, minimal manpower and environmental impact, and precise instrumentation. Though limited by interpretive ambiguities (i.e., non-unique solutions), these methods reduce exploration costs by contributing subsurface information that may aid in planning geothermal well drilling strategies.

Dual forward modeling of gravity and magnetic data profiles is a new method applicable to many facets of geothermal exploration. Skalbeck et al. (2002; 2005) performed dual forward modeling on profiles at the Steamboat Hills geothermal system in order to identify structural controls on hydrologic flow and to estimate geothermal

reservoir volume. Dual forward modeling is also being performed on gravity and magnetic data in northern Dixie Valley as an integral component of developing Engineered Geothermal System (EGS) exploration techniques (Iovenitti et al., 2012; Iovenitti et al., 2013).

The purpose of this study is to conduct detailed analysis and dual modeling of gravity and magnetic data, supported by ancillary data from geologic and hydrothermal surface expression analyses, from the Dixie Meadows geothermal prospect in order to delineate likely subsurface structural controls of hydrothermal fluid flow. This study is presented in an order consistent with geothermal exploration methodology: assessment of hydrothermal surface expressions, followed by geologic reconnaissance at the surface and investigation of available drill cuttings, and concluding with detailed investigation of subsurface structure using gravity and magnetic data. The goal is to create a testable, 3D structural model of the Dixie Meadows subsurface that is more robust and definitive than any previously developed. This study will hopefully guide future geothermal exploration and development at this site, as well as others in the Great Basin.

2.2 Regional and geologic setting

2.2.1 Tectonic and physiographic context

Dixie Meadows is located in central Dixie Valley – an extensional graben located in the northern Great Basin of the western USA (Figure 2.1a). Regional crustal strain is currently characterized by west-northwest-oriented extension (Hammond and Thatcher, 2004; Thompson and Burke, 1973) that initiated 8-10 Ma (Colgan et al., 2004; Fosdick

and Colgan, 2008; Surpless et al., 2002), producing primarily north-northeast-striking normal faults (Faulds et al., 2004) (Figure 2.1a).

Crustal extension of the Great Basin is part of the dynamic tectonic systems of the western USA, illustrated in Figure 2.1b from Faulds et al. (2004). The Pacific and North American plates are in right-lateral strike-slip motion, with respect to each other, along the San Andreas fault zone. Seismologic, geodetic, and geologic studies collectively indicate that ~20% of this motion is accommodated along the northwest-striking, transtensional fault zones in the Walker Lane (Faulds et al., 2004; Hammond et al., 2011). Right lateral shear in the Walker Lane is interpreted to be progressively transferred into the Great Basin along systems of north-northeast-striking normal faults (Faulds et al., 2004). The Walker Lane shear zone merges with the San Andreas system to the south, and terminates into the Cascadian arc to the north. The Sierra Nevada block and the Cascadian arc appear to be a single micro-plate that is decoupling northwestward from the Great Basin (Faulds et al., 2004). The Great Basin, in response to these various tectonic forces, is undergoing predominantly west-northwest-directed extension with respect to the relatively stable Colorado Plateau.
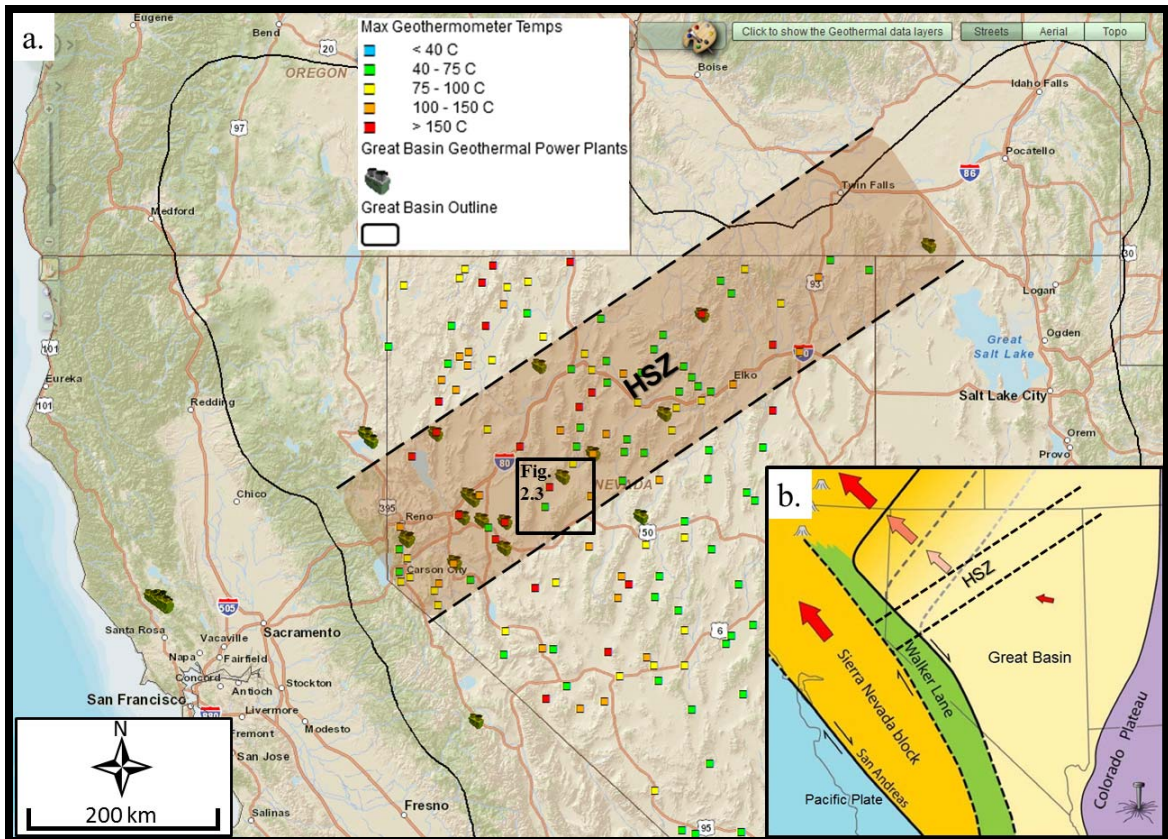
Figure 2.1. (a) Physiographic map of the northern Great Basin. The Great basin boundary is outlined in black. Geothermometer data and power plant locations were obtained from the Nevada Bureau of Mines and Geology. The Humboldt Zone (HSZ) is highlighted and bordered by black dashed lines. (b) Conceptual tectonic diagram of the western USA, adapted from Faulds et al., 2004. The San Andreas fault zone accommodates the majority of the right-lateral slip between the Pacific and North American tectonic plates. ~20% of this motion is accommodated by dextral shear in the Walker Lane. The Walker Lane progressively transfers motion into the north-northeast-trending normal faults of the Great Basin. The Sierra Nevada block and the Cascadian arc to the north appear to be translating northwestward as a single micro-plate. The Great Basin is experiencing primarily west-northwest extension with respect to the "stable" Colorado Plateau. The northeast-trending HSZ contains subsidiary northeast- to east-northeast-striking sinistral-normal faults.

Dixie Valley is incorporated within the Humboldt Structural Zone (HSZ) of Rowan and Wetlaufer (1981). The HSZ is a northeast-trending belt consisting of east-northeast- to northeast-striking sinistral-normal faults that are interlinked with the

dominant north-northeast-striking faults of the northern Great Basin, and are accompanied by a relative abundance of geothermal systems (Faulds et al., 2003; Rowan and Wetlaufer, 1981) (Figures 2.1a and 2.1b). Evolution of the HSZ is not well understood; the subsidiary east-northeast- to northeast-striking faults appear to be an inherited structural fabric, but when and how they initially developed is unknown (J. Faulds, 2013, personal communication). However, the component of left-lateral shear and linkage to north-northeast-striking faults may be invigorating west-northwest directed extension and promoting heat flow within the HSZ (Faulds et al., 2003) (Figure 2.2).
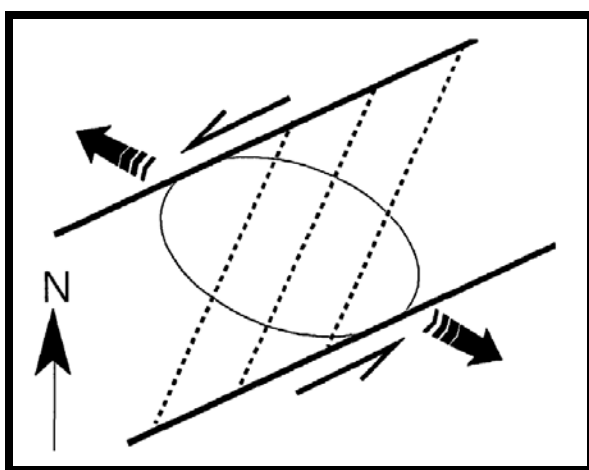
Figure 2.2. Schematic diagram, from Faulds et al. (2003), depicting west-northwest-oriented extension generating a component of left-lateral slip on east-northeast-trending faults. This arrangement may be facilitating extension and stimulating heat flow on north-northeast-trending faults in the Humboldt Structural Zone.

Dixie Valley is bounded to the east by the Clan Alpine Mountains and to the west by the Stillwater Mountains (Figure 2.3), and is the lowest-elevation valley in the northern Great Basin. Dixie Meadows is located on the north-northeast-oriented rangefront margin separating Dixie Valley and the Stillwater Mountains, ~ 25 km southwest of the 60+ MW Dixie Valley power plant (Figure 2.3). The study area includes the Humboldt Salt Marsh (the minimum elevation in Dixie Valley) and >2 km deep geothermal wells 42-9 and 45-14 (Figure 2.3). The eastern face of the Stillwater

Mountains is steep – peaks of the Stillwater Mountains and the Humboldt Salt Marsh are separated by ~1 km of vertical relief.
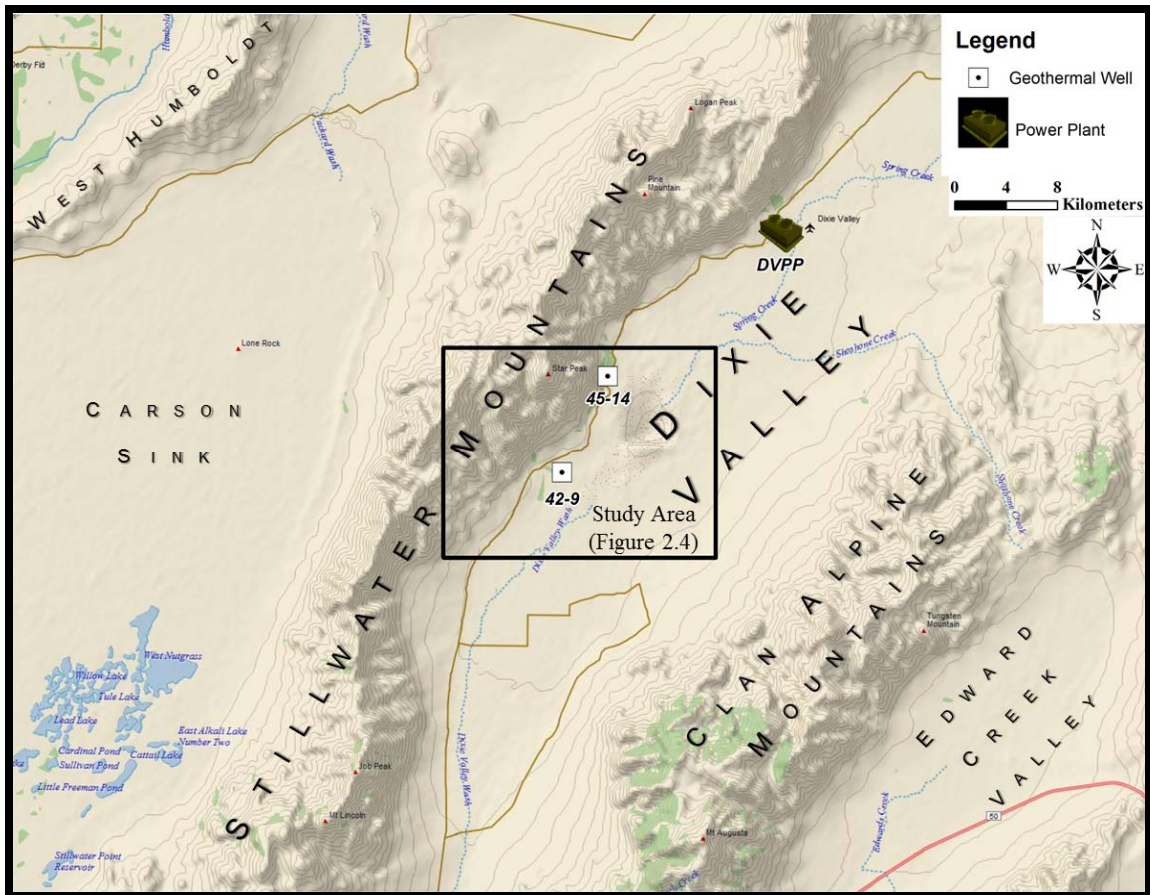
Figure 2.3. Shaded topographic relief map of Dixie Valley and surrounding terrain. The study area is outlined by a black rectangle. Locations of deep geothermal wells 42-9 and 45-14 are shown for reference.

2.2.2 Geologic Units

Figure 2.4 is a geologic map, adapted from Speed (1976), summarizing the geologic units observed at Dixie Meadows. The valley consists of late Tertiary through Quaternary alluvial and lacustrine basin fill sediment successions (Willden and Speed, 1974). Basin fill depths vary from 10s to 100s of meters on the valley margins to more than 2 km in the central valley (Speed, 1976; Waibel, 1987).
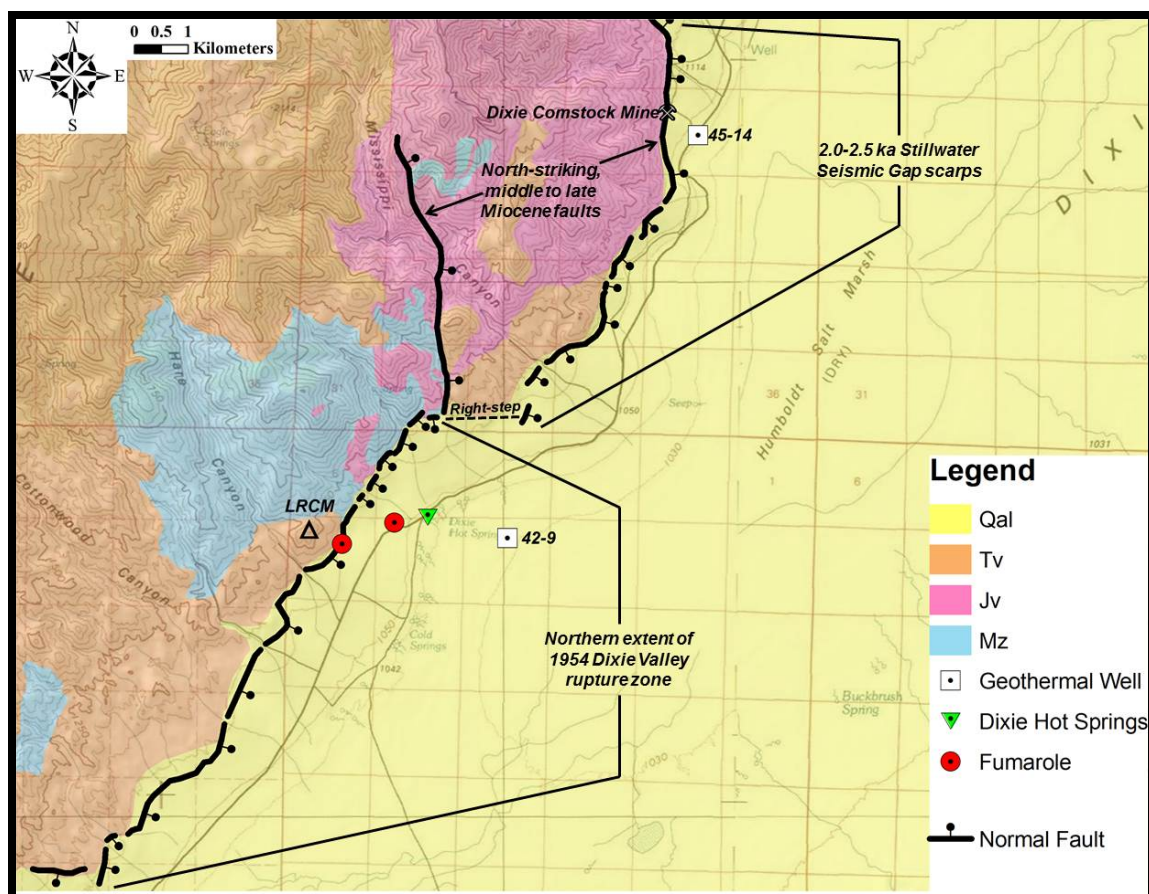
Figure 2.4. Generalized geologic map of the study area, adapted from Speed (1976), overlain on topographic base. Topographic contour lines are in meters. Qal = Quaternary alluvial and lacustrine basin fill, Tv = Tertiary volcanics, Jv = Jurassic volcanics (Humboldt igneous complex), and Mz = Mesozoic Boyer Ranch Formation and Triassic marine sequence. Quaternary fault scarps adapted from Sawyer and Anderson (1999). Right-step inferred between the 1954 Dixie Valley and Stillwater Seismic Gap fault scarps. North-striking, Miocene-aged fault crossing Mississippi Canyon was mapped by Speed (1976). North-striking fault through the Dixie Comstock Mine also has a Miocene age of inception, as dated by Vikre (1994) in White Rock Canyon ~4 km north. LRCM = "Little Rock Candy Mountain".

Extensive Tertiary volcanics, sourced from multiple calderas and volcanic events that were active in the northern Great Basin during the middle Tertiary, comprise the uppermost bedrock units (Figure 2.4). The volcanics are dominantly Oligocene-aged ash-flow tuffs exhibiting varying degrees of hydrothermal alteration (Willden and Speed, 1974). Localized andesites and basalts of Miocene age are also present (Hudson and

Geissman, 1991; Page, 1965; Willden and Speed, 1974). The Oligocene tuffs are well-exposed at an outcrop on the northeastern side of Hare Canyon's mouth, referred to as "Little Rock Candy Mountain" (LRCM) in this study (Figure 2.4).

Mesozoic rocks of Jurassic and Triassic age underlie the Tertiary volcanics. Cretaceous plutons have been found exposed in the northwestern Stillwater Mountains and in wells drilled in northern Dixie Valley (Lutz et al., 1997; Page, 1965; Speed, 1976; Waibel, 1987), but are not encountered in the Dixie Meadows area. The youngest Mesozoic rocks at Dixie Meadows are middle Jurassic (Willden and Speed, 1974) intrusive and extrusive volcanics of varying thickness that comprise the Humboldt igneous complex (Dilek and Moores, 1995), originally referred to as the Humboldt lopolith by Speed (1976). These Jurassic volcanic rocks (Figure 2.4) are juxtaposed and interbedded with Triassic and lower Jurassic marine units; they appear to originate from a subduction-driven, plutonic arc that was transported eastward in the Luning-Fencemaker allochthon (Dilek and Moores, 1995). Lower Jurassic sedimentary units are of the ~200 m thick Boyer Ranch Formation, consisting of limestone overlain by quartzite (Speed, 1976). The Boyer Ranch Formation unconformably overlies a thick sequence of Triassic marine metasediments consisting of slate, metaquartzite, and phyllite (Page, 1965; Silberling and Roberts, 1962; Speed, 1976). The thickness of this sequence is unknown, but is inferred to be several kilometers (Speed, 1976). For the purposes of this study, the Boyer Ranch Formation and Triassic sequence are presented as a single unit (Figure 2.4).

2.2.3 Cenozoic structural summary and geothermal implications

Holocene fault scarps at Dixie Meadows include the northern-most ruptures of the 1954 Dixie Valley earthquake and from the 2.0-2.5 ka Stillwater Seismic Gap event. Previously mapped fault scarps, compiled by Sawyer and Anderson (1999), from both events are included in Figure 2.4; their fault scarp compilation includes the low-angle lateral spreading features of Watts (2010). Continued investigations by J. Caskey and J. Bell (2012, personal communication) indicate that these basin features are relatively superficial and unlikely to be related to geothermal structural controls, and are thus not included in this study.

The 1954 event was a M_S 6.8, normal slip, ~12 km deep earthquake that produced a 42 km long rupture zone with scarp heights ranging from up to 3 m in southern Dixie Valley to < 50 cm in Dixie Meadows (Caskey et al., 1996; Doser, 1986; Slemmons, 1957). Visible effects on the geothermal features at Dixie Meadows included rising steam from fumaroles at the rangefront and the appearance of small mud and silt volcanoes near the Dixie Hot Springs (Slemmons, 1957).

The Stillwater Seismic Gap event is a spatial gap between historic ruptures – the 1954 Dixie Valley earthquake to the south, and the 1915 Pleasant Valley earthquake to the north (Page, 1935; Wallace, 1984) – containing a 40 km long zone of paleoscarps (Wallace and Whitney, 1984). The event is estimated to be 2.0-2.5 ka based on radiocarbon dating of faulted sinter deposits and is interpreted to have been a M_W 7.1-7.3 earthquake that generated ~ 3 m of average vertical slip (Bell et al., 2004; Lutz et al., 2002).

Overlap of the Holocene fault zones and varying fault scarp patterns at Dixie Meadows are potentially favorable for increasing permeability required to host an economic geothermal system. The 1954 Dixie Valley rupture zone overlaps the Stillwater Seismic Gap scarps by ~22 km (Bell et al., 2004). Enhanced geothermal activity at Dixie Meadows has been associated with fault endpoint interaction and stress redistribution created by the intercalating fault zones (Caskey and Wesnousky, 2000; Smith et al., 2001). Fault scarps displayed in Figure 2.4 primarily strike north-northeast. A subtle, right-stepping pattern of north-striking fault scarps is contained within the north-northeast striking fault scarps. There is a nearly 2 km right-step, along an east-northeast bend in the rangefront, of the faults from the north end of the 1954 Dixie Valley ruptures to the Stillwater Seismic Gap scarps (Figure 2.4). The scarps and rangefront bend from a north-northeast to a northward strike near the Dixie Comstock Mine. These stepping and intersecting fault patterns resemble other favorable structural settings for geothermal activity in the Great Basin (e.g., Faulds et al., 2011).

North-striking, Miocene-aged normal faults mapped in the Stillwater Mountains and surrounding areas are indicative of inherited structural controls on geothermal activity at Dixie Meadows. Speed (1976) mapped several north-striking faults in the northern Stillwater Mountains; two of these faults are located at the north end of the Dixie Meadows study area (Figure 2.4). The north-striking fault segment crossing through the Dixie Comstock Mine is interpreted to be an east-dipping, moderate-angle normal fault from the middle Miocene based on observed displacement of Mesozoic and Tertiary rocks in White Rock Canyon, ~4 km north of the Dixie Comstock Mine (Speed, 1976; Vikre, 1994). North-striking faults in this part of the Great Basin have been

associated with middle to late Miocene extension (Fosdick and Colgan, 2008; Proffett Jr., 1977; Stockli, 1999; Surpless et al., 2002; Vikre, 1994; Waibel, 1987). North-striking faults and fault segments appear to be inherited from this older extensional episode; superposition of modern north-northeast extensional faults upon older north-striking faults in Dixie Valley appears to enhance fault/fracture permeability (Waibel, 1987).

Northwest-striking faults in the Stillwater Mountains and other nearby locales are associated with late Oligocene to early Miocene extensional and dextral motion. Oligocene- to late Miocene-aged geologic units are moderately to steeply tilted northeastward or southwestward, along north- to northwest-striking faults, in the Stillwater Mountains (Hudson and Geissman, 1991). These northwest-striking faults are likely related to high-angle extensional faulting of late Oligocene to early Miocene age interpreted at other locales (e.g., John et al., 1989; Boden, 1986). Right-lateral offsets along these faults are also apparent (Boden, 1986; Hudson and Geissman, 1991). These are the oldest-documented Cenozoic extensional faults associated with structural development of the Stillwater Mountains and Dixie Valley, and they likely influence geothermal fluid migration in the subsurface.

2.3 Methods

2.3.1 Hydrothermal surface expression assessment

A reconnaissance-level survey of spring fluid from the Dixie Hot Springs and other springs in the study area was performed in May of 2012. Fifty springs were sampled at, or as close as possible to, locations where the spring fluid is first exposed to

the surface, as depicted in Figure 2.5. Each spring was measured in-situ for temperature, pH, and total dissolved solids (TDS) using a thermocouple meter and a pH/conductivity meter with location control provided by hand-held GPS. Measurement locations are displayed in Figure 2.6.

Figure 2.5. Pictures from the spring fluid survey. Field assistant C. Dudley measures pH/TDS (left panel) and temperature (right panel). Note that measurements are being performed where the fluid first comes to the surface.

Two fumarole zones (Figure 2.6), identified by Kennedy-Bowdoin et al. (2004), were revisited in this study to investigate mineralization and measure temperatures. Rock/precipitate samples were collected from the fumaroles, examined under a microscope, and analyzed via x-ray diffraction (XRD) and analytical spectral device (ASD) instrumentation in order to precisely identify mineralization. Three temperature measurements at the fumaroles were acquired in February of 2012 using a thermocouple meter. Temperatures were measured by digging a small hole, ~0.5 m deep, into the fumarole, emplacing the thermocouple sensor, back-filling the hole, allowing the temperature reading to stabilize for ~10 minutes, and then recording the temperature.

Upon completion of the measurement, the thermocouples were removed and the holes were backfilled and reclaimed.
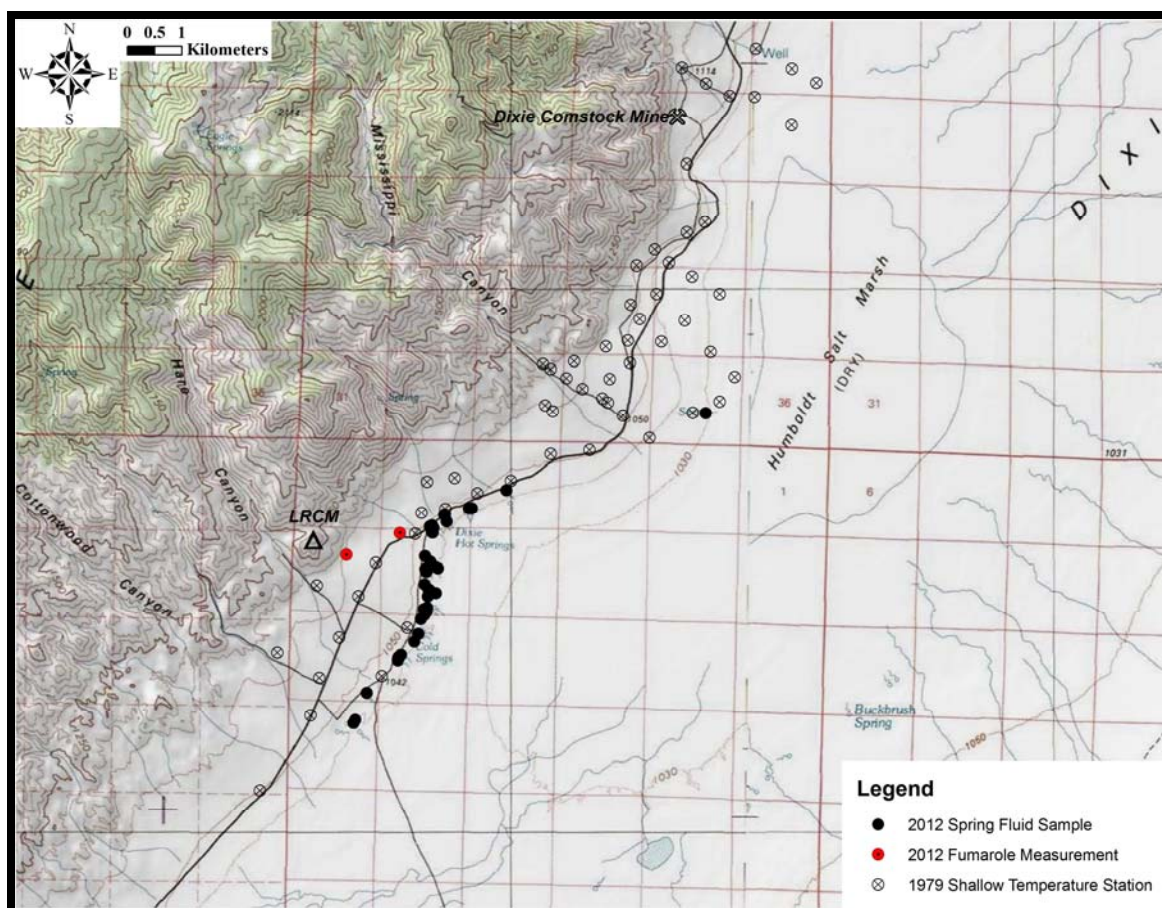
Figure 2.6. Locations of data collected for hydrothermal surface expression analyses. Spring fluid and fumarole data were obtained during this study, and one-meter shallow temperatures were collected by Campana et al. (1980).

Shallow temperatures were collected across northern Dixie Valley in a survey performed in the summer of 1979 (Campana et al., 1980). 59 one-meter deep measurements were performed in the Dixie Meadows study area (Figure 2.6 and Appendix A). Temperatures acquired from the 1979 shallow temperature survey and the

spring fluid and fumarole surveys of 2012 were compiled into a single near-surface temperature database for analysis.

2.3.2 Geologic Reconnaissance

Qualitative geologic reconnaissance of hydrothermally altered silicic volcanics was performed at LRCM and the mouth of Hare Canyon (Figure 2.4). Observations were focused on the Tertiary silicic volcanics, as originally mapped by Page (1965), that are proximal to the hydrothermal surface expressions investigated in this study (Figure 2.6). Hyperspectral studies confirm that abundant argillic and advanced argillic hydrothermal alteration zones are concentrated in the silicic volcanics at LRCM and the mouth of Hare Canyon (Kennedy-Bowdoin et al., 2004; Lamb et al., 2011). In this study, the altered silicic volcanics were examined in the field during several visits in 2012 to elicit more detailed geologic descriptions, deduce likely age correlations, and identify structures delineated by stratigraphic offset, fault slicks, and/or fault gauge. Hand samples were collected for grain-scale analysis using a microscope.

Drill cuttings from two geothermal exploration wells were examined for possible lithologic correlations to exposed geologic units and to provide geophysical modeling constraints. Wells 45-14 and 42-9 were drilled in 1979 and 2011, respectively (Figures 2.3 and 2.4). 45-14 was collared 710 m to the southeast of the Dixie Comstock Mine, was drilled 2.75 km deep, penetrated the rangefront fault at ~750 m depth, and was completed in Mesozoic basement of relatively low fluid permeability and poor fracture orientation/sustainability – factors that rendered the well unproductive for geothermal power production, despite a maximum measured temperature of 197 °C (Edmiston and

Benoit, 1984; Hickman et al., 1998; Vikre, 1994; Zoback, 1999). In the Dixie Meadows basin, well 42-9 was drilled ~2.2 km deep, did not intersect any major fault/production zones, bottomed in silicic volcanics, and reached a maximum temperature of 120 °C (B. Delwiche, 2012, personal communication). Depth-registered drill cuttings from 45-14 and 42-9 were made available by the Nevada Bureau of Mines and Geology (NBMG) and by Ormat Technologies Inc. (Ormat), respectively; measured depths were converted to vertical depths using well survey information provided by the NBMG and Ormat. Drill cuttings were examined using a microscope. Observed properties were compared to the lithologic descriptions of units exposed in the Stillwater Mountains and encountered by wells in northern Dixie Valley (Page, 1965; Silberling and Roberts, 1962; Speed, 1976; Waibel, 1987; Willden and Speed, 1974) (Table 2.1), and to mud logging reports shared by the NBMG and Ormat, in order to deduce lithologic correlations.

Table 2.1. Lithologic unit summary of regional formations found in the study area.

General Unit	Formation	Formation Description	Lithologic Properties
Basin sediments	QTal	Quaternary/Tertiary alluvial/lacustrine sediment	Heterogeneous, unconsolidated
Tertiary volcanics	Ta	Tertiary intermediate andesites	Tuffaceous, contains felsic mineral grains
	Tb	Tertiary mafic basalts	Mafic, w/ distinct plagioclase phenocrysts
	Tt	Tertiary rhyolitic ash-flow tuffs	Heterogeneous mineral content, stratified
Jurassic volcanics	Jv	Jurassic mafic igneous rocks	Dominantly hornblende-gabbro
Triassic sediments	TRma	Triassic metasiltstone	Silty, fine-grained, silicified
	TRms	Triassic metaquartzarenite	Medium-grained, subrounded, silicified

2.3.3 Gravity and magnetic methods

Zonge Geosciences Inc. (Zonge) performed the gravity survey at Dixie Meadows, under contract to Ormat, in 2010. Zonge collected 516 gravity stations, using LaCoste & Romberg Model-G gravimeters, in a grid pattern with a nominal station-to-station spacing of 400 m (Figure 2.7). Gravity data were corrected and reduced by Zonge

(Appendix B). Zonge provided a suite of Complete Bouguer Anomaly (CBA) density reductions, ranging from 2.00-2.67 g/cc, and determined that a Bouguer density of 2.35 g/cc produced the minimum topographic influence (e.g., Nettleton, 1939).
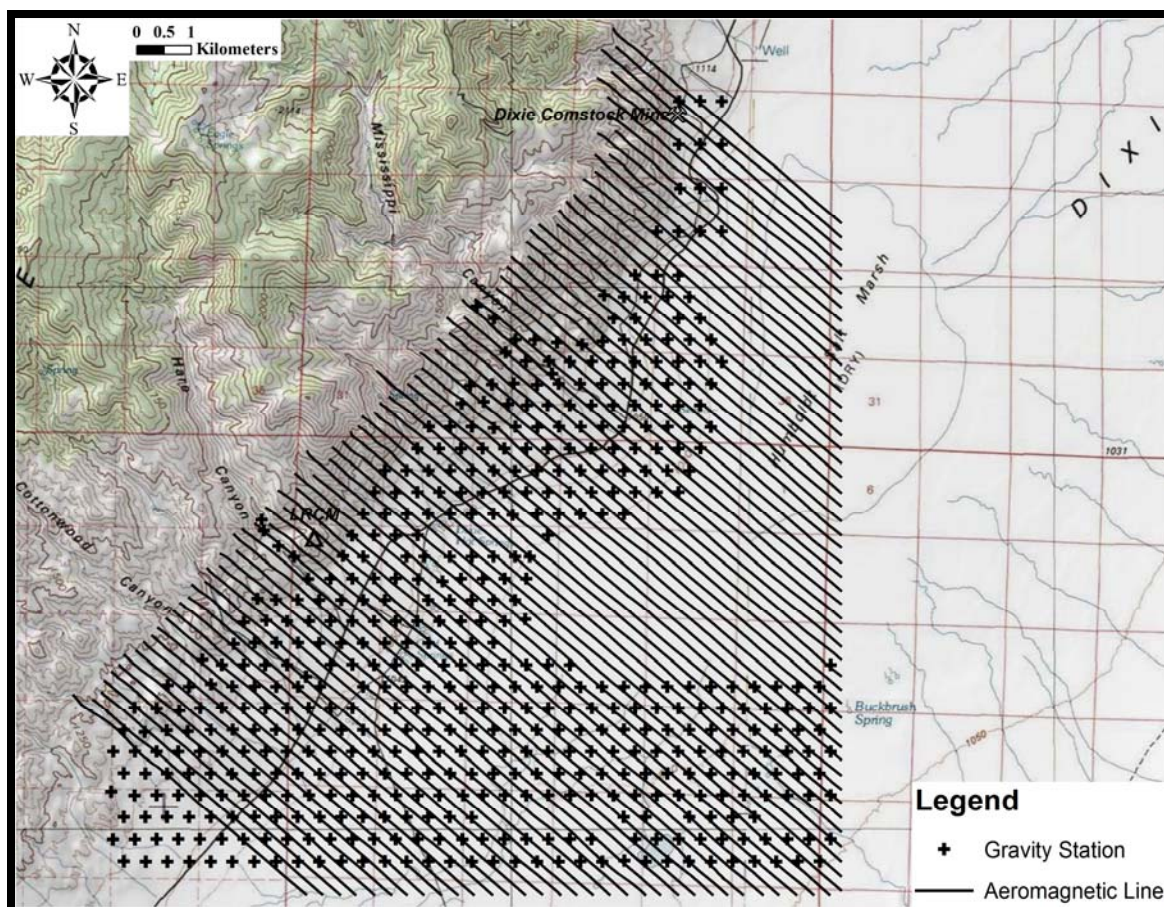
Figure 2.7. Gravity and aeromagnetic data coverage.

Pearson, deRidder, and Johnson Inc. (PRJ) collected magnetic data at Dixie Meadows, under contract to the United States Geological Survey, as part of a larger aeromagnetic survey that spanned northern Dixie Valley (Grauch, 2002). PRJ executed the survey with a helicopter-borne, cesium-vapor magnetometer flown ~120 m above the ground surface on a total of over 240 transects nominally spaced 200 m apart and oriented N30°W. PRJ corrected and reduced the data to a final total field (TF) magnetic

dataset of northern Dixie Valley (Appendix B). For this study, the TF dataset was clipped to include only the western side of the 80 southernmost transects that cover the Dixie Meadows geothermal prospect (Figure 2.7). The TF data were reduced-to-pole (RTP) in Montaj to minimize the polarity effects caused by geometric obliquity of magnetized bodies with respect to the inclination of Earth's primary magnetic field (Baranov, 1957; Blakely, 1996). The reduction calculation was based on a primary magnetic field of 51,518.02 nT magnitude, 15° declination, and 64° inclination (Grauch, 2002). The RTP magnetic data were used for all subsequent magnetic analysis, interpretation, and modeling.

CBA gravity and RTP magnetic data were gridded and analyzed in 2D map-view for first-order interpretation using Geosoft's Oasis Montaj software (Montaj); dual forward modeling of the datasets was performed with Geosoft's GM-SYS Profile Modeling software (GM-SYS). Dual model profiles 1) followed gravity station coverage, and 2) were oriented approximately perpendicular to linear trends observed in gravity maps and across magnetic anomalies. Observed data for each profile came from CBA values of gravity stations (or else were extrapolated from the CBA minimum curvature grid), and sampling of the RTP grid for magnetic values corresponding to the gravity station locations.

2D profile modeling was performed by defining densities and magnetic susceptibilities (in cgs units) for representative geologic units. Modeling geologic units as having singular values of density and magnetic susceptibility are simplifications. Density logs in Great Basin wells, for instance, generally show gradationally increasing density (i.e., increasing compaction) of basin fill material with depth. Magnetic susceptibility in

geologic units is generally heterogeneous; furthermore, there may be a component of magnetic remanence that influences measured magnetic data. For the purposes of this modeling approach, however, it is reasonable to assume that these effects are either "averaged out" or negligible.

2D geophysical modeling enables the user to define polygonal geologic units on the 2D profile, with specified geophysical parameters (in this case, density and magnetic susceptibility), that represent prismatic bodies of infinite perpendicular extent (Figure 2.8). For the purposes of modeling geologic bodies that are laterally extensive, this is a reasonable approximation.
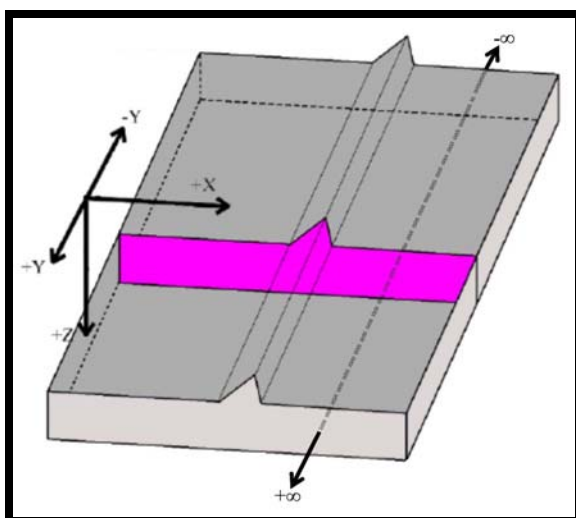
Figure 2.8. Diagram, adapted from the GM-SYS user manual, illustrating the concept of a 2D model. The magenta plane represents a 2D polygon defined in a GM-SYS model profile (X and Z axes). The polygon defines a prismatic body of presumed infinite perpendicular (Y axis) extent.

Dual model cross-sections were exported from GM-SYS, georeferenced, and imported into Aranz Geo Limited's Leapfrog Geothermal 3D program (Leapfrog). Leapfrog employed the implicit modeling technique for 3D interpolation of geological data (e.g., Chaodong et al., 2010). The multi-oriented 2D cross-sections exported from GM-SYS were all utilized in Leapfrog to implicitly model 3D meshes representing the faults and the basin fill depth.

2.4 Observations and results

2.4.1 Hydrothermal surface expressions

Springs at Dixie Meadows were devoid of deposits commonly found at thermal springs (e.g., sinter or travertine terraces). The springs generally contained clear fluid and supported biota such as reeds and algae; some spring pools were even inhabited by fish and frogs. Measurements of temperature, pH, and TDS from the spring fluid survey are presented in Table 2.2. Distributions of pH and TDS are mapped in Figure 2.9.

The fumaroles are not of the type often found at magmatic geothermal systems that generally exhibit constant or intermittent pressurized steam flow. Steam emanating from the fumaroles at Dixie Meadows does not appear to be under pressure; rather it subtly escapes to the open air. The fumaroles are most discernible by sulfate precipitates at the surface and warm ground temperatures. Microscope-enhanced observations and XRD/ASD analyses of fumarole samples detected native sulfur, sulfate mineral precipitates, and advanced argillic minerals. Sulfates included gypsum, anhydrite, and alunogen; advanced argillic minerals consisted of kaolinite and alunite (B. Littlefield & J. McCormack, 2012, personal communications). Recorded fumarole locations and temperatures are provided in Table 2.3.

Table 2.2. Data from the spring fluid survey, listed in chronological order of measurements.

Easting (m) (±3 m)	Northing (m) (±3 m)	Elevation (m) (±0.1 m)	Date	Time	Temperature (°C) (±0.2 °C)	pH (±0.05)	TDS (ppm) (±15 ppm)
407063	4402241	1040.0	18-May-2012	9:20	14.1	6.60	430
407032	4402181	1039.6	18-May-2012	9:30	11.8	7.60	840
407274	4402742	1040.8	18-May-2012	10:25	13.1	*	*
407849	4403338	1040.2	18-May-2012	10:50	16.1	7.08	599
407853	4403369	1041.2	18-May-2012	10:55	23.7	7.23	595
407867	4403375	1040.5	18-May-2012	11:00	22.1	7.23	597
407861	4403389	1041.1	18-May-2012	11:10	32.5	7.85	607
407879	4403405	1040.3	18-May-2012	11:20	29.7	7.53	604
407908	4403437	1039.9	18-May-2012	11:30	29.5	7.96	547
408150	4403679	1039.4	18-May-2012	12:10	30.7	7.94	533
408218	4403821	1040.0	18-May-2012	12:20	41.0	8.06	522
408227	4403823	1040.0	18-May-2012	12:30	39.2	8.26	549
408273	4404098	1041.3	18-May-2012	12:45	34.7	7.51	810
408336	4404172	1040.6	18-May-2012	13:00	45.0	8.17	630
408339	4404741	1042.4	18-May-2012	13:30	43.0	8.84	435
408412	4404652	1040.4	18-May-2012	13:40	44.1	8.94	563
408430	4404625	1040.1	18-May-2012	13:45	15.0	7.62	884
408432	4404633	1040.0	18-May-2012	13:50	46.9	8.58	546
408402	4404523	1040.6	18-May-2012	14:00	26.2	8.02	2390
408549	4404580	1038.7	18-May-2012	14:10	47.5	8.32	720
408385	4404309	1039.9	18-May-2012	14:25	42.6	8.38	572
408331	4404285	1041.5	18-May-2012	14:35	44.6	8.33	565
408374	4404234	1039.3	18-May-2012	14:40	54.2	8.23	611
408373	4404969	1041.6	18-May-2012	15:10	53.4	8.16	456
408370	4404973	1041.6	18-May-2012	15:15	52.1	8.45	434
408354	4405021	1043.0	18-May-2012	15:25	51.4	8.72	455
408363	4405026	1042.6	19-May-2012	8:10	44.1	8.59	404
408522	4405066	1040.1	19-May-2012	8:20	50.1	8.40	565
408588	4405033	1039.6	19-May-2012	8:30	43.0	8.50	538
408443	4405154	1041.3	19-May-2012	8:45	53.1	8.49	436
408345	4405257	1043.3	19-May-2012	8:55	39.6	8.52	344
408466	4405819	1044.6	19-May-2012	9:10	66.3	7.96	426
408477	4405822	1044.4	19-May-2012	9:15	49.1	8.07	553
408470	4405812	1044.5	19-May-2012	9:20	44.3	8.87	393
408436	4405803	1045.3	19-May-2012	9:25	61.3	8.60	405
408439	4405792	1045.1	19-May-2012	9:35	52.6	8.97	369
408500	4405775	1043.1	19-May-2012	9:40	69.8	8.32	393
408499	4405771	1043.1	19-May-2012	9:45	40.6	7.46	401
408483	4405772	1043.7	19-May-2012	9:50	47.2	8.23	542
408482	4405695	1042.6	19-May-2012	10:00	73.2	8.63	388
408479	4405695	1042.7	19-May-2012	10:05	65.1	8.77	394
408491	4405688	1042.3	19-May-2012	10:10	70.6	8.80	387
408743	4405893	1040.6	19-May-2012	10:55	38.4	8.00	1460
408703	4406022	1044.8	19-May-2012	11:10	58.3	7.40	923
408704	4406023	1044.8	19-May-2012	11:15	56.8	7.24	1280
408711	4406025	1044.4	19-May-2012	11:20	42.0	7.72	1230
409206	4406139	1041.8	19-May-2012	12:00	15.2	7.28	432
409157	4406139	1042.0	19-May-2012	12:05	16.3	8.12	490
409841	4406470	1041.9	19-May-2012	12:35	19.8	8.35	403
413511	4407888	1032.4	19-May-2012	13:25	12.1	7.46	4010

Easting and northing coordinates are registered to UTM Zone 11N, WGS 84. Elevations were extracted from a 10 m digital elevation model. * indicates missing datum.
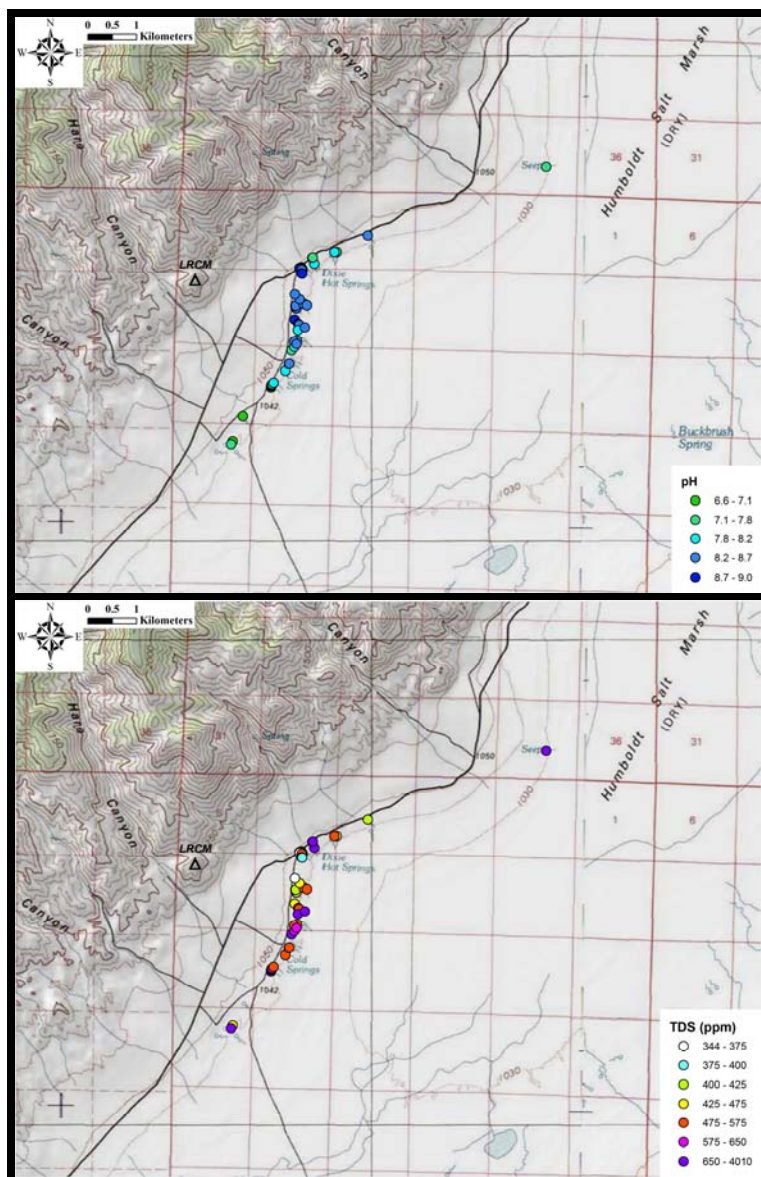
Figure 2.9. Spring fluid distributions of pH (top panel) and total dissolved solids (TDS) (bottom panel).

Table 2.3. Data from fumarole investigation.

Location	Easting (m) (±3 m)	Northing (m) (±3 m)	Elevation (m) (±0.1 m)	Date	Time	Temperature (°C) (±0.2 °C)
RF	406907	4405285	1094.0	22-Feb-2012	8:10	91.0
BF1	407848	4405679	1058.1	22-Feb-2012	9:05	57.0
BF2	407762	4405693	1059.7	22-Feb-2012	9:25	35.6

Fumarole abbreviations: RF = rangefront fumaroles, BF = basin fumaroles (Figure 2.6). Easting and northing coordinates are registered to UTM Zone 11N, WGS 84. Elevations were extracted from a 10 m digital elevation model.

Data utilized from the 1979 shallow temperature survey are presented in Appendix A (Campana et al., 1980). The shallow temperature data were combined with temperature data from the spring fluid and fumarole surveys to map near-surface temperatures (Figure 2.10). The compiled near-surface temperatures were gridded using Montaj via linear model kriging (Figure 2.10), after Calder and Cressie (2009).
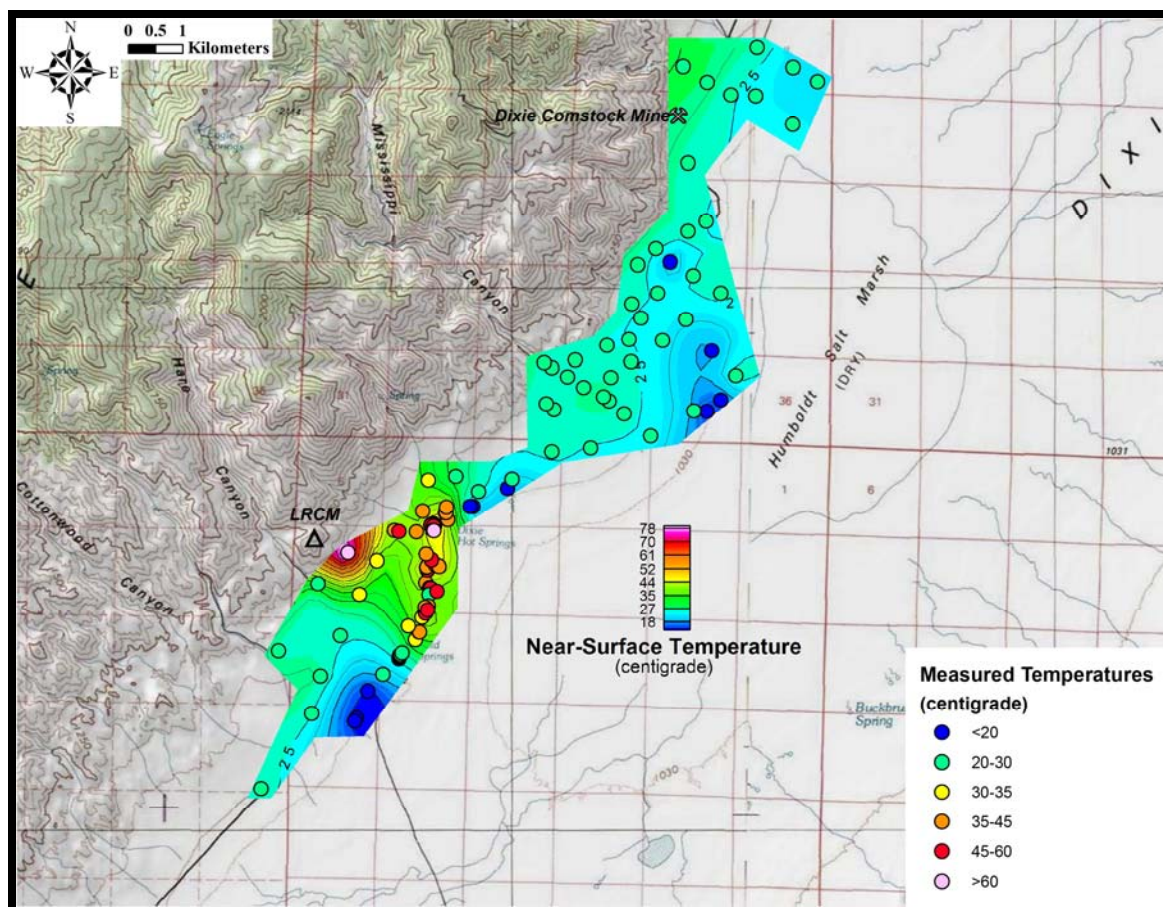

Figure 2.10. Map of compiled near-surface temperatures. Measurements are denoted by colored circles. Color contour grid, highlighting the thermal anomaly from LRCM to the Dixie Hot Springs, was created via linear model kriging of the measurements.

2.4.2 Lithology and stratigraphic/structural relationships

The Tertiary volcanics exposed at the mouth of Hare Canyon and LRCM are comprised of four distinctive units of ash-flow tuffs, and a basaltic dike, unconformably juxtaposed against Mesozoic rocks. Figure 2.11a is a perspective photo, looking east-northeast across the mouth of Hare Canyon, of LRCM that captures each of the observed geologic units (Figures 2.11b and 2.11c). Alluvial Quaternary fill spills out of Hare Canyon and into the basin. Tertiary volcanics flank each side of the mouth of Hare Canyon. The volcanics are comprised primarily of four distinctive ash-flow tuffs (Tt_0 – Tt_3), generally dipping ~30° east-southeast, that are lithologically described in Table 2.4. A basaltic dike intrudes Tt_1 on the northwest side of LRCM. The Tertiary volcanics are in unconformable contact with strongly foliated Triassic slates to the north.

The distinguishable, well-exposed volcanic units preserve post-depositional fault traces and landslide remnants. Stratigraphic offset and fault slicks/gauge in the tuffs qualitatively delineate four normal faults and their relative direction of offset (Figures 2.11 and 2.12): 1) a northwest-striking, southwest-dipping normal fault separating the tuffs at LRCM from the tuffs across Hare Canyon; 2) an east-northeast-striking, north-northwest-dipping normal fault on the north edge of LRCM, separating the Tertiary volcanics from the Triassic slate; 3) a north-striking, east-dipping normal fault across LRCM; and 4) an east-northeast-striking, south-southeast-dipping normal fault along the southern flank of LRCM that intersects the rangefront fault near the fumarole zone. Two landslides are outlined by arcuate scarps above rubblized zones in the tuffs (Figure 2.12).
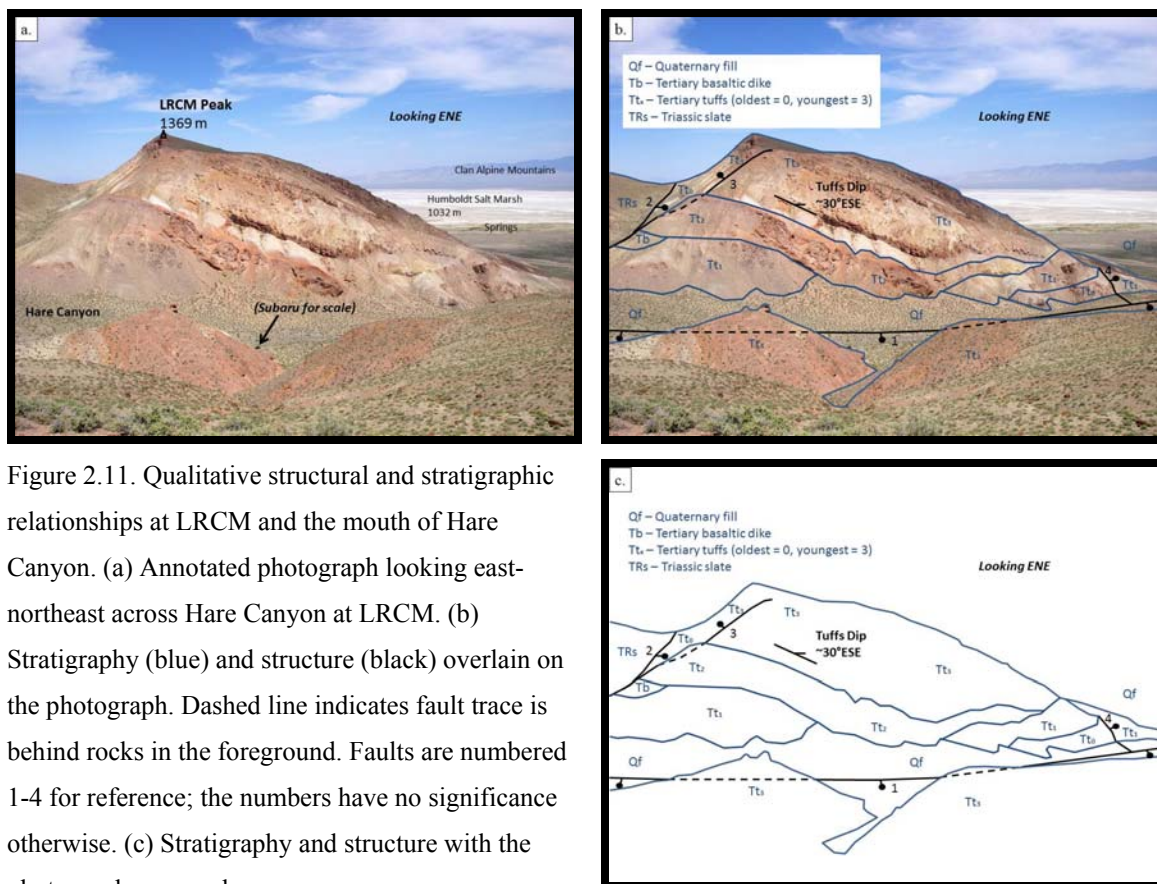
Figure 2.11. Qualitative structural and stratigraphic relationships at LRCM and the mouth of Hare Canyon. (a) Annotated photograph looking east-northeast across Hare Canyon at LRCM. (b) Stratigraphy (blue) and structure (black) overlain on the photograph. Dashed line indicates fault trace is behind rocks in the foreground. Faults are numbered 1-4 for reference; the numbers have no significance otherwise. (c) Stratigraphy and structure with the photograph removed.

Table 2.4. Lithologic description of Tertiary ash-flow tuffs.

Formation	Lithology
Tt_3	Vitric ash-flow tuff with clasts of pumice. Contains quartz, plagioclase, & sanidine.
Tt_2	Porphyritic, welded ash-flow tuff. Contains plagioclase & sanidine phenocrysts.
Tt_1	Biotite-rich ash-flow tuff. Contains plagioclase phenocrysts.
Tt_0	Sparsely porphyritic ash-flow tuff. Quartz-rich, also has sanidine & minor biotite.

Total thickness of these units combined, as exposed at the LRCM outcrop, is ~200m.
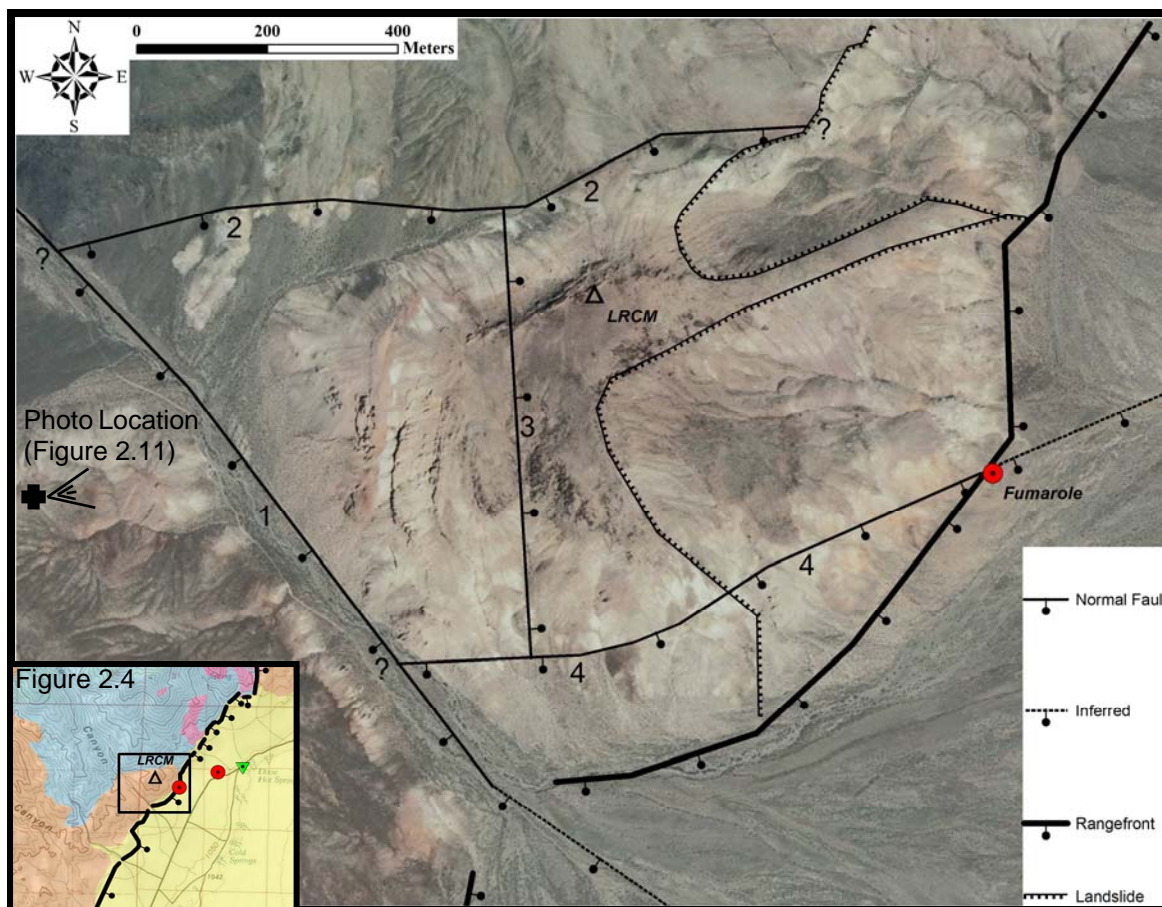
Figure 2.12. Qualitative structural map of LRCM and Hare Canyon overlain on satellite imagery. Fault numbers correspond to Figure 2.11. Question marks on the ends of faults 2 and 4 indicate the traces of the faults become obscure, and may or may not continue beyond those points. Inset at the bottom-left is part of Figure 2.4 – the black rectangle in the center outlines the satellite map perimeter, for reference.

Examination of well cuttings yields lithologic information and depth-to-bedrock constraints. Lithology summaries, based on regional correlations (Table 2.1), are provided in Table 2.5. In well 42-9, Quaternary to Tertiary basin fill reaches a vertical depth of 1470 m. The first bedrock unit encountered is a basaltic dike similar to the unit found on LRCM. The remainder of the drill interval is comprised of each of the late Oligocene tuffs found at LRCM. The thickness of the tuffs encountered in 42-9 is >600 m, compared to ~200 m at LRCM. Well 45-14 encounters bedrock at 335 m through an

interval of interbedded Tertiary tuffs and andesites. LRCM tuff Tt_0 appears in a 49 m thick interval, but none of the other LRCM tuffs were recognized. Triassic metasediments, consisting of interbedded metasiltstones and metaquartzarenites, are encountered beneath the rangefront fault intersection at 768 m depth, and are prevalent to the bottom of the well. Thin intervals of Jurassic gabbro of the Humboldt igneous complex intrude the metasediments. Depth-to-bedrock in well 42-9 and the depth of the rangefront fault in 45-14 are key modeling constraints.

Table 2.5. Lithologic summaries of wells 42-9 and 45-14 (continues on next page).

	MD top (m)	MD bot (m)	VD top (m)	VD bot (m)	VT unit (m)	Formation	Dominant Colors	Lithology
Well 42-9	0	396	0	396	396	Qalc	grn, gry	Clay intrbeded w/ alluvial sands & lacustrine silt
	396	1119	396	1101	705	QTas	gry, wht, vc	Alluvial sand & gravel
	1119	1524	1101	1470	369	QTvs	red, brn, vc	Volcanic, lithic sand
	1524	1582	1470	1521	51	Tb	gry, blk	Dense, basaltic dike w/ plag phenos
	1582	2024	1521	1925	404	Tt_3	brn, gry	Vitric ash-flow tuff w/ qtz, plag, & sanidine; pumice clasts
	2024	2088	1925	1984	59	Tt_2	gry, wht	Porph, welded ash-flow tuff w/ plag & sanidine
	2088	2182	1984	2067	83	Tt_1	gry, brn	Biotite-rich ash-flow tuff w/ plag
	2182	2268	2067	2146	79	Tt_0	wht, gry, red	Qtz-rich, sparsely porph ash-flow tuff w/ sanidine & minor biotite
Well 45-14	0	256	0	256	256	Qas	gry, wht, vc	Alluvial sand & gravel, minor pyrt & biotite
	256	308	256	308	52	QTav	gry, wht, red, brn	Above, mixed w/ volcanic, lithic sand
	308	335	308	335	27	QTvs	red, brn, vc	Volcanic, lithic sand
	335	408	335	408	73	Ttp	gry, wht, red, vc	Ash-flow tuff w/ plag, pryite, & biotite
	408	518	408	518	110	Ta_1	gry, blk, brn	Tuffaceous andesite w/ plag, qtz, & pyrt
	518	567	518	567	49	Tt_0	wht, gry, red	Qtz-rich, vitric porph ash-flow tuff w/ sanidine & minor biotite
	567	664	567	664	97	Ta_0	blk, grn, brn	Dense, tuffaceous andesite w/ felds & qtz
	664	730	664	730	66	Ttq	wht, tan, gry	Qtz-rich, rhyolitic, vitric ash-flow tuff w/ plag & minor biotite
	730	768	730	768	38	Ttql	wht, tan, gry, red	Above, increasingly lithic & andesitic, minor pyrt
	768	1140	768	1138	370	TRms	blk, gry, grn	Fine-grain, well-sort, silicic metasilts w/ crbncs mtrl & pyrt
	1140	1149	1138	1147	9	Jv	grn, blk	Med-grain, micro-xln plag/pyrxn/olvn/hrnblnd gabbro
	1149	1256	1147	1254	107	TRms	blk, gry, grn	Fine-grain, well-sort, silicic metasilts w/ crbncs mtrl & pyrt
	1256	1274	1254	1272	18	Jv	grn, blk	Med-grain, micro-xln plag/pyrxn/olvn/hrnblnd gabbro
	1274	1420	1272	1418	146	TRms	blk, gry, grn	Fine-grain, well-sort, silicic metasilts w/ crbncs mtrl & pyrt
	1420	1426	1418	1424	6	Jv	grn, blk	Med-grain, micro-xln plag/pyrxn/olvn/hrnblnd gabbro
	1426	1481	1424	1479	55	TRms	blk, gry, grn	Fine-grain, well-sort, silicic metasilts w/ crbncs mtrl & pyrt
	1481	1500	1479	1498	19	TRms	wht, gry, blk, grn	Above, w/ mmphsd plag, calcite, & qtz, minor biotite & pyrt
	1500	1783	1498	1779	281	TRms	blk, gry, grn	Fine-grain, well-sort, silicic metasilts w/ crbncs mtrl & pyrt
	1783	1853	1779	1848	69	TRms	wht, gry, blk, grn	Above, w/ mmphsd plag, calcite, & qtz, minor biotite & pyrt
	1853	2030	1848	2024	176	TRmsa	gry, blk, wht	Interlayered, siliceous metasilts & metaqtzarenite w/ plag
	2030	2149	2024	2141	117	TRma	blk, gry, wht	Med-grain, subrnd, slilic metaqtzarenite w/ plag & calcite
	2149	2210	2141	2200	59	TRma	gry, wht, blk	Above, w/ mmphsd plag, calcite, & qtz, minor biotite & pyrt
	2210	2332	2200	2319	119	TRma	gry, blk, wht	Med-grain, subrnd, slilic metaqtzarenite w/ plag & calcite
	2332	2432	2319	2417	98	TRms	gry, blk, grn, wht	Fine-grain, well-sort, silicic metasilts w/ crbncs mtrl & plag
	2432	2457	2417	2442	25	Jv	grn, blk	Med-grain, micro-xln plag/pyrxn/olvn/hrnblnd gabbro
	2457	2609	2442	2591	149	TRms	gry, grn, blk, wht	Fine-grain, well-sort, silicic metasilts w/ crbncs mtrl & plag
	2609	2719	2591	2699	108	TRma	gry, blk, wht	Med-grain, subrnd, slilic metaqtzarenite w/ plag & calcite
	2719	2749	2699	2729	30	TRmsa	gry, blk, wht, grn	Interlayered, siliceous metasilts & metaqtzarenite w/ plag

42-9 Vertical Thickness (m)		45-14 Vertical Thickness (m)		blk = black	crbncs = carbonaceous, felds = feldspar, hrnblnd = hornblende,
Basin Fill:	1470	Basin Fill:	335	brn = brown	mmphsd = metamorphosed, mtrl = material, olvn = olivene,
Tb:	51	Ta:	207	grn = green	phenos = phenocrysts, plag = plagioclase, porph = porphyritic,
LRCM Tt:	625	LRCM Tt:	49	gry = grey	pyrt = pyrite, pyrxn = pyroxene, qtz = quartz, sbrnd = subrounded,
		Other Tt:	177	vc = various colors	xln = crystalline
Unit Thickness @ LRCM (m)		Jv:	58	wht = white	
LRCM Tt:	200	TR:	1903		

2.4.3 Dual gravity and magnetic analysis and modeling

2.4.3.1 2D geophysical maps

Maps of the gravity data were generated in Montaj for analysis. CBA data, reduced to 2.35 g/cc, were gridded using the minimum curvature method (e.g., Briggs, 1974) at a grid cell size of 100 m (Figure 2.13). The CBA map generally displays high CBA values spatially correlating with competent bedrock of the Stillwater Mountains and low values correlating to unconsolidated Dixie Valley basin sediments. CBA contours mimic the structural grain of the rangefront fault scarps.
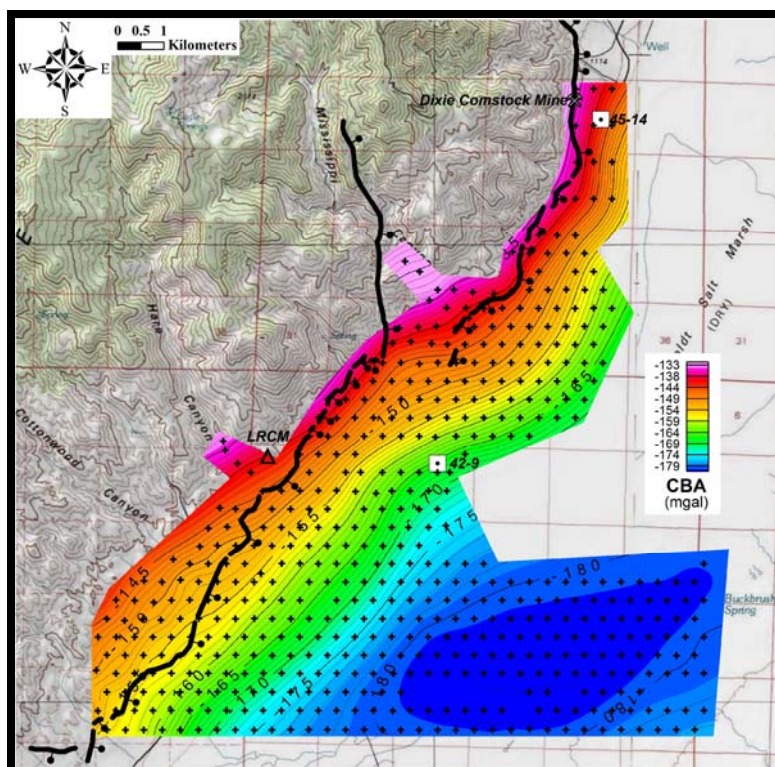

Figure 2.13. Color contour map of the minimum curvature gridded complete Bouguer anomaly (CBA) in milligals (mgal), at a reduction density of 2.35 g/cc, overlain by gravity station coverage and mapped fault scarps for reference. High CBA values correlate to Stillwater Mountain bedrock, and lows correlate to Dixie Valley basin sediments.

For more detailed insight, the horizontal derivative of the CBA data was calculated (Blakely, 1996) and gridded in Montaj to highlight the maximum CBA gradients (Figure 2.14). The horizontal gradient grid was upward-continued 60 m to reduce the effects of high-frequency, near-surface effects (Blakely, 1996). Linear horizontal gradient maxima are indicative of relatively sharp changes in the gravity field. The rangefront fault segments generally have adjacent, linear gradient trends. Additionally, several linear horizontal gradient trends located in the basin are oriented subparallel to the rangefront fault zone and are not outlined by surface fault scarps.
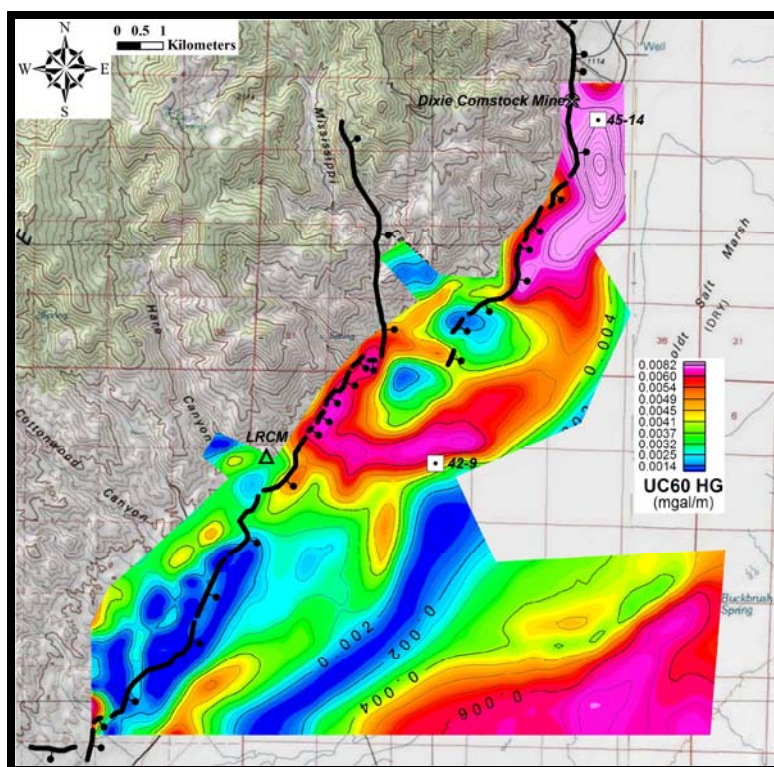

Figure 2.14. Color contour map of the horizontal gradient (HG) of the CBA, upward-continued 60 m (UC60). Linear horizontal gradient maxima delineate rapid changes in the gravity field. Note the linear gradients adjacent to the rangefront fault scarps, and subparallel linear gradient trends that are also present in the basin.

Magnetic data maps were also produced using Montaj. The final TF data were gridded using bi-directional Akima spline interpolation (Akima, 1970) at a grid cell size of 100 m, re-gridded to 50 m (Figure 2.15). This grid was then reduced to the magnetic

pole in Montaj, in order to remove the effects from Earth's magnetic field inclination, to produce an RTP grid (Figure 2.16). RTP magnetic anomalies are generally centered over their causative subsurface bodies (Blakely, 1996). Relative magnetic high and low anomalies of varying amplitude occur across the study area. For instance, there is a magnetic high immediately west of the Dixie Comstock Mine that spatially correlates with previously mapped exposure of the Jurassic volcanics (Figures 2.4 and 2.16). A magnetic low, on the other hand, appears to protrude from the rangefront and into the basin between LRCM and well 42-9 (Figure 2.16).
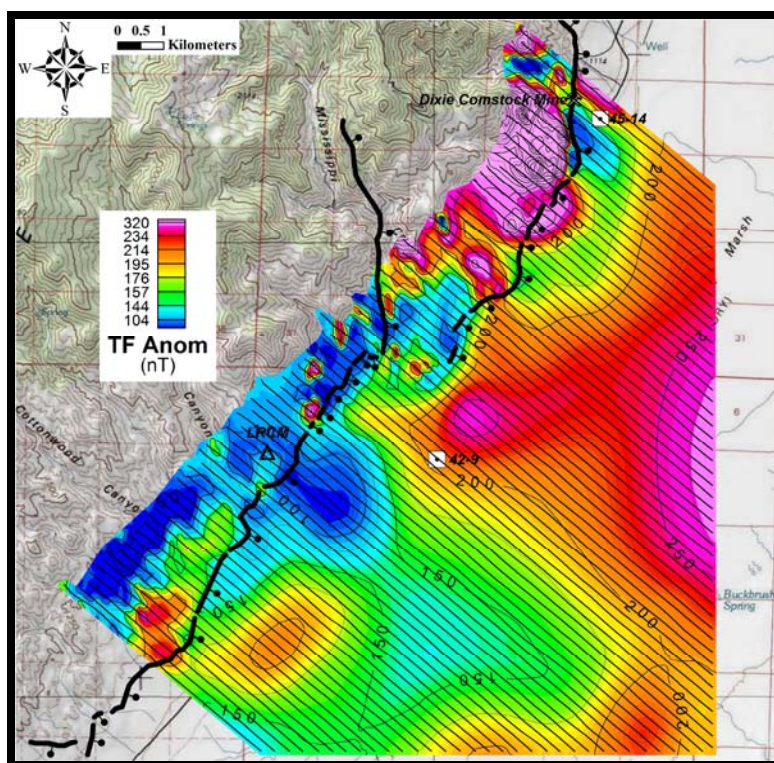

Figure 2.15. Color contour map of the bi-directionally gridded magnetic total field anomaly (TF Anom) data, overlain by transect coverage. Magnetic data is measured in units of nanoTeslas (nT).
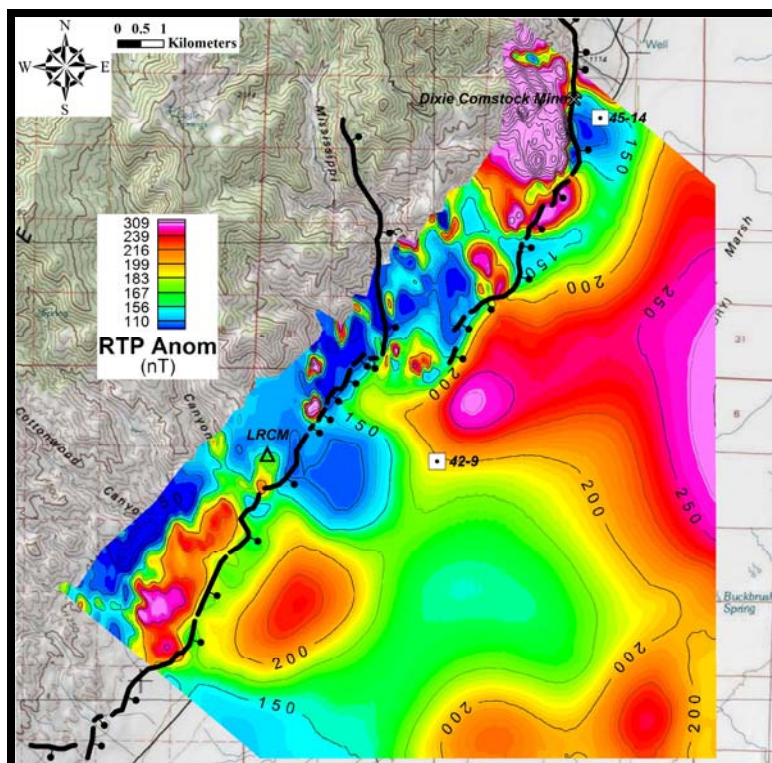
Figure 2.16. Color contour map of the magnetic reduced-to-pole anomaly (RTP Anom) data. RTP anomalies have been corrected for Earth's magnetic inclination, and are centered over their causative bodies. Note the magnetic low protruding from the rangefront between LRCM and 42-9.

2.4.3.2 2D dual model profiles

The CBA and RTP data were utilized for 2D dual forward modeling profiles using GM-SYS. Twelve profiles, labeled A-Aʹ through L-Lʹ, were selected for dual modeling based on gravity coverage, and trends/anomalies observed in the horizontal gravity gradient and RTP magnetic maps (Figure 2.17). Profiles primarily trend east to southeast, except F-Fʹ is oriented to the northeast as a cross-line. The intersecting, multi-oriented 2D profiles enable 3D interpretation of the gravity and magnetic data.
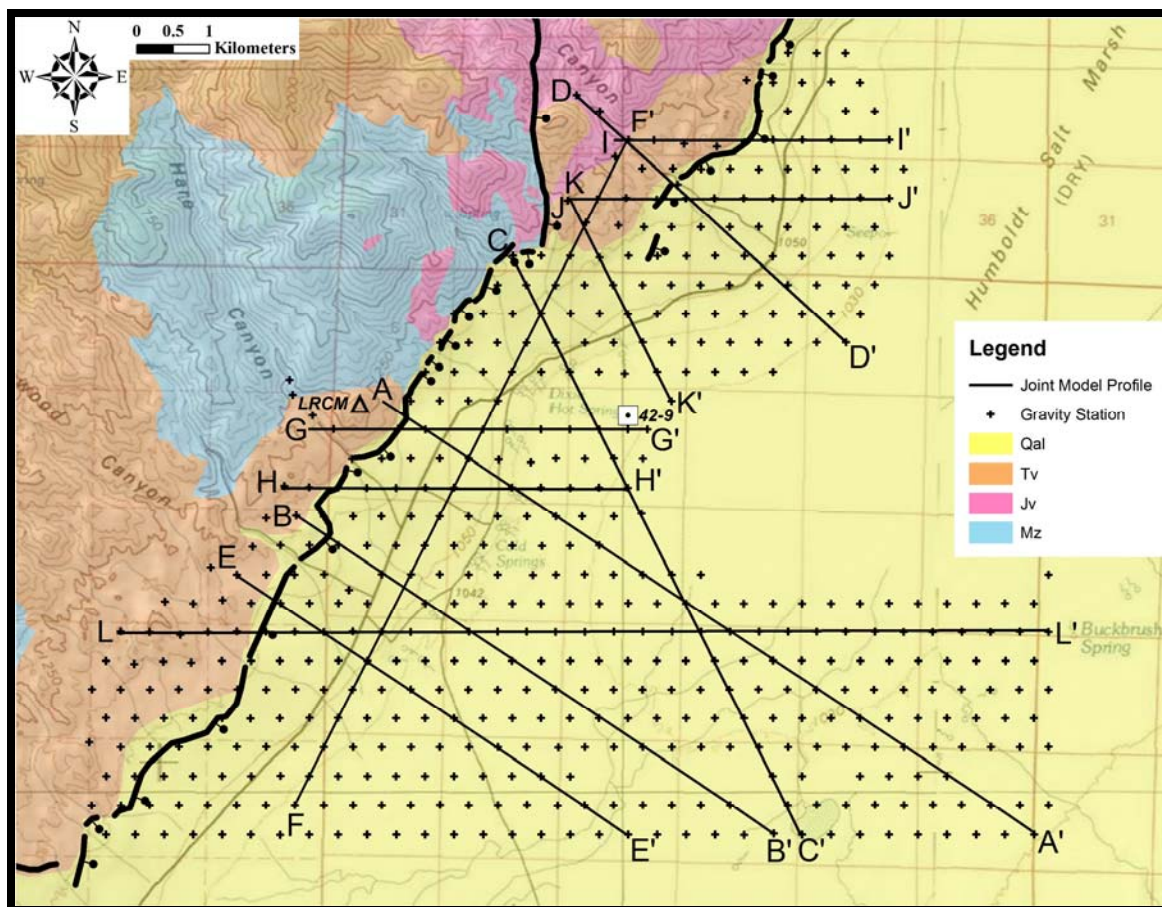
Figure 2.17. Geologic map overlain by dual gravity and magnetic modeling profiles utilized in this study.

Each dual model profile was designed to fit observed gravity and magnetic data with precision (Appendix C). Profile A-A´ is displayed in Figure 2.18 as a sample model result; representative geologic cross-sections (bottom panel) were designed and adjusted to achieve sufficient matches to the observed gravity (middle panel) and magnetic (top panel) data. GM-SYS provides real-time calculations of the root-mean-square deviation (RMSD) of the gravity/magnetic data fit, enabling the user to adjust the polygonal bodies in the model until an acceptable fit is achieved. RMSD is a scale-dependent statistic; therefore, RMSD values were normalized (NRMSD) by the maximum and minimum observed gravity/magnetic values. Statistics for all 12 model profiles are presented in

Table 2.6. Models all match within 2% NRMSD of observed magnetic data and within 1% NRMSD of observed gravity data.

The key geologic units modeled in this study are the relatively low-density basin fill and the relatively magnetic Jurassic volcanics (e.g., Figure 2.18, bottom panel). Profile G-G' was used as a "test profile" to establish modeling parameters of these geologic units (Figure 2.19), in contrast with bedrock at a density of 2.67 g/cc and no magnetic susceptibility. A basin fill density of 2.17 g/cc was attempted first, after Schaefer (1983). This value produced a basin fill depth exceeding that encountered by well 42-9, indicating a smaller basin fill density should be used. Basin fill densities of 1.97 and 2.07 g/cc were also attempted, each of which are reasonable for unconsolidated basin sediments (Schaefer, 1983). 1.97 g/cc generated too shallow a basin fill depth with respect to well 42-9, but 2.07 g/cc yielded a good fit and was thus selected as the basin fill density (Figure 2.19).

Identification of a suitable magnetic susceptibility for the Jurassic volcanics was less straightforward; in the G-G' profile, well 42-9 only rules out the possibility of 0.004 cgs since no Jurassic volcanics were encountered in the well. A susceptibility of 0.007 cgs was selected, as this value corresponds to preliminary results of GM-SYS modeling performed by R. Karlin (2013, personal communication) in northern Dixie Valley, where the dimensions and distribution of the subsurface Jurassic volcanics are better constrained by well data. Note that altering the magnetic susceptibility of the Jurassic volcanics generally changes the thickness of the bodies, rather than their depths (Figure 2.19).

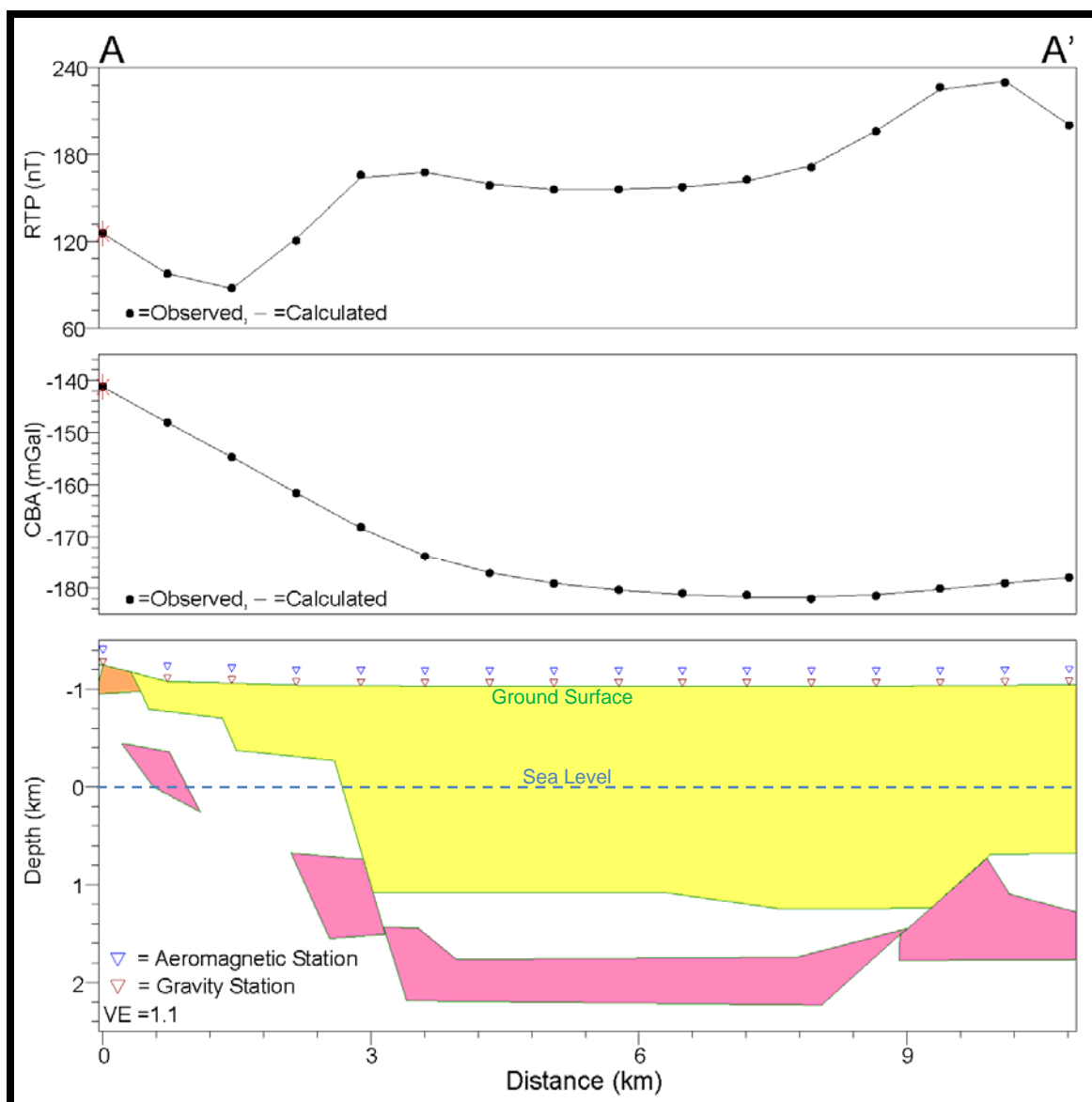Figure 2.18. Dual model profile A-A'. Top panel: observed and calculated CBA gravity. Middle panel: observed and calculated RTP magnetism. Bottom panel: 2D model cross-section; VE = vertical exaggeration; yellow = basin fill, orange = Tertiary volcanics, magenta = Jurassic volcanics, white (below ground surface) = bedrock; note the semi-vertical offsets of the basin fill and Jurassic volcanic units.

Table 2.6. Statistical precision of dual model profiles.

Model Profile Statistics: Magnetics				
Profile	**Max Obs RTP (nT)**	**Min Obs RTP (nT)**	**Model RMSD**	**NRMSD (%)**
A-A'	229.65	87.59	0.974	0.69
B-B'	226.45	159.45	0.871	1.30
C-C'	201.00	92.89	0.456	0.42
D-D'	244.59	83.18	1.916	1.19
E-E'	228.23	158.45	0.874	1.25
F-F'	228.65	80.75	2.744	1.86
G-G'	190.48	80.75	0.384	0.35
H-H'	216.12	95.84	1.210	1.01
I-I'	211.49	67.92	0.421	0.29
J-J'	238.56	98.33	0.827	0.59
K-K'	238.89	107.35	0.148	0.11
L-L'	270.36	121.81	1.153	0.78

Model Profile Statistics: Gravity				
Profile	**Max Obs CBA (mGal)**	**Min Obs CBA (mGal)**	**Model RMSD**	**NRMSD (%)**
A-A'	-141.24	-182.02	0.162	0.40
B-B'	-147.42	-181.84	0.120	0.35
C-C'	-138.28	-182.19	0.172	0.39
D-D'	-128.50	-169.38	0.153	0.37
E-E'	-149.53	-180.79	0.202	0.65
F-F'	-133.47	-169.67	0.169	0.47
G-G'	-140.11	-168.41	0.081	0.29
H-H'	-143.51	-172.23	0.108	0.38
I-I'	-132.83	-160.24	0.132	0.48
J-J'	-137.67	-162.85	0.104	0.41
K-K'	-137.67	-166.84	0.058	0.20
L-L'	-144.39	-181.50	0.357	0.96
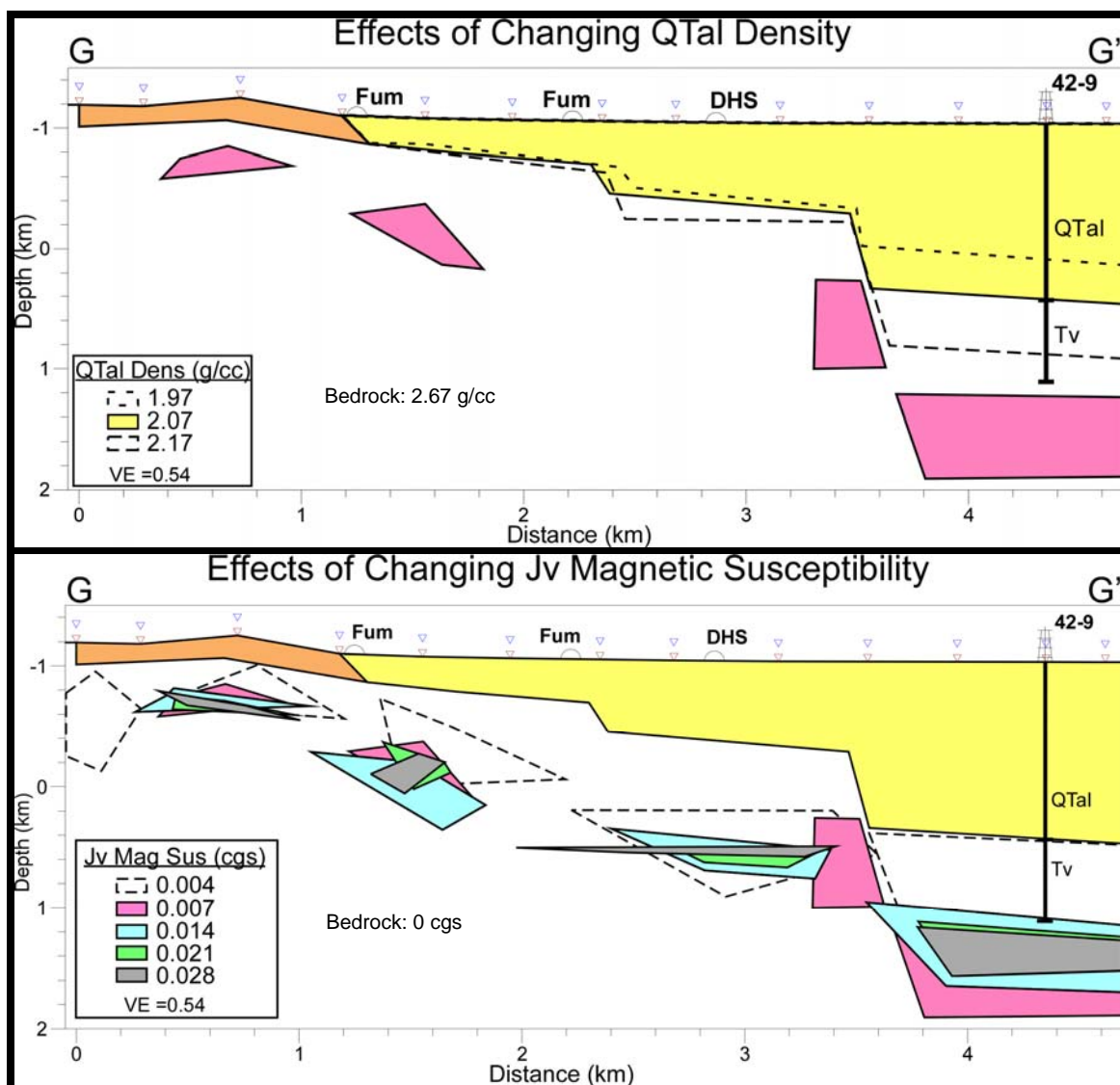
Figure 2.19. Model variants of profile G-G' produced from altering basin fill (QTal) density (top panel) and Jurassic volcanic (Jv) magnetic susceptibility (bottom panel), distinguished from bedrock values. A basin fill density of 2.07 g/cc and a Jurassic volcanic magnetic susceptibility of 0.007 were selected as the parameters of best fit. The depicted 42-9 well path is not the true well path; it shows the true vertical depth of lithologic units encountered by the well, projected under the well collar. Fum = fumarole, DHS = Dixie Hot Springs, for reference. VE = vertical exaggeration.

The twelve profiles were all modeled using the same parameters for each 2D cross-section. The geophysical parameters for the modeled geologic units are presented in Table 2.7, and Figure 2.20 displays the 12 model cross-sections. Gravity modeling was

utilized to model the basin geometry and near-surface Tertiary volcanic units, and magnetic modeling shows the distribution of the Jurassic volcanics (Figure 2.20). Cross-sections A-A', F-F', G-G', and H-H' each traverse the magnetic low between LRCM and well 42-9 (Figures 2.16 and 2.17). This could be modeled in the 2D cross-sections as a depositional "gap" in the Jurassic volcanics (e.g., Figures 2.18 and 2.19). However, given that the Jurassic volcanics are generally laterally continuous (albeit vertically offset) in the dual model cross-sections, a gap seems unlikely. The magnetic low spatially correlates with surficial hydrothermal expressions (i.e., the fumaroles, the Dixie Hot Springs, and maximum near-surface temperatures). It follows that the magnetic low is likely caused by hydrothermal upflow and alteration that has locally demagnetized the Jurassic volcanics (e.g., Bruhn et al., 2010). Thus, the magnetic low is modeled in the cross-sections by hydrothermally altered, demagnetized Jurassic volcanics (Figure 2.20 and Table 2.7). Note that hydrothermally altered Jurassic volcanics are not differentiated by dual modeling. These units have geophysical properties equivalent to bedrock (Table 2.7). The geometry of these units is topologically and geologically inferred from the surrounding Jurassic volcanic units; their dimensions are otherwise unconstrained.

Table 2.7. Representative geologic units, and their geophysical properties, for dual model profiles.

Model Unit	Density (g/cc)	Mag Sus (cgs)	Symbol	Description
Background	2.35	0.000		Bouguer reduction density
Bedrock	2.67	0.000		Pre-Quaternary rocks
QTal	2.07	0.000		Quaternary/Tertiary alluvial and lacustrine basin fill
Tv	2.30*	0.000		Tertiary volcanics**
Jv	2.67	0.007		Jurassic volcanics (Humboldt igneous complex)
Jvha	2.67	0.000		Hydrothermally altered Jv (no longer magnetic)

* Density of near-surface Tertiary volcanics after Abbott , Louie, Caskey, & Pullammanappallil (2001).
** Tertiary volcanics, primarily constituting of late Oligocene tuffs, are generally porous/vesicular and relatively low density material; burial and overburden pressurization induces compression that tends to increase the density of the tuffs to that of nominal bedrock at 2.67 g/cc (e.g., Tv encountered in 42-9).
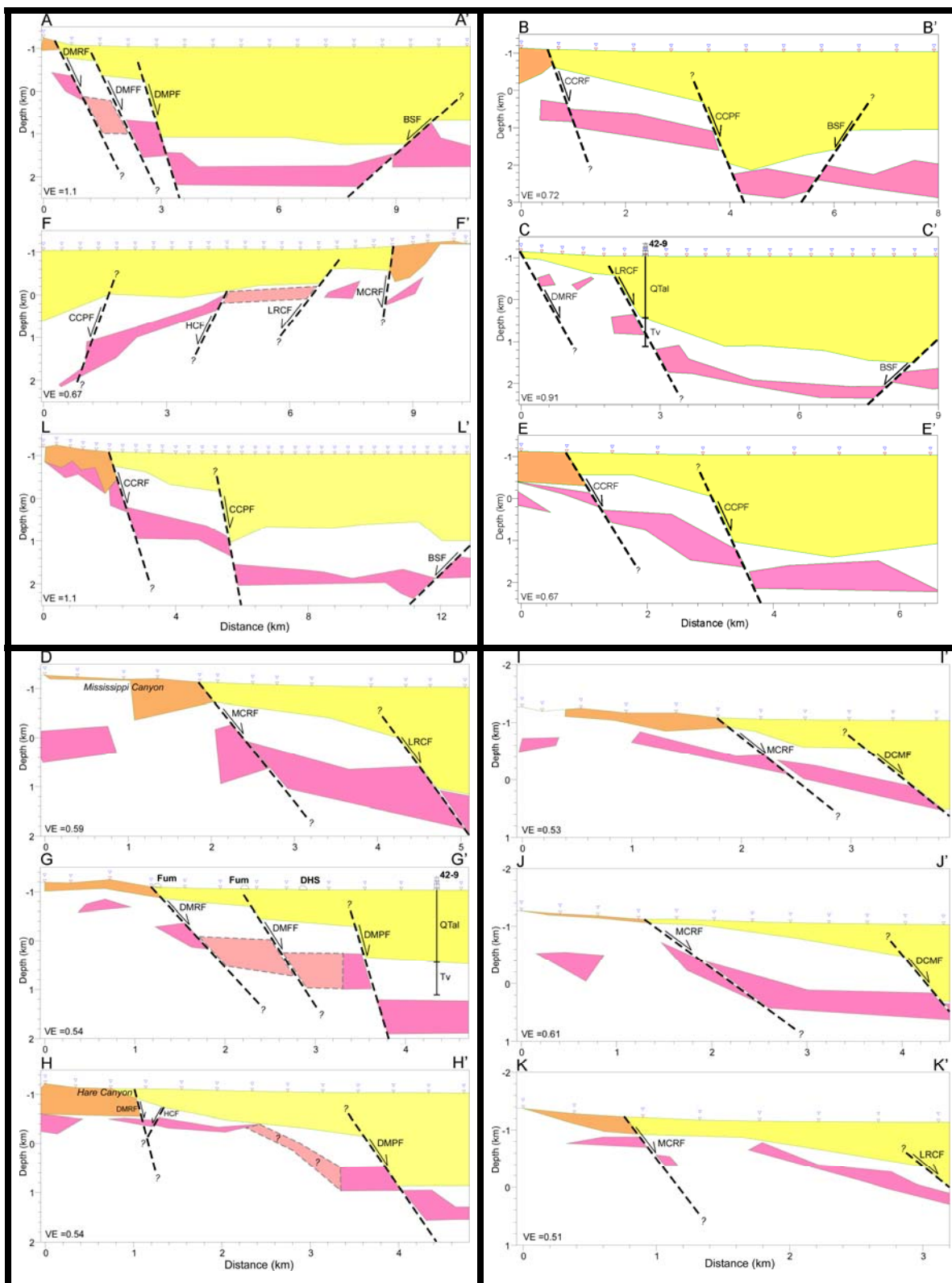
Figure 2.20. Dual model cross-sections, with normal fault segments and demagnetized Jurassic volcanics.

The 2D cross-sections were modeled with fault structure in the subsurface. Faults are delineated by 1) lateral juxtaposition of basin fill and bedrock and 2) vertical displacement of Jurassic volcanic units. The 2D dual model profiles delineate 10 normal fault segments of varying throw and define basin fill depths (Figure 2.20). Table 2.8 presents a summary of the identified normal fault segments, their approximate cumulative offset, and the cross-section profiles the faults were interpreted from. The faults exhibit normal offset and moderate to steep dip angles. A zone of piedmont faults (after Blackwell, Wisian, Benoit, & Gollan, 1999) contribute the largest offset ($\geq$1 km), and the basin fill is accordingly deepest in the hanging wall of these faults. In contrast, basin depths in the intra-basin zone – i.e., the area between the rangefront and piedmont faults – are relatively shallow. Similarly, cumulative fault offset of the rangefront and intra-basin faults are no more than a few hundred meters.

Table 2.8. Delineated fault segments, approximate total offset, and the dual model profiles they correspond to (Figure 2.20).

Label	Fault Segment Name	Approximate Cumulative Offset (Profiles)
BSF	Buckbrush Spring fault	0.5 km (A-A', B-B', C-C', L-L')
CCPF	Cottonwood Canyon piedmont fault	1.2 km (B-B', E-E', F-F', L-L')
CCRF	Cottonwood Canyon rangefront fault	0.2 km (B-B', E-E', L-L')
DCMF	Dixie Comstock Mine fault	0.5 km (I-I', J-J')
DMFF	Dixie Meadows fumarole fault	0.2 km (A-A', G-G')
DMPF	Dixie Meadows piedmont fault	1.4 km (A-A', G-G', H-H')
DMRF	Dixie Meadows rangefront fault	0.3 km (A-A', C-C', G-G', H-H')
HCF	Hare Canyon fault	0.2 km (F-F', H-H')
LRCF	Little Rock Candy fault	1.0 km (C-C', D-D', F-F', K-K')*
MCRF	Mississippi Canyon rangefront fault	0.4 km (D-D', F-F', I-I', J-J', K-K')

* Cumulative offset on the LRCF appears to decrease from the basin towards the range.

2.4.3.3 3D model

The 2D cross-sections from GM-SYS were imported into Leapfrog for 3D modeling. Prior to importing the cross-sections, the model was initiated by importing

topography from a 10 m digital elevation model (Figure 2.21). Well collar locations and

drill paths were also imported, with the basin fill and bedrock intervals included (Figure

2.21). Cross-sections were georeferenced and imported into Leapfrog (Figure 2.22).
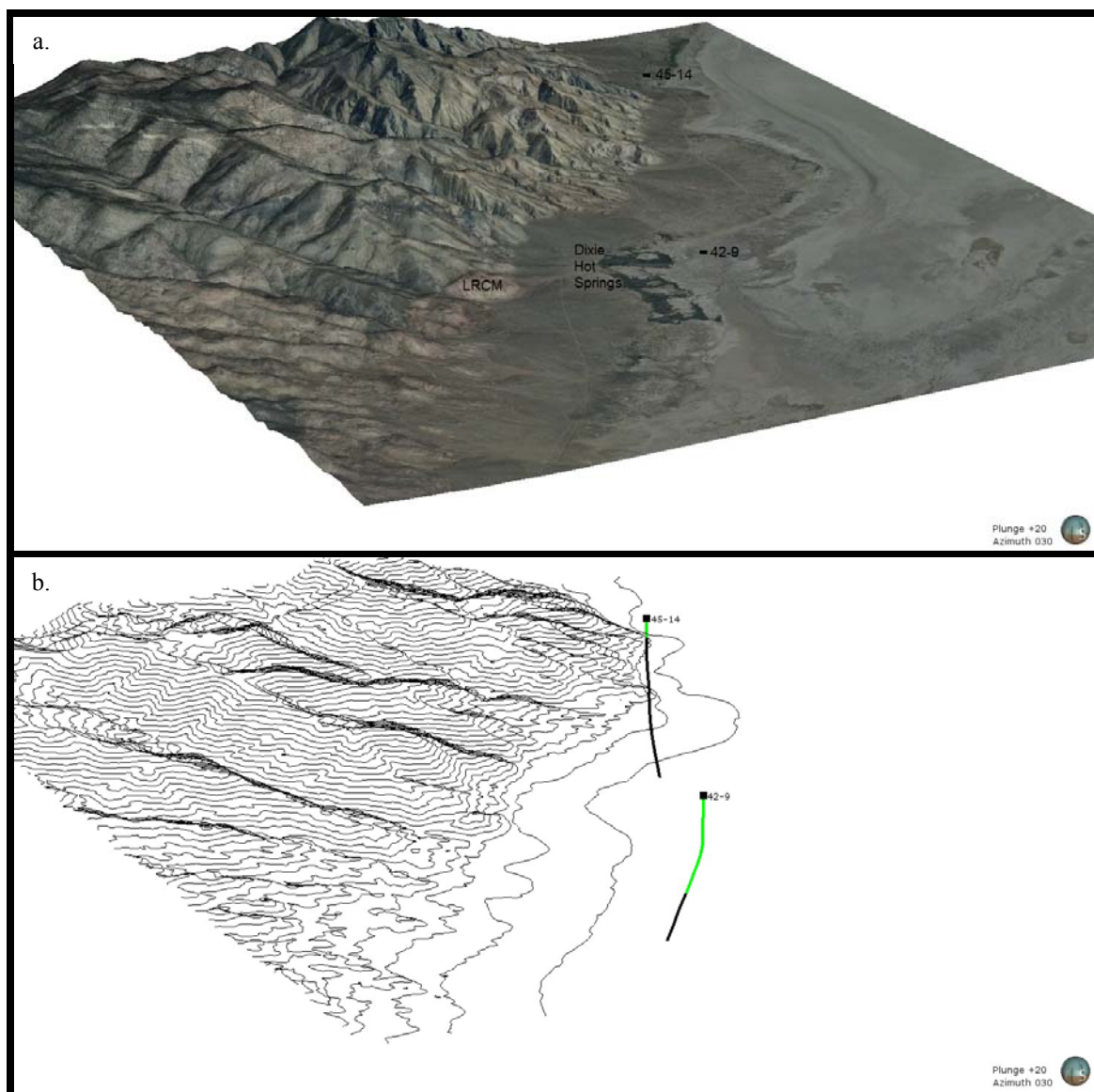
Figure 2.21. Images of Leapfrog 3D model topography. View perspectives of all Leapfrog images are in the lower right of each image; in this case "Plunge +20" = looking from 20° above horizontal, and "Azimuth 030" = looking 30° from north. All images are presented with no vertical exaggeration. (a) Topography with satellite imagery draped and surface features annotated for spatial reference. (b) Topography represented by black contour lines (contour interval: 50 m). Wells 42-9 and 45-14 are also displayed with generalized lithologic intervals (green = basin fill, black = bedrock).
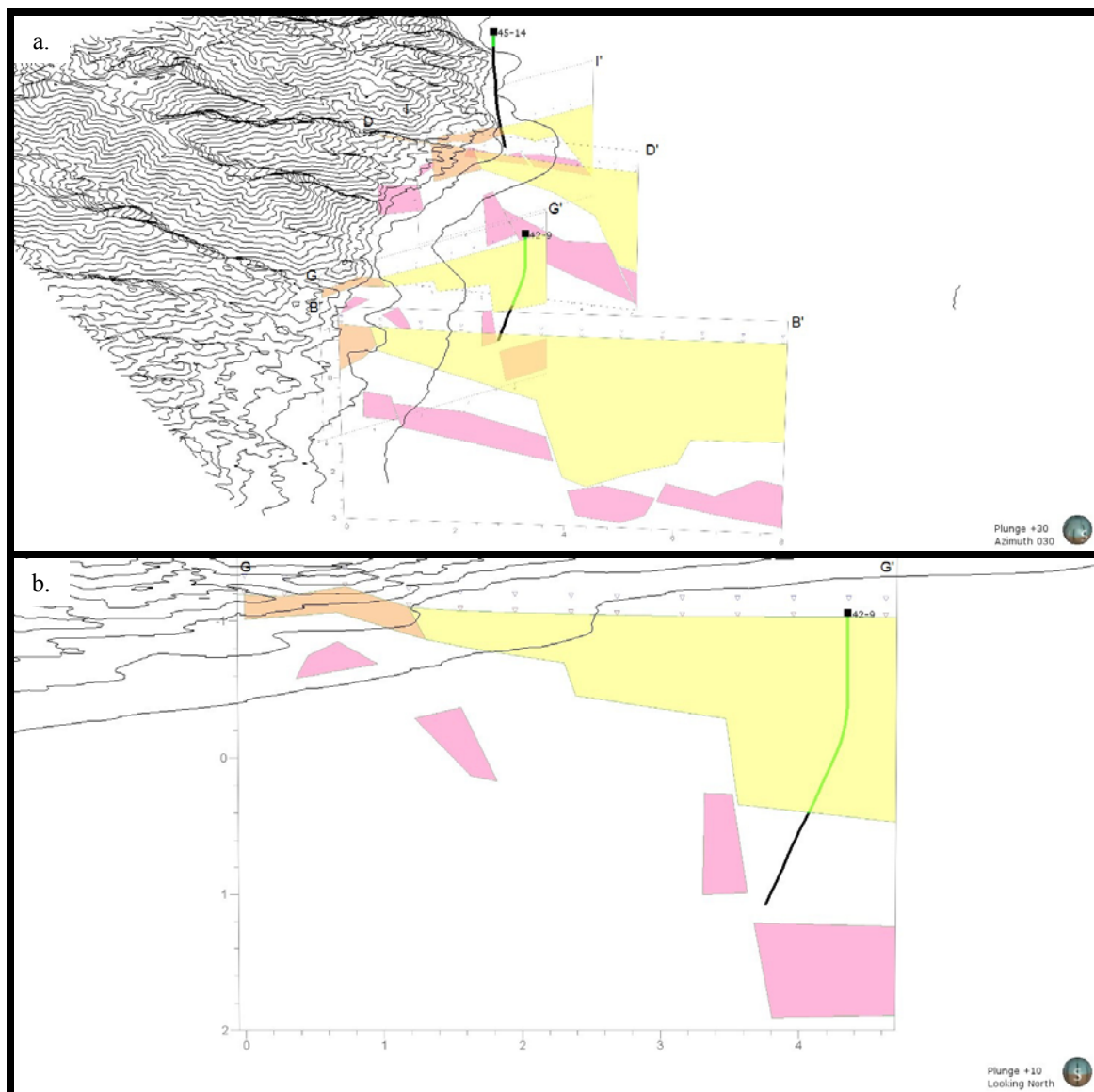
Figure 2.22. (a) Leapfrog image featuring four of the twelve 2D cross-sections imported from GM-SYS. The cross-sections are displayed semi-transparently. (b) Semi-transparent cross-section G-G' in front of well 42-9, highlighting the cross-section fit to well lithology.

Fault meshes were implicitly modeled based on the twelve cross-sections (Figure 2.20) and the added constraints of the well data and surface faults (section 2.4.2). The eastward-dipping rangefront fault segments (Table 2.8) were modeled as a single mesh;

the fault strike was constrained by the surface traces of the fault scarps, and dip was controlled by the cross-sections and the fault intersection with well 45-14 (Figure 2.23).

Figure 2.23. Opposing perspectives of the rangefront fault mesh and four of the cross-sections that help define it. The hanging wall side of the fault is colored blue, the footwall side is red. Note the fault intersection with well 45-14 (bottom panel).

Eastward-dipping piedmont fault segments CCPF and DMPF (Table 2.8, Figure 2.20) were modeled as a single mesh (Figure 2.24). This fault terminates against the

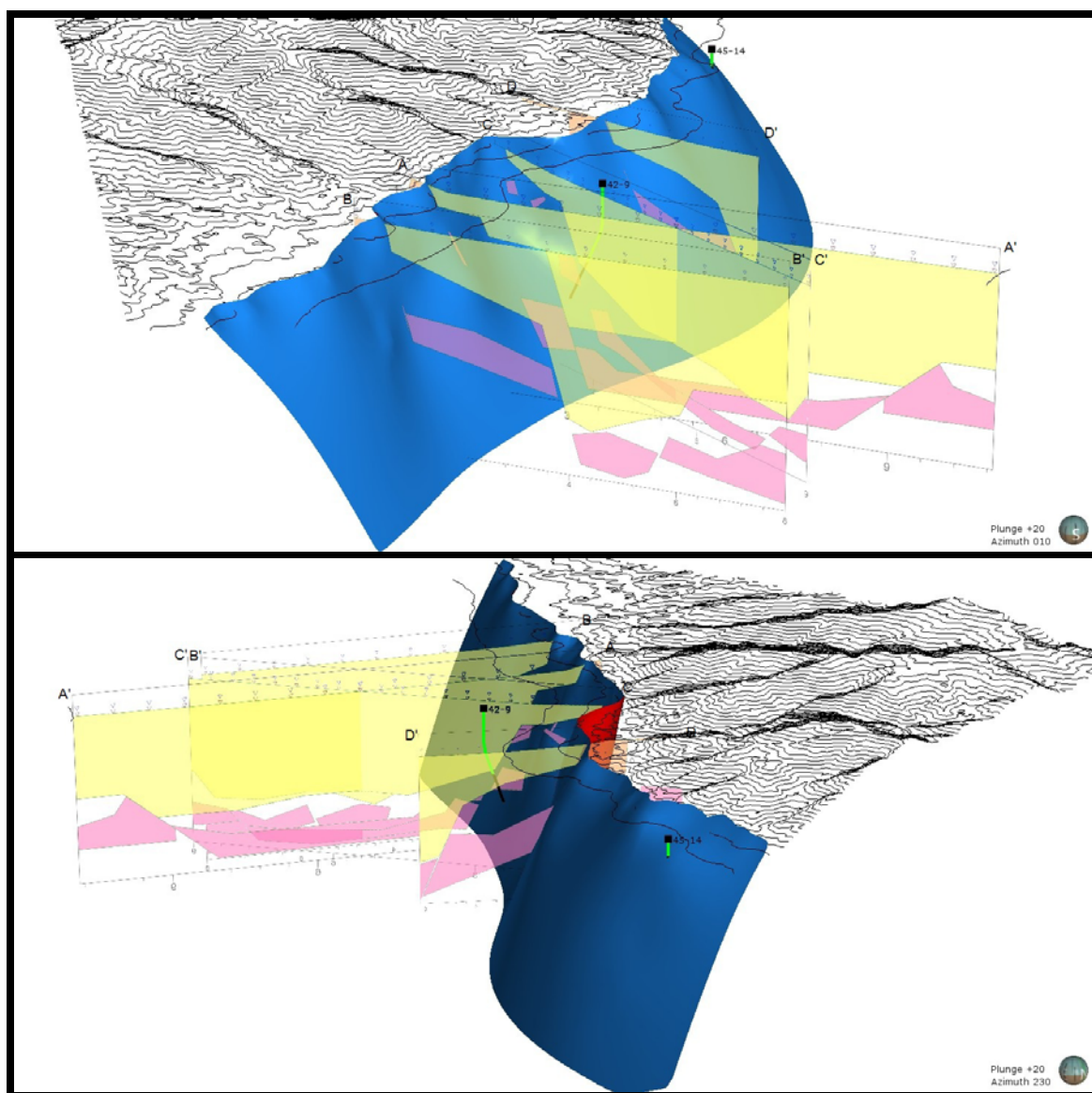LRCF segment. The east-northeast-striking LRCF and north-striking DCMF were modeled as a single fault, intersecting the rangefront near LRCM and merging with the rangefront to the north (Figure 2.24). Fault 4, from Figure 2.12, was modeled as the surface expression of the LRCF segment, and similarly fault 1 is the surface expression of the HCF segment. It is not clear whether or not the LRCF continues across the northwest-striking HCF (Figure 2.12); the LRCF was modeled terminating against the HCF in Leapfrog. The HCF (Figure 2.25) is modeled as a single mesh that terminates against the DMPF to the east, and is truncated just west of the rangefront fault since there is no data control on fault attitude and cumulative displacement of the HCF in Hare Canyon. To the north of the HCF, the DMFF is modeled as a short, north-northeast-striking fault splay that intersects the LRCF to the north, and diminishes to the south (Figure 2.26). On the east side of the basin, the BSF dips westward in conjunction with the cross-sections that delineate it (Figure 2.26).
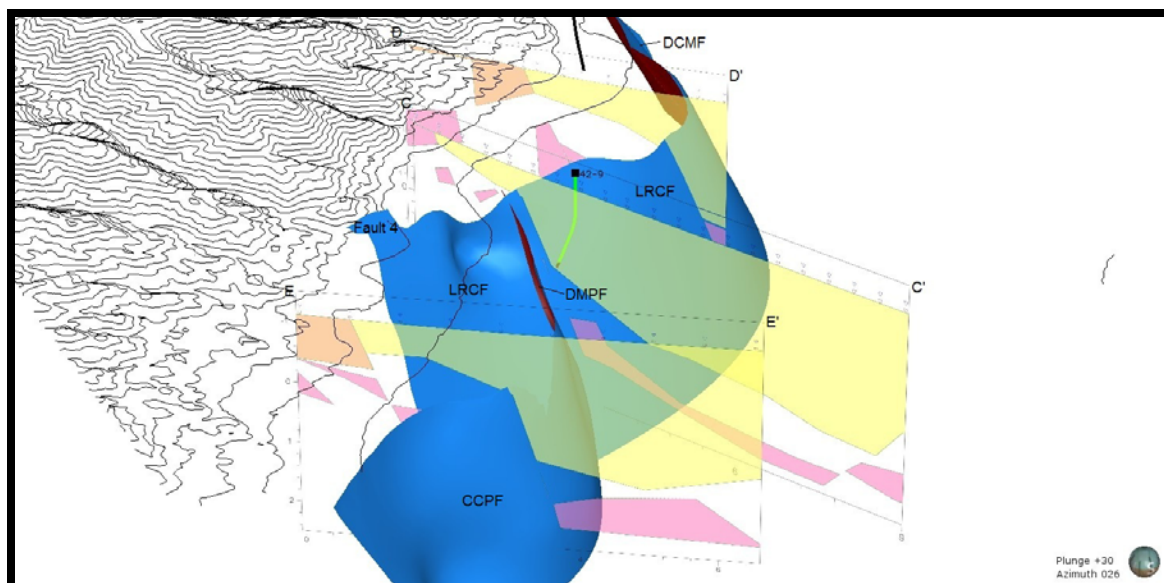
Figure 2.24. CCPF/DMPF and LRCF/DCMF fault meshes and three of the cross-sections they were modeled from (Table 2.8, Figure 2.20). Fault 4 (Figure 2.12) is included as a surface expression of the LRCF segment.
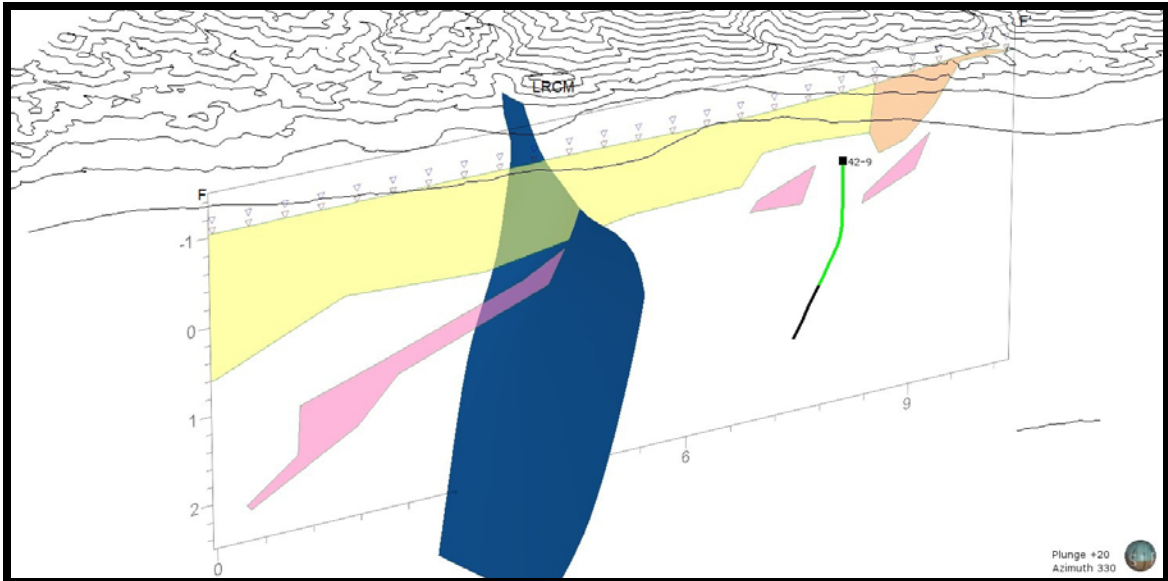
Figure 2.25. Southwest-dipping HCF, delineated in part by cross-section F-F'.
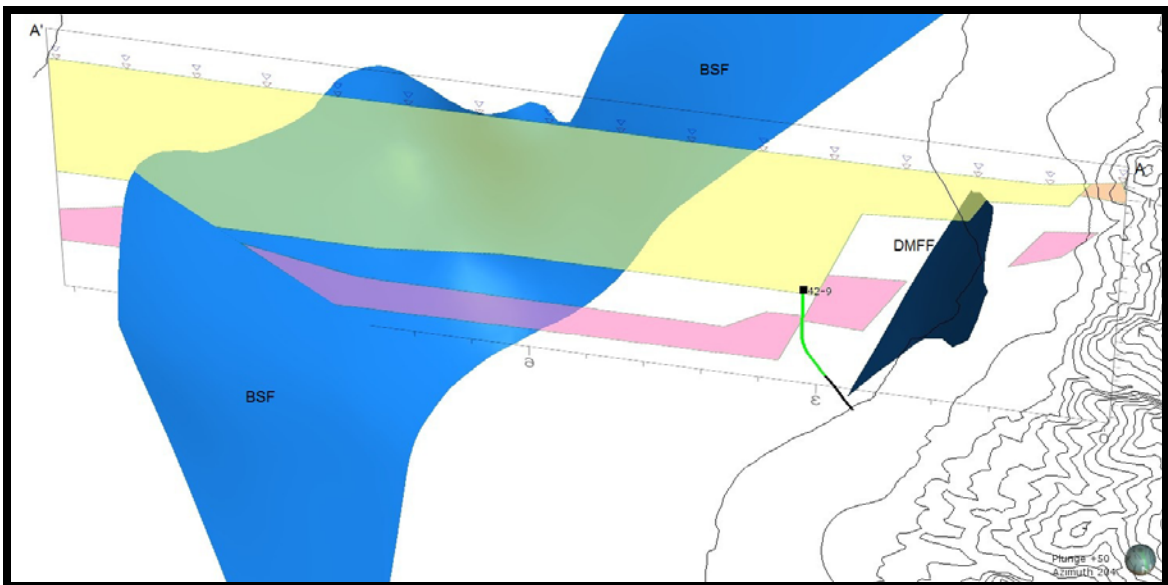
Figure 2.26. Cross-section A-A', viewed towards the southwest in this image, indicates the offsets of the eastward-dipping DMFF and the westward-dipping BSF.

Elevation-slice images of the faults reveal modeled fault architecture with depth. From a near-surface elevation-slice of 1150 m, the dip of north-northeast-trending rangefront fault zone, intersected by the HCF and LRCF, appears to steepen at the right-

step and then flatten as the fault turns northward (Figure 2.27a). At -300 m (below sea-level), the subsurface piedmont and intra-basin faults near the Stillwater Mountains are all visible (Figure 2.27b). The piedmont fault zone appears to diverge from the rangefront from the south, step right near well 42-9 along the LRCF, and merge back into the rangefront fault to the north near well 45-14. The LRCF, DMPF, and HCF define a semi-triangular fault block, cut by the DMFF. At -1500 m elevation, the DMFF is nearly gone, and the moderately- and westward-dipping BSF comes into view (Figure 2.27c). The modeled faults maintain the same structural pattern down-dip to -2300 m elevation (Figure 2.27d) – effectively the upper limit of modeling depth.

Basin geometry was defined in Leapfrog by implicit modeling of the basin fill depths, or depth-to-bedrock, from the 2D cross-sections. All twelve cross-sections and wells 42-9 and 45-14 were utilized to implicitly model a depth-to-bedrock mesh (Figure 2.28). The mesh defines a relatively deep Dixie Valley basin bounded by a shallower intra-basin to the west, towards the Stillwater Mountains (Figure 2.28). East of the deep Dixie Valley basin, bedrock depth decreases as well, but not as dramatically as on the western side. The western intra-basin is bounded by the rangefront fault zone along the Stillwater Mountains (Figure 2.28). The intra-basin loses definition to the north and is no longer visible in the vicinity of well 45-14, where the depth-to-bedrock mesh becomes relatively flat but is also not constrained by dual model cross-sections (Figure 2.28).
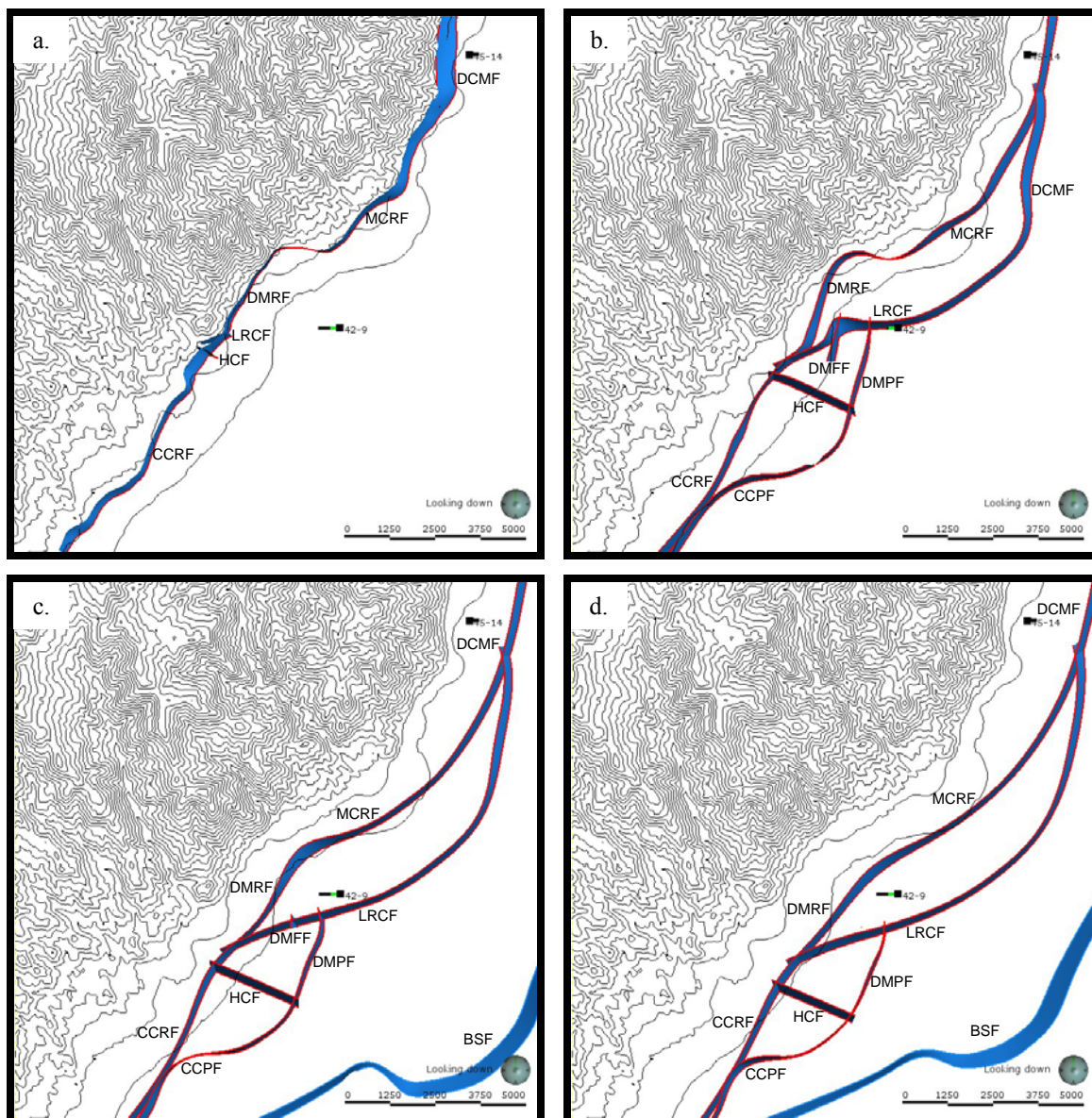
Figure 2.27. Depth-slices of the faults modeled in Leapfrog. The scale at the bottom-right of each image is in meters. Faults are dipping at moderate to steep angles – the faults appear thinner where they are steeply-dipping, and wider where they are moderately dipping. The thickness of each slice is 400 m (200 m above and 200 m below the depth of the slice). Slice elevations: (a) 1150 m; (b) -300 m; (c) -1500 m; (d) -2300 m.
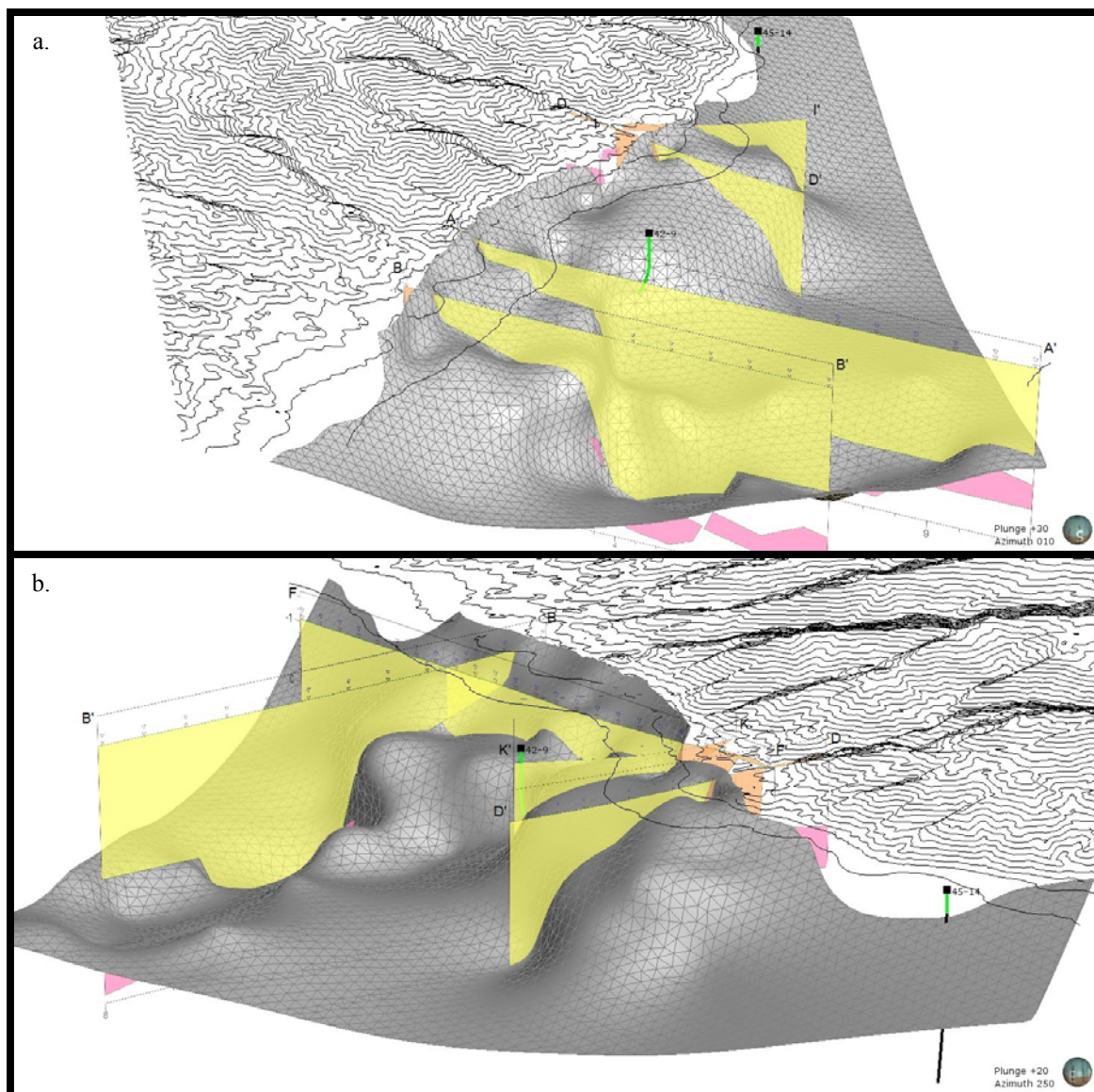
Figure 2.28. Implicitly modeled depth-to-bedrock mesh (grey) based on dual model cross-sections and well lithology data. (a) Northward view, including four of the cross-sections, highlighting the relatively deep Dixie Valley basin bounded by the shallower intra-basin to the west. Basin depth also decreases to the east. (b) Westward view with cross-sections emphasizing the steepness of the intra-basin boundary south of well 45-14. The intrabasin disappears to the north near 45-14.

2.5 Interpretation

Measurements of the fluid at the Dixie Hot Springs and mineralogy at the fumaroles indicates that hydrothermal upflow, occurring beneath the fumaroles,

transitions to lateral outflow at the springs. The sub-boiling thermal fluid at the Dixie Hot Springs is relatively low in solutes (TDS ≤500 ppm) and generally basic (pH ≥8). The gross distributions of these measurements (Figure 2.29) indicate that the thermal fluid is mixing with meteoric groundwater (see also Bohm et al., 1980). Microscope-enhanced observations and XRD/ASD analyses of fumarole samples detected native sulfur, sulfate mineral precipitates, and advanced argillic minerals. Sulfates included gypsum, anhydrite, and alunogen; advanced argillic minerals consisted of kaolinite and alunite (B. Littlefield & J. McCormack, 2012, personal communications). These observations are most analogous to "steaming ground which results from the boiling of steam-heated waters," (Henley, 1985). In this case, illustrated on cross-section G-G′ in Figure 2.30, superheated thermal fluid begins to boil as it rises (due to decreasing confinement pressure), creating hydrogen sulfide-rich vapor that migrates vertically to near-surface, laterally-flowing, meteoric groundwater (Henley, 1985). Migrating upward along permeable conduits (e.g., fault/fracture zones), the hydrogen sulfide oxidizes as it interacts with the atmosphere, forming condensed sulfuric acid (Henley, 1985). Sulfuric acid reacts with the surrounding rocks to produce advanced argillic alteration (M. Coolbaugh, 2012, personal communication) and also undergoes hydrolysis reactions that produce sulfates (J. Moore, 2011, personal communication), as observed at the fumaroles. Meanwhile, the steam-heated, sub-boiling groundwater, characterized by slightly basic pH and a relatively low TDS, continues to flow down the hydrologic gradient on top of the groundwater table until it exits to the surface at the edge of the playa to form the precipitate- and sinter-lacking Dixie Hot Springs (M. Coolbaugh, 2012, personal communication).
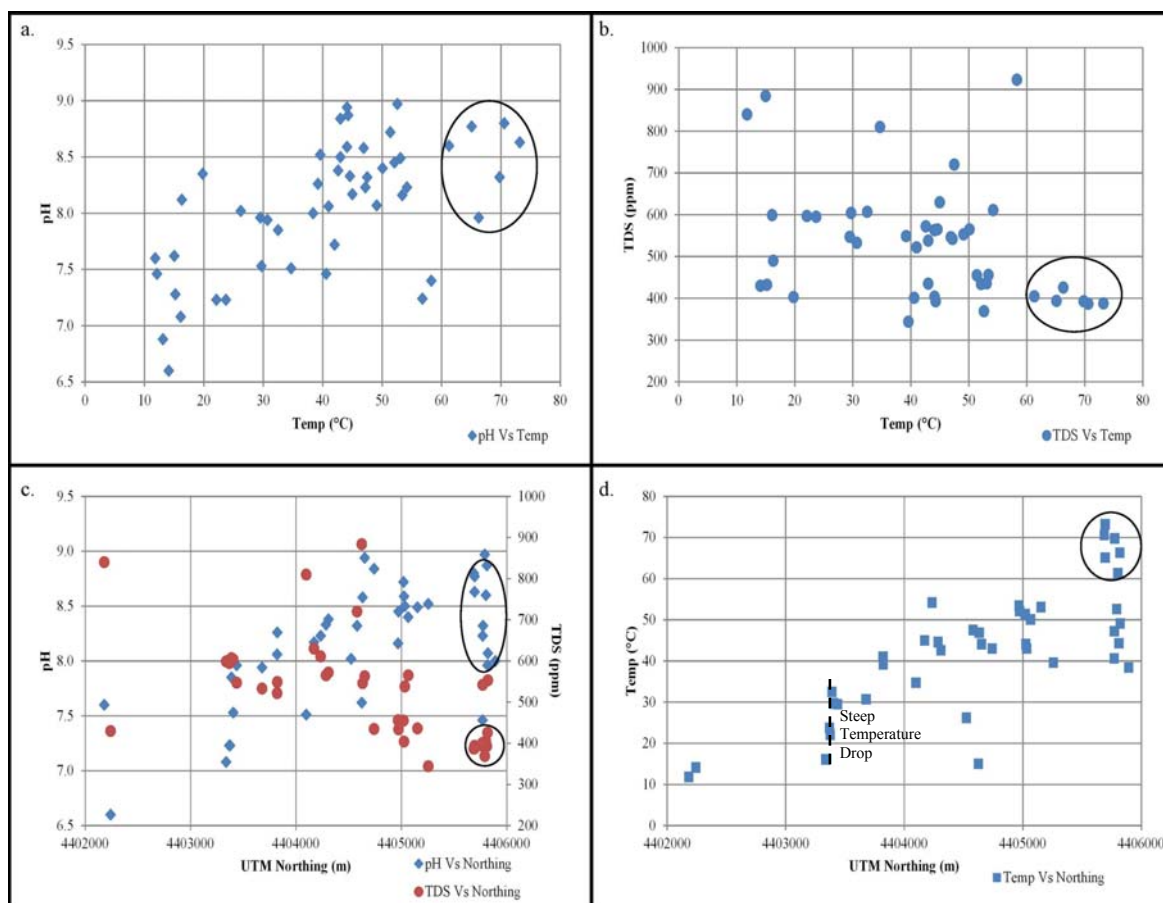
Figure 2.29. Interpretation plots from spring fluid analysis, with measurements from the Dixie Hot Springs indicated by black ovals. (a) Increasing pH with increasing temperature. (b) Decreasing TDS with increasing temperature. (c) Dual axis spatial plot showing increasing pH (blue diamonds) and decreasing TDS (red circles) with increasing northing coordinates, registered to UTM Zone 11N, WGS 84. (d) Increasing temperature with increasing northing coordinates. Note the ~10°C steep temperature drop.
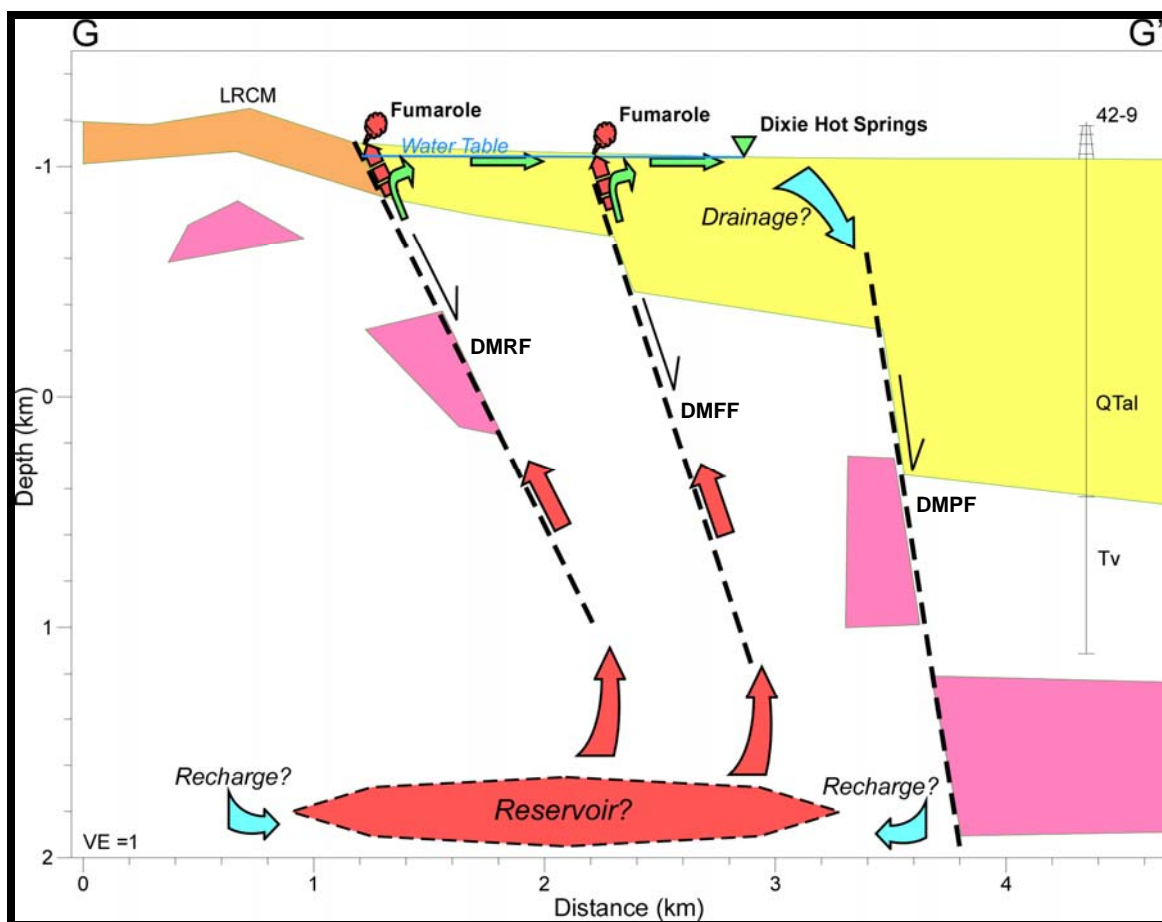
Figure 2.30. Conceptual model of hydrothermal framework on profile G-G'. Colored arrows indicate likely fluid flow paths.

The shallow temperature distribution indicates that thermal fluid flow is structurally controlled. High temperatures are confined to a single thermal anomaly at Dixie Meadows (Figure 2.10). The highest temperatures are aligned along an east-northeast trend from the rangefront fumaroles to the Dixie Hot Springs. Temperatures gradually decrease to the southeast of this trend, and then abruptly drop across a northwest trend emanating out of Hare Canyon (Figures 2.10 and 2.29d). The semi-linear trend from the fumaroles to the Dixie Hot Springs and confinement of the high temperature anomaly are evidence of fault control. Flow appears to be promoted along an

east-northeast-trending fault zone from the rangefront fumaroles to the Dixie Hot Springs, and seems restricted by a northwest-trending fault emanating from Hare Canyon.

The distinctive Tertiary volcanics exposed at LRCM and encountered in well 42-9 correlate to other units recognized in the northern Great Basin and reveal depositional timing constraints. Four distinct units of ash-flow tuffs, labeled $Tt_0 - Tt_3$, and a basaltic dike are summarized in Table 2.9. Tt_1-Tt_3 were correlated by D. John (2012, personal communication). Tt_0 is stratigraphically inferred to be an older tuff, but its visual characteristics are not uniquely distinguishable (C. Henry, 2013, personal communication). However, Tt_0 contains abundant sanidine phenocrysts; a sample of the phenocrysts has been prepared and submitted for $^{40}Ar/^{39}Ar$ dating. The resultant age date will be provided as an addendum to this study as soon as it is available. Age of the basaltic rocks is not definitive from this study, however B. Delwiche (2012, personal communication) inferred that they are likely related to widespread middle Miocene (10-17 Ma) basalts identified in the Stillwater Mountains (e.g., Hudson and Geissman, 1991). In summary, the LRCM tuffs were deposited >25 Ma in the late Oligocene as part of the "ignimbrite flareup" of the western Nevada volcanic field that lasted from 34.4-23.3 Ma (Henry and John, 2013), and appear to have been intruded by a 10-17 Ma basaltic dike.

Table 2.9. Stratigraphic correlation summary of Tertiary volcanics.

Formation	Regional Correlations	Age (Ma)
Tb	middle Miocene basalts	10-17
Tt_3	tuffs of Chimney Spring, New Pass, & Poco Canyon	25.1
Tt_2	tuffs of Nine Hill and Bates Mountain Unit D	25.3
Tt_1	tuffs of Dogskin Mountain and McCoy Mine	29.4
Tt_0	uncorrelated tuffs	>29.4

Regional correlations provided by D. John. References on the regional tuffs:

Tt_3 – tuffs of Chimney Spring, New Pass, & Poco Canyon (Deino, 1989; Henry and Faulds, 2010; John, 1995; McKee and Stewart, 1971);

Tt_2 – tuffs of Nine Hill and Bates Mountain Unit D (Deino, 1989; Gromme et al., 1972; Henry and Faulds, 2010);

Tt_1 – tuffs of Dogskin Mountain and McCoy Mine (Henry et al., 2004; Henry and John, 2013; McKee and Stewart, 1971).

Linear trends in the horizontal gradient of the gravity data delineate the strike of probable normal faults in the basin. Linear maxima of the horizontal gradient (Figure 2.14) are indicative of abrupt, lateral changes in density perpendicular to the strike of the linear trends. Lateral density changes occur where there are geologic variations (i.e., an interface between two geologic units of differing density). In an extensional basin setting, abrupt lateral geologic variations are most likely caused by normal fault offset. Therefore, linear horizontal gradient maxima in the Dixie Meadows basin likely delineate the strike of normal faults. This inference is corroborated by 2D dual modeling.

A prominent magnetic low is associated with localized hydrothermal upflow and alteration. A distinct magnetic low is visible in map view, outlining a primary geothermal target area immediately east of the LRCM rangefront and covering ~3 km^2 (Figure 2.16). The low spatially correlates with the fumaroles, the Dixie Hot Springs, and the near-surface thermal anomaly (Figure 2.10). Dual modeling indicates that hydrothermal upflow is occurring along faults/fractures located within the magnetic low (Figure 2.30).

Thus, the magnetic low is likely caused by hydrothermal upflow and alteration that has locally demagnetized the Jurassic volcanics, as modeled on cross-sections A-A´, F-F´, G-G´, and H-H´ of Figure 2.20.

Secondary potential geothermal targets are identified by magnetic lows and favorable structural patterns. In addition to the primary geothermal target area between LRCM and the Dixie Hot Springs, there are secondary potential targets: one near the mouth of Mississippi Canyon and one southeast of the Dixie Comstock Mine. Both are delineated by relatively low magnetic anomalies (Figure 2.16) and potentially favorable structural settings. The magnetic lows are conspicuous in that they are located at/near Jurassic volcanic exposures (Figure 2.4) that are expected to be strongly magnetic. These magnetic lows could be linked to hydrothermal alteration, similar to the primary target area. The magnetic low at Mississippi Canyon is located to the northeast of the right step-over from the 1954 Dixie Valley ruptures to the Stillwater Seismic Gap ruptures (Figure 2.4). This setting is similar to others in the Great Basin, in which hydrothermal upwelling occurs along fault linkages in a step-over (Faulds et al., 2011). The magnetic low near the Dixie Comstock Mine occurs near the fault intersection of the DCMF and MCRF segments, near well 45-14 (Figures 2.16 and 2.27). The fault intersection may be promoting a narrow zone hydrothermal flow, as evidenced by the high temperatures and low fluid permeability encountered by well 45-14.

The Dixie Valley basin is bounded to the west by a relatively shallow intra-basin at Dixie Meadows. Figure 2.31 is a contour map of the bedrock elevation (bottom of the basin fill) determined from 3D implicit modeling of the 2D geophysical cross-sections in Leapfrog. The basin is divided into two components: the deep Dixie Valley basin and the

shallow intra-basin. The Dixie Valley basin reaches more than 2 km deep in the study area. Basin depths abruptly decrease on the margins bounded by the large-offset piedmont fault zone. A relatively shallow intra-basin, south of the Dixie Comstock Mine, is delineated between the Stillwater rangefront and the piedmont fault zone (Figure 2.31). The shape of the intra-basin is defined by the trends of the bounding rangefront and piedmont fault zones.
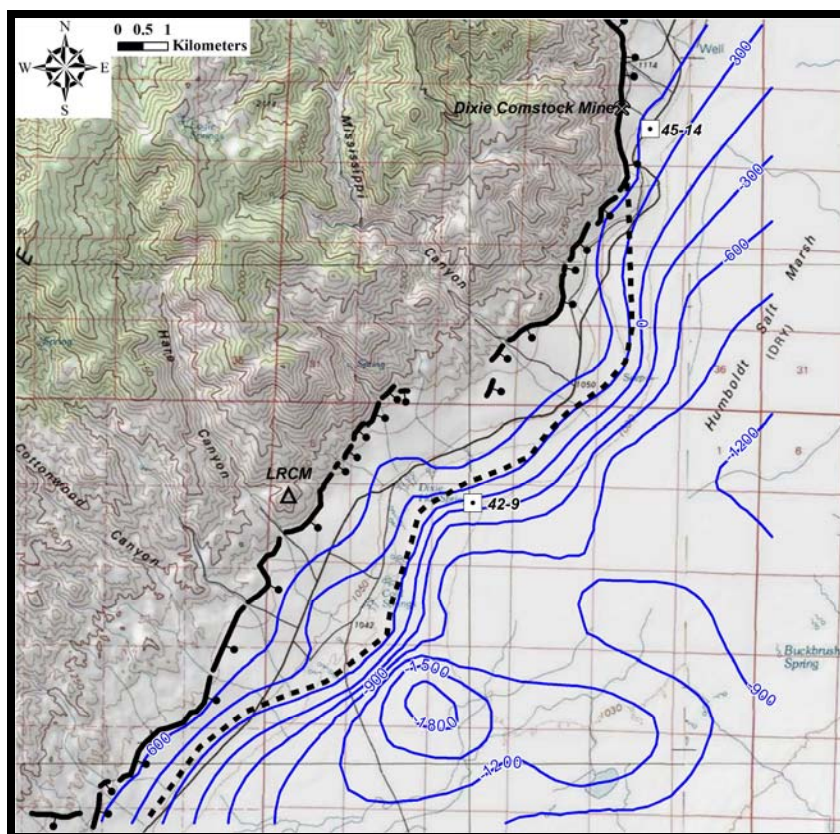
Figure 2.31. Elevation-of-bedrock map with blue contour lines (contour interval: 300 m) generated from the Leapfrog model. Closely-spaced contours are indicative of the piedmont fault zone. The black dashed line denotes the approximate location of the piedmont fault zone trace, separating the Dixie Valley basin to the east from the relatively shallow intra-basin between the piedmont and rangefront fault zones.

A network of exposed and subsurface normal faults of varying attitudes and offsets is delineated. Figure 2.32 presents the surface traces of exposed faults and the traces of subsurface faults in map view. Subsurface traces are surface projections of where these faults cross the bedrock/basin contact in the 3D model. A relatively large-

offset, subsurface piedmont fault zone trends subparallel to the smaller-offset rangefront fault zone; the fault zones appear to link together ~1.5 km south of the Dixie Comstock Mine. The subsurface BSF is likely to be the eastern boundary of the Dixie Valley basin (see also Smith et al., 2001). Faulting is most intricate in the intra-basin between Hare Canyon and the Dixie Hot Springs. The piedmont and rangefront fault zones cut the northwest-striking HCF, intersect/interlink with the LRCF, and are parallel to the short, north-northeast-striking, intra-basin DMFF.

Figure 2.32. Geologic map, adapted from Speed, 1976 (see Figure 2.4), displaying exposed (solid lines) and concealed (dashed lines), faults delineated in this study. Concealed faults are drawn approximate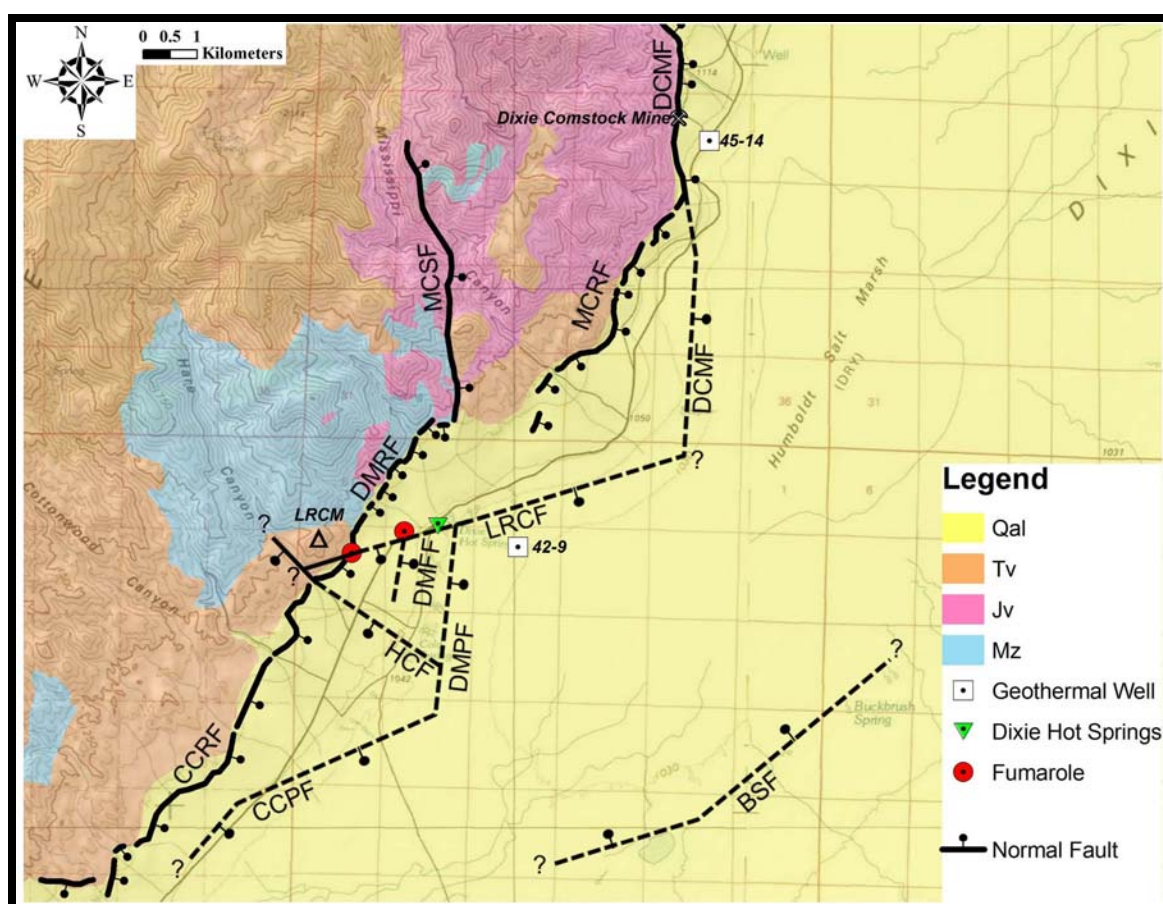ly where they trace the top of bedrock at depth, as determined from Leapfrog modeling. MCSF denotes the Mississippi Canyon fault mapped by Speed, 1976 (no data added to that fault in this study).

Hydrothermal flow appears to be promoted primarily by intersecting faults, though contributions from fault splay and step-over kinematics are also likely. The two fumaroles at Dixie Meadows are situated near intersections of the north-northeast-striking, east-southeast-dipping DMRF and DMFF with the east-northeast-striking, south-southeast-dipping LRCF (Figure 2.32). Hydrothermal flow appears to be promoted along-strike of the LRCF; intersections with the DMRF and DMFF are likely to create dilatant, semi-vertical fracture conduits that may promote upflow (e.g., Figure 2.30). The DMFF is interpreted to be a relatively short fault splay in the intra-basin (Figure 2.32). This fault splay may be a result of stress accommodation due to fault endpoint interaction (e.g., Caskey and Wesnousky, 2000) or perhaps due to the right step-over of the rangefront and piedmont faults in the vicinity (Figure 2.32).

Other faults represent hydrothermal boundaries. The northwest-striking, southwest-dipping HCF spatially correlates with the southwestern boundary of the Dixie Meadows thermal anomaly (Figures 2.29 and 2.32). The north-northwest-striking, east-southeast-dipping DMPF appears to form the eastern hydrothermal boundary (Figure 2.32). It is possible, though speculative, that these boundary faults are the fluid recharge margins for the geothermal reservoir (e.g., Figure 2.20).

Modeled fault offsets indicate that the inception of rangefront faults is younger than that of the piedmont faults. Fault offsets determined from 2D dual modeling (Table 2.8) indicate that rangefront faults have accommodated a fraction of displacement compared to the piedmont faults (see also Blackwell et al., 1999). It is not clear how much slip the concealed piedmont faults accommodate in proportion to the rangefront faults as extension continues. However, the interpreted basin depths (Figure 2.31) suggest

that the piedmont faults represent the rangefront margin of an ancestral Dixie Valley, perhaps dating back to the inception of middle to late Miocene extension (e.g., Vikre, 1994). Faulting of the modern rangefront began in the Quaternary, and has likely shared displacement with the piedmont faults ever since (Bell and Katzer, 1990).

The normal faults delineated in this study may be indicative of three extensional generations. The current generation is defined by west-northwest extension primarily characterized by abundant and historically active north-northeast-striking normal faults that began 8-10 Ma. The two landslides identified on LRCM (section 2.4.2) have not been analyzed in detail for timing constraints, but they appear to be remnants of a large seismic event in the late Quaternary (e.g., perhaps the Stillwater Seismic Gap event). East-northeast-striking faults (e.g., the LRCF) may be associated with sinistral-normal faulting characteristic of the HSZ. The previous generation is associated with north-striking faults (e.g. DCMF) from middle to late Miocene extension. Inheritance of the north-oriented structural fabric from this extensional episode appears to influence the right step-over kinematics of the younger north-northeast-striking faults (e.g., Figure 2.4), in addition to producing dilatant fault intersections. The oldest generation is related to the northwest-striking HCF. Northwest-striking faults in the Stillwater Mountains have been associated with late Oligocene to early Miocene extension. Offset of the Tt_3 unit across Hare Canyon (section 2.4.2) infers post-depositional fault displacement, < 25.1 Ma, occurred on the HCF approximately ≤ 2 Ma after Tt_3 deposition (Hudson and Geissman, 1991).

The superposition of these structural phases may be the most critical factor in structural control of hydrothermal fluid flow. No single fault zone or orientation appears

solely accountable for hydrothermal control; rather, dynamic fault interactions seem to have greatest influence. Fault intersections and stepovers, as well as faults interpreted to be hydrothermal barriers, delineated in this study appear to be direct results of temporal structural overlapping. Multiple phases/orientations of regional extension and localized fault segment interaction, in other words, are the likely primary driving forces behind structural control of hydrothermal zones at Dixie Meadows and other geothermal locales in the Great Basin.

2.6 Conclusions

This study demonstrates the interpretive power of dual analysis and modeling of gravity and magnetic data, and highlights the importance of data integration to interpret subsurface structure. Patterns observed in both gravity and magnetic data maps delineate previously unrecognized subsurface structural features and potential exploration targets in greater detail than is possible with only one of the data sets. Precision 2D dual profile modeling of gravity and magnetic data reveals subsurface basin and fault structures in cross-section, and profiles can be oriented to develop a comprehensive and testable 3D model. Integration of the geophysical analyses with hydrothermal surface expression assessment and geological observations enables interpretive refinement and supplies important modeling constraints.

A primary geothermal target area at Dixie Meadows appears to be confined within the intra-basin. A low magnetic anomaly, a high near-surface temperature anomaly, and fumarole zones are indicative of localized upflow within the intra-basin. Geothermal upflow in this target area, associated with the fumaroles and advanced argillic alteration,

appears to be promoted along subvertical, intra-basin fracture zones at the intersections of faults that have likely been active since 8-10 Ma; i.e., where the east-northeast-striking LRCF intersects with the DMRF and the DMFF splay that each strike north-northeast (Figure 2.32 and Table 2.8). Geothermal activity appears to be laterally restricted by the approximately 25-23 Ma, northwest-striking HCF, the north-northeast-striking DMPF that probably first developed during the middle to late Miocene, and the DMRF.

The integrated approach employed in this study is the key factor in developing a relevant conceptual geothermal flow model, identifying likely structural controls and exploration targets, and interpreting a structural chronology at Dixie Meadows – the latter of which may be the overarching mechanism behind structural control of hydrothermal fluid flow. The methodology and findings of this study will hopefully aid in further exploration and potential development of the Dixie Meadows geothermal prospect, and are likely applicable to other geothermal prospects and systems in the Great Basin.

~

"If I have seen further than others, it is by standing upon the shoulders of giants."

Isaac Newton

Chapter 3: Summary and Recommendations

Dual gravity and magnetic interpretation and modeling at Dixie Meadows reveal a hidden network of piedmont and intra-basin faults. Linear gravity gradients and magnetic contrasts are indicative of fault strike. Dual gravity and magnetic profile modeling delineates approximate fault dip, ranging from moderate to steep, and estimated cumulative offset. 3D interpolative modeling of the dual model cross-sections delineates a large-offset piedmont fault zone separating the deeper Dixie Valley basin from the shallower intra-basin. Faults along the rangefront and within the intra-basin have less offset than the piedmont faults; however, there appear to be more fault intersections and stepovers in the rangefront/intra-basin zone. Geologic information from this study and previous works suggest that discrete Cenozoic extensional phases produced the network of intersecting and interlinking faults at Dixie Meadows.

Geothermal targets identified in this study are characterized by both geologic and geophysical patterns. The primary geothermal target is evidenced by expressions at the surface, analysis of which aided in producing a conceptual hydrothermal model. Geothermal upflow in the primary target area appears largely controlled by intersecting faults identified at the surface, as well as by the dual modeling. A distinct magnetic low at the target is associated with demagnetization caused by advanced argillic hydrothermal alteration. Secondary geothermal targets are similarly associated with low magnetic anomalies and favorable geologic structures (a fault step-over and a fault intersection).

The 3D model and proposed targets from this study ought to be integrated into a broader geothermal exploration program at Dixie Meadows. Increased gravity and magnetic data coverage may prove instructive; for instance, expanding gravity coverage to the northeast may add more information about piedmont, and possibly more intrabasin, faulting near Buckbrush Spring and well 45-14. Coverage in the Stillwater Mountains may also prove useful in more clearly identifying the gravity and magnetic properties of bedrock. Dual 3D modeling of the gravity and magnetic data, as opposed to 2D profile modeling converted to a 3D model as performed in this study, is recommended if coverage can be increased. Integration with 3D magnetotelluric surveying may be utilized for further insights on fault characteristics, as well as estimation of reservoir location, volume, and fluid circulation (e.g., Wannamaker, Maris, Sainsbury, & Iovenitti, 2013). Another option towards those ends may be airborne electromagnetic surveying and 3D inversion (e.g., Devriese et al., 2012). Addition of seismic lines, oriented to intersect structures as close to orthogonal as possible, would likely help to accurately quantify the location and dip of the faults (e.g., Abbott, Louie, Caskey, & Pullammanappallil, 2001; Honjas et al., 1997; Louie et al., 2011). Detailed geologic mapping, already underway (B. Delwiche, 2013, personal communication), should also be expanded to 1) identify the stratigraphic distribution of the Tertiary volcanics, 2) accurately define fault attitudes and sense(s) of motion, and 3) more precisely determine structural relationships that may better constrain the timing and nature of Cenozoic extensional phases. Modernized two-meter temperature surveying may help to more robustly define the thermal outflow pattern (e.g., Skord et al., 2011). Some or all of these aspects ought to be pursued to decrease the risks and costs of exploratory drilling.

There are challenges specific to the Dixie Meadows geothermal prospect with respect to the above recommendations. The steep terrain in the Stillwater Mountains and the wetlands of the springs and the Humboldt Salt Marsh are difficult to negotiate by foot and by vehicle. Wilderness Study Area zonation in the Stillwater Mountains and around the Dixie Hot Springs prohibits vehicle and heavy equipment access. An active power line from the Dixie Valley power plant runs through the entire geothermal prospect. These obstacles will have to be overcome and/or reconciled in order to pursue further exploration on the prospect.

The methodologies and findings of this study are not unique to this geothermal prospect. Gravity and magnetic data are established methods for structural delineation and demarcation of potential geothermal targets. Detailed structural interpretation and geothermal targeting is not limited to locales containing fault/hydrothermal expressions at the surface; settings with little or no surface expressions are also attainable. Systems of interlinking rangefront, intra-basin, and piedmont faulting are being recognized at other Great Basin locales. Structural controls from faults associated with the HSZ found in this study are likely also manifested at other sites within this structural/geothermal belt. Inherited structure from previous episodes of extension in the Great Basin is a recognized phenomenon that appears to play a pivotal role in developing favorable structures that control geothermal systems. This work stands as but one case study to include in the broader context of using geophysical and geological methods in geothermal exploration, in order to identify the structural patterns that control hydrothermal fluid flow.

~

Appendix A: 1979 Shallow Temperature Survey Data

Station #	Easting (m)	Northing (m)	Elevation (m)	Date	Temperature (°C)
1	406241	4402325	1058.6	Jul-1979	26.0
2	405308	4400945	1048.1	Jul-1979	26.6
38	408167	4405671	1050.9	Jul-1979	36.2
39	408723	4406128	1045.6	Jul-1979	40.1
40	409308	4406416	1049.5	Jul-1979	28.2
41	409924	4406644	1044.2	Jul-1979	22.0
42	410659	4407140	1054.9	Jul-1979	26.2
43	411374	4407210	1050.3	Jul-1979	24.7
44	411989	4407845	1051.0	Jul-1979	25.5
45	412118	4408818	1057.5	Jul-1979	25.6
46	412128	4409890	1057.3	Jul-1979	25.4
47	412237	4410605	1052.7	Jul-1979	26.6
48	412575	4410903	1055.4	Jul-1979	26.4
50	413160	4412481	1043.1	Jul-1979	26.3
51	413498	4411409	1039.6	Jul-1979	24.5
52	413160	4411221	1046.4	Jul-1979	26.8
53	413121	4409602	1034.1	Jul-1979	22.8
54	413597	4409017	1030.1	Jul-1979	18.0
55	414044	4408560	1029.0	Jul-1979	27.3
56	412694	4409205	1041.9	Jul-1979	23.7
57	412833	4410655	1035.6	Jul-1979	18.4
126	413260	4410407	1032.1	Jul-1979	26.2
127	413766	4410089	1029.7	Jul-1979	26.0
128	413270	4407895	1033.8	Jul-1979	20.7
129	413766	4408103	1029.2	Jul-1979	16.8
130	412476	4407438	1038.6	Jul-1979	24.8
131	414411	4413722	1033.5	Jul-1979	23.9
132	415087	4413196	1030.7	Jul-1979	23.6
134	414431	4414606	1043.9	Jul-1979	26.7
137	415096	4414239	1030.9	Jul-1979	21.9
138	415543	4413981	1030.0	Jul-1979	23.5
142	413955	4413742	1046.9	Jul-1979	25.3
143	413518	4413971	1075.7	Jul-1979	28.3
144	413071	4414259	1111.3	Jul-1979	29.8
146	406400	4403020	1073.8	Jul-1979	28.4
147	406767	4403755	1073.3	Jul-1979	25.6
148	407124	4404519	1084.9	Jul-1979	31.2
149	407442	4405135	1070.7	Jul-1979	33.2
150	412605	4410089	1040.0	Jul-1979	25.1
184	412078	4409225	1053.3	Jul-1979	25.1
185	412297	4409622	1047.3	Jul-1979	24.6
186	411711	4408083	1069.3	Jul-1979	27.8
187	411612	4408163	1074.6	Jul-1979	27.9
188	411244	4408332	1094.7	Jul-1979	27.1
189	410947	4408530	1118.0	Jul-1979	26.3
190	410659	4408699	1136.1	Jul-1979	26.6
191	410520	4408798	1148.0	Jul-1979	26.3
192	411741	4408520	1074.4	Sep-1979	26.2
193	411671	4409116	1073.4	Sep-1979	24.7
194	411086	4408848	1114.7	Sep-1979	26.1
196	410698	4407925	1087.9	Jul-1979	26.3
230	408892	4406694	1073.3	Jul-1979	27.8
231	408385	4406624	1080.2	Sep-1979	33.8
232	408283	4406058	1055.5	Jul-1979	35.4
235	408018	4403934	1046.4	Jul-1979	31.0
236	407550	4403048	1041.9	Jul-1979	22.0
237	405635	4403477	1121.3	Sep-1979	26.2
238	406360	4404718	1127.5	Jul-1979	28.5
246	410559	4408034	1093.9	Jul-1979	26.2

Station numbers match those of Campana et al. (1980). Easting and northing coordinates are registered to UTM Zone 11N, WGS 84. Elevations were extracted from a 10 m digital elevation model. Data are primarily from July, but September data were inserted for stations missing July measurements.

~

Appendix B: Gravity and Magnetic Surveys – Principle Fact References

Principle facts for the gravity survey performed by Zonge Geosciences may be obtained with permission from Ormat Technologies. Ormat can be contacted at:

Ormat Technologies, Inc.

6225 Neil Road

Reno, Nevada 89511-1136
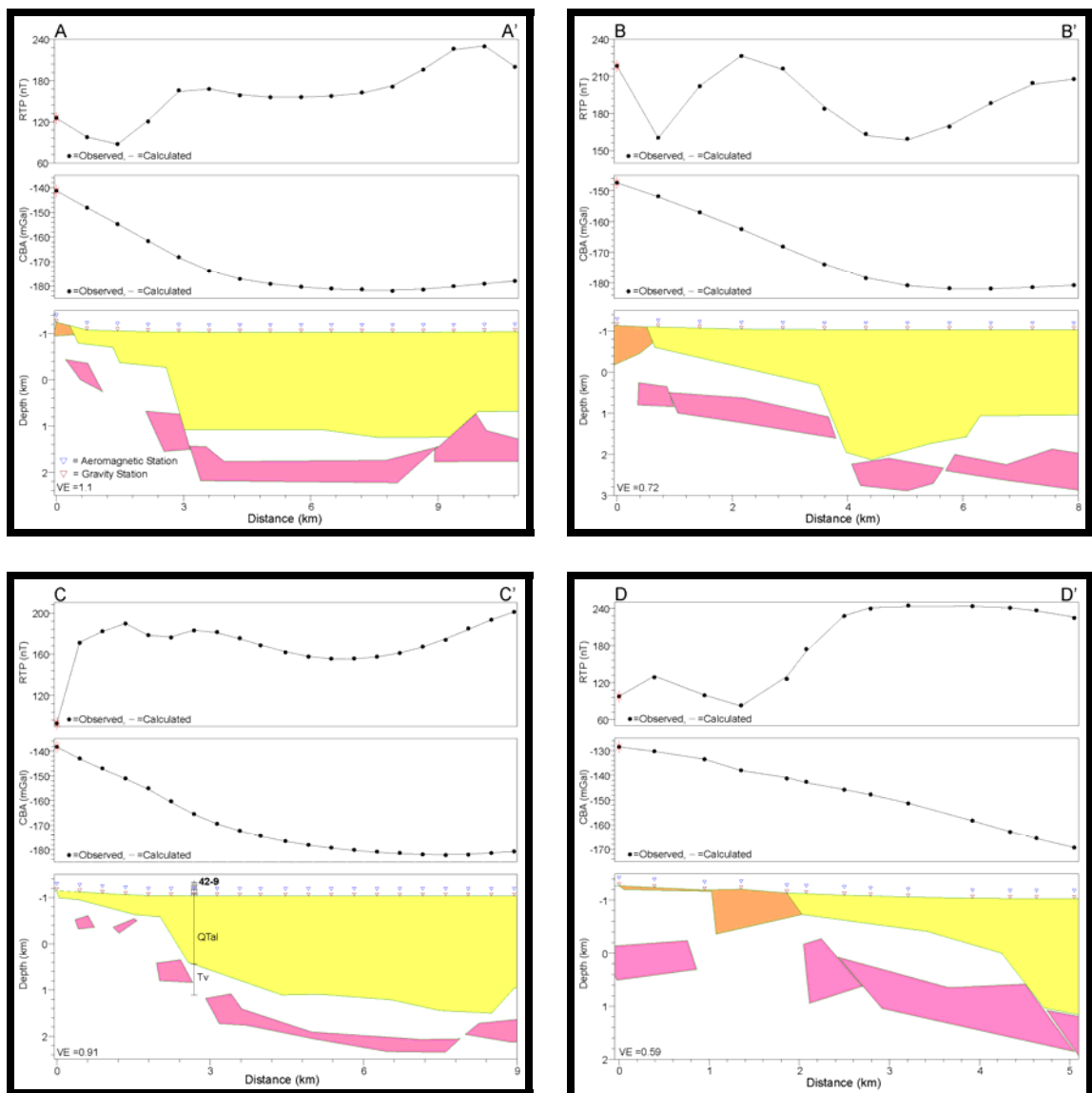
Tel: (775)356-9029

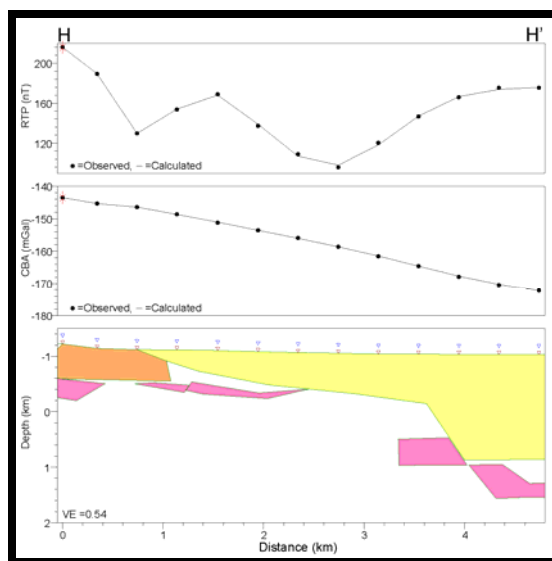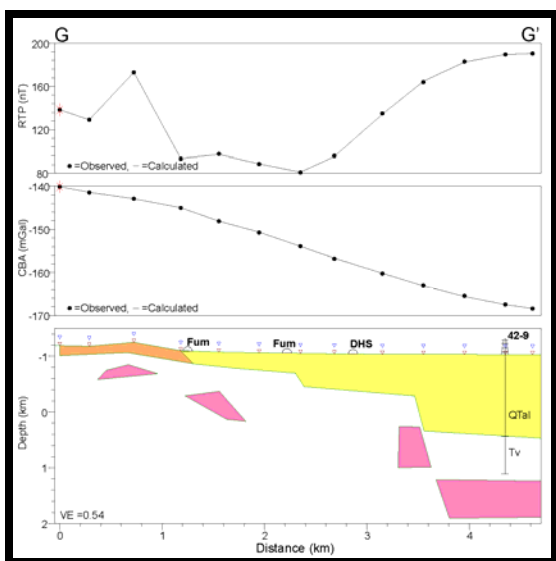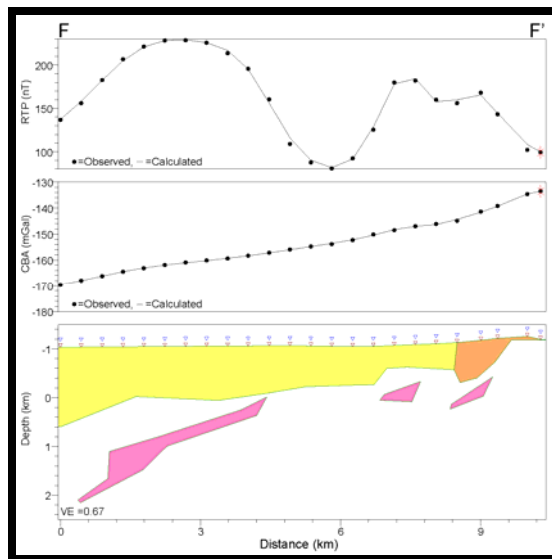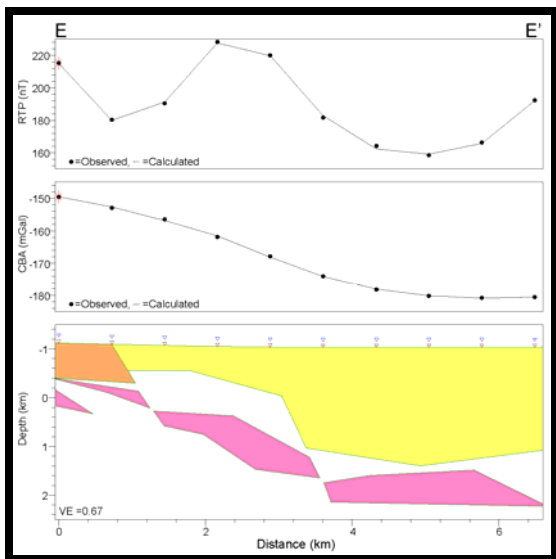Fax: (775)356-9039

Email: info@ormat.com

Principle facts for the magnetic survey performed by Pearson, deRidder, and Johnson are publically available from the U. S. Geological Survey website:
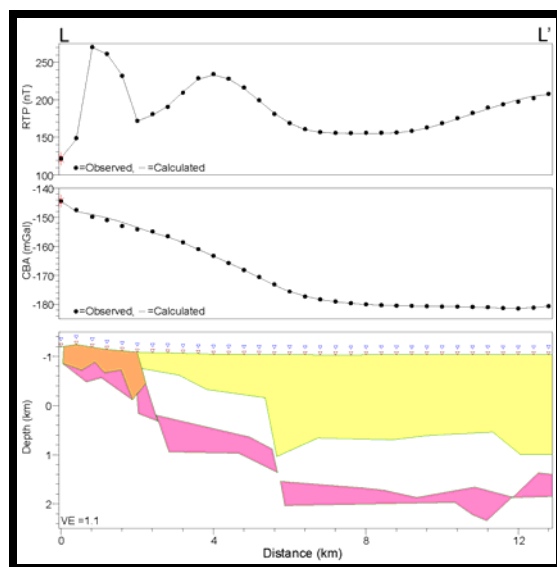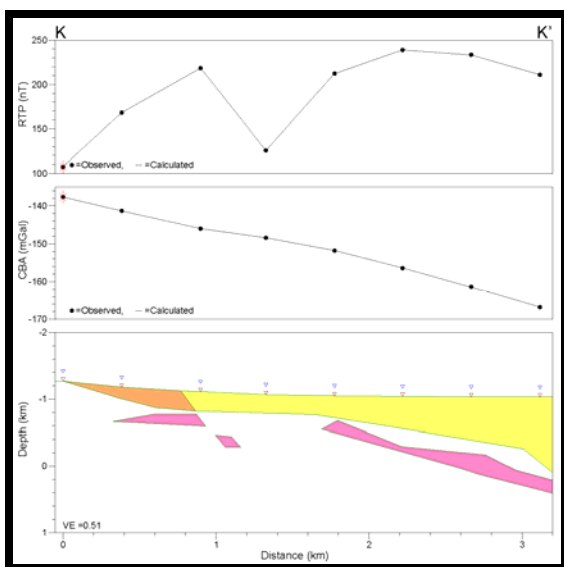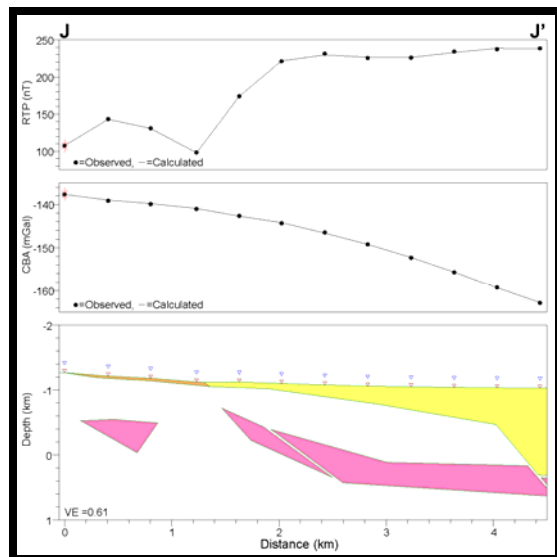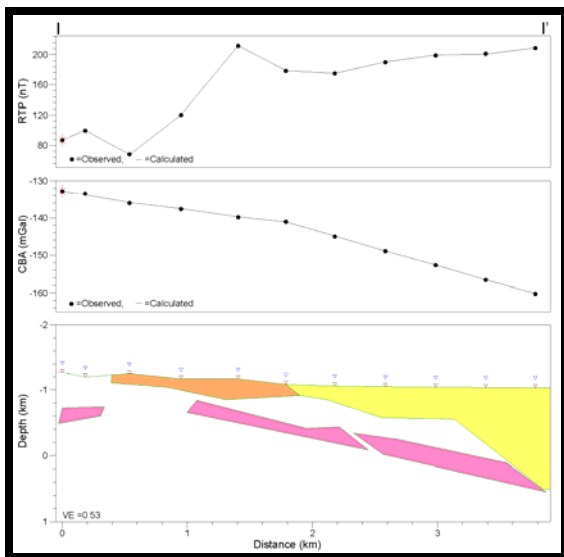
http://pubs.usgs.gov/of/2002/ofr-02-0374/

~

Appendix C: 2D Dual Model Profiles

References

Abbott, R.E., Louie, J.N., Caskey, S.J. and Pullammanappallil, S., 2001. Geophysical confirmation of low-angle normal slip on the historically active Dixie Valley fault, Nevada. Journal of Geophysical Research, 106(B3): 4169-4181.

Akima, H., 1970. A new method of interpolation and smooth curve fitting based on local procedures. Journal of the Association for Computing Machinary, 17(4): 589-602.

Baranov, V., 1957. A new method for interpretation of aeromagnetic maps: pseudo-gravimetric anomalies. Geophysics, 22(2): 359-383.

Bell, J.W., Caskey, S.J., Ramelli, A.R. and Guerrieri, L., 2004. Pattern and rates of faulting in the Central Nevada Seismic Belt, and paleoseismic evidence for prior beltlike behavior. Bulletin of the Seismological Society of America, 94(4): 1229-1254.

Bell, J.W. and Katzer, T., 1990. Timing of late Quaternary faulting in the 1954 Dixie Valley earthquake area, central Nevada. Geology, 18: 622-625.

Benoit, D., 1992. A case history of injection through 1991 at Dixie Valley, Nevada. Geothermal Resources Council Transactions, 16: 611-620.

Benoit, D., 1999. Conceptual models of the Dixie Valley, Nevada geothermal field. Geothermal Resources Council Transactions, 23: 505-511.

Blackwell, D.D., Smith, R.P. and Richards, M.C., 2007. Exploration and development at Dixie Valley, Nevada: Summary of DOE studies. Thirty-Second Workshop on Geothermal Reservoir Engineering Proceedings, SGP-TR-183: 1-16.

Blackwell, D.D., Wisian, K.W., Benoit, D. and Gollan, B., 1999. Structure of the Dixie Valley geothermal system, a "typical" Basin and Range geothermal system, from thermal and gravity data. Geothermal Resources Council Transactions, 23: 525-531.

Blakely, R.J., 1996. Potential Theory in Gravity & Magnetic Applications. Cambridge University Press, 464 pp.

Boden, D.R., 1986. Eruptive history and structural development of the Toquima caldera complex, central Nevada. Geological Society of America Bulletin, 97: 61-74.

Bohm, B.W., Jacobson, R.L., Campana, M.E. and Ingraham, N.L., 1980. Appendix F-1: Geothermal reservoir assessment case study, northern Basin and Range Province, northern Dixie Valley, Nevada; Chapter 5 - Hydrology and hydrogeochemistry, Mackay Minerals Research Institute, University of Nevada, Reno, Nevada.

Briggs, I.C., 1974. Machine contouring using minimum curvature. Geophysics, 39(1): 39-48.

Bruhn, D., Manzella, A., Vuataz, F., Faulds, J.E., Moeck, I. and Erbas, K., 2010. Chapter 2: Exploration methods. In: E. Huenges and P. Ledru (Editors), Geothermal Energy Systems: Exploration, Development, and Utilization. John Wiley & Sons Ltd., pp. 37-112.

Calder, C. and Cressie, N.A., 2009. Kriging and variogram models. In: R. Kitchin and N. Thrift (Editors), International Encyclopedia of Human Geography. Elsevier, Oxford, pp. 49-55.

Campana, M.E., Jacobson, R.L. and Ingraham, N.L., 1980. Appendix F-1: Geothermal reservoir assessment case study, northern Basin and Range Province, northern

Dixie Valley, Nevada; Chapter 6 - Shallow temperature survey, Mackay Minerals Research Institute, University of Nevada, Reno, Nevada.

Caskey, S.J. and Wesnousky, S.G., 2000. Active faulting and stress redistributions in the Dixie Valley, Beowawe, and Bradys geothermal fields: implications for geothermal exploration in the Basin and Range. Twenty-Fifth Workshop on Geothermal Reservoir Engineering Proceedings, SGP-TR-165: 1-16.

Caskey, S.J., Wesnousky, S.G., Zhang, P. and Slemmons, D.B., 1996. Surface faulting of the 1954 Fairview Peak (M_S 7.2) and Dixie Valley (M_S 6.8) earthquakes, central Nevada. Bulletin of the Seimological Society of America, 86(3): 761-787.

Chaodong, F., Peng, Y. and Bo, X., 2010. Rapid geological modeling by using implicit 3D potential field interpolation method, International Conference on Computer Design and Applications, pp. 50-53.

Colgan, J.P., Dumitru, T.A. and Miller, E.L., 2004. Diachroneity of Basin and Range extension and Yellowstone hotspot volcanism in northwestern Nevada. Geology, 32(2): 121-124.

Coolbaugh, M.F., Raines, G.L., Zehner, R.E., Shevenell, L. and Williams, C.F., 2006. Prediction and discovery of new geothermal resources in the Great Basin: multiple evidence of a large undiscovered resource base. Geothermal Resources Council Transactions, 30: 867-873.

Deino, A.L., 1989. Single crystal ^{40}Ar/^{39}Ar dating as an aid in correlation of ash flows: examples from the Chimney Springs/New Pass Tuffs and the Nine Hill/Bates Mountain Tuffs of California and Nevada. New Mexico Bureau of Mines and Mineral Resources: Continental Magmatism Abstracts Bulletin, 131: 70.

Devriese, S.G.R., Oldenburg, D.W. and Shoffner, J.D., 2012. Three-dimensional inversion of ZTEM data at the Eleven Mile Canyon geothermal system, Nevada. Geothermal Resources Council Transactions, 36: 995-999.

Dilek, Y. and Moores, E.M., 1995. Geology of the Humboldt igneous complex, Nevada, and tectonic implications for the Jurassic magmatism in the Cordilleran orogen. Geological Society of America Special Paper, 299: 229-248.

Doser, D.I., 1986. Earthquake processes in the Rainbow Mountain-Fairview Peak-Dixie Valley, Nevada, Region 1954-1959. Journal of Geophysical Research, 91(B12): 12572-12586.

Edmiston, R.C. and Benoit, D., 1984. Characteristics of Basin and Range geothermal systems with fluid temperatures of 150°C to 200°C. Geothermal Resources Council Transactions, 8: 417-424.

Faulds, J.E., Coolbaugh, M., Blewitt, G. and Henry, C.D., 2004. Why is Nevada in hot water? Structural controls and tectonic model of geothermal systems in the northwestern Great Basin. Geothermal Resources Council Transactions, 28: 649-654.

Faulds, J.E., Garside, L.J. and Oppliger, G.L., 2003. Structural analysis of the Desert Peak-Brady geothermal fields, northwestern Nevada: implications for understanding linkages between northeast-trending structures and geothermal reservoirs in the Humboldt Structural Zone. Geothermal Resources Council Transactions, 27: 859-864.

Faulds, J.E., Hinz, N.H., Coolbaugh, M.F., Cashman, P.H., Kratt, C., Dering, G., Edwards, J., Mayhew, B. and McLachlan, H., 2011. Assessment of favorable

structural settings of geothermal systems in the Great Basin, Western USA. Geothermal Resources Council Transactions, 35: 777-783.

Fosdick, J.C. and Colgan, J.P., 2008. Miocene extension in the East Range, Nevada: a two-stage history of normal faulting in the northern Basin and Range. Geological Society of America Bulletin, 120(9/10): 1198-1213.

Goff, F., Bergfield, D., Janik, C.J., Counce, D. and Murrell, M., 2002. Geochemical data on waters, gases, scales, and rocks from the Dixie Valley region, Nevada (1996-1999), Los Alamos National Laboratory.

Grauch, V.J.S., 2002. High-resolution aeromagnetic survey to image shallow faults, Dixie Valley geothermal field, Nevada, U.S. Geological Survey.

Gromme, C.S., McKee, E.H. and Blake Jr., M.C., 1972. Paleomagnetic correlations and potassium-argon dating of middle Tertiary ash-flow sheets in the eastern Great Basin, Nevada and Utah. Geological Society of America Bulletin, 83: 1619-1638.

Hammond, W.C., Blewitt, G. and Kreemer, C., 2011. Block modeling of crustal deformation of the northern Walker Lane and Basin and Range from GPS velocities. Journal of Geophysical Research, 116(B04402): 1-28.

Hammond, W.C. and Thatcher, W., 2004. Contemporary tectonic deformation of the Basin and Range province, western United States: 10 years of observation with the Global Positioning System. Journal of Geophysical Research, 109(B08403): 1-21.

Henley, R.W., 1985. The geothermal framework of epithermal deposits. Reviews in Economic Geology, 2: 1-24.

Henry, C.D. and Faulds, J.E., 2010. Ash-flow tuffs in the Nine Hill, Nevada, paleovalley and implications for tectonism and volcanism of the western Great Basin, USA. Geosphere, 6(4): 339-369.

Henry, C.D., Faulds, J.E., dePolo, C.M. and Davis, D.A., 2004. Geology of the Dogskin Mountain quadrangle, northern Walker Lane, Nevada, Nevada Bureau of Mines and Geology Maps.

Henry, C.D. and John, D.A., 2013. Magmatism, ash-flow tuffs, and calderas of the ignimbrite flareup in the western Nevada volcanic field, Great Basin, USA. Geosphere, in review.

Hickman, S., Zoback, M. and Benoit, D., 1998. Tectonic controls on reservoir permeability in the Dixie Valley, Nevada, geothermal field. Twenty-Third Workshop on Geothermal Reservoir Engineering Proceedings, SGP-TR-158: 291-298.

Honjas, W., Pullammanappallil, S.K., Lettis, W.R., Plank, G.L., Louie, J.N. and Schweichert, R., 1997. Predicting subsurface structure within the Dixie Valley geothermal field, Dixie Valley, Nevada, using a non-linear optimization scheme. Geothermal Resources Council Bulletin, 26: 45-52.

Hudson, M.R. and Geissman, J.W., 1991. Paleomagnetic evidence for the age and extent of middle Tertiary counterclockwise rotation, Dixie Valley region, west central Nevada. Journal of Geophysical Research, 96(B3): 3979-4006.

Iovenitti, J., Blackwell, D.D., Sainsbury, J., Tibuleac, I., Waibel, A.F., Cladouhos, T., Karlin, R.E., Isaaks, E., Clyne, M., Ibser, F.H., Callahan, O., Kennedy, B.M. and Wannamaker, P.E., 2012. Towards developing a calibrated EGS exploration

methodology using the Dixie Valley geothermal system, Nevada. Thirty-Seventh Workshop on Geothermal Reservoir Engineering Proceedings, SGP-TR-194: 1-15.

Iovenitti, J., Sainsbury, J., Tibuleac, I., Karlin, R.E., Wannamaker, P.E., Maris, V., Blackwell, D.D., Thakur, M., Ibser, F.H., Lewicki, J., Kennedy, B.M. and Swyer, M., 2013. EGS exploration methodology project using the Dixie Valley geothermal system, Nevada, status update. Thirty-Eighth Workshop on Geothermal Reservoir Engineering Proceedings, SGP-TR-198: 1-10.

John, D.A., 1995. Tilted middle Tertiary ash-flow calderas and subadjacent granitic plutons, southern Stillwater Range, Nevada: cross sections of an Oligocene igneous center. Geological Society of America Bulletin, 107(2): 180-200.

John, D.A., Thomason, R.E. and McKee, E.H., 1989. Geology and K-Ar geochronology of the Paradise Peak Mine and the relationship of pre-Basin and Range extension to early Miocene precious metal mineralization in west-central Nevada. Economic Geology, 84: 631-649.

Kennedy-Bowdoin, T., Silver, E.A., Martini, B.A. and Pickles, W.L., 2004. Geothermal prospecting using hyperspectral imaging and field observations, Dixie Meadows, NV, Lawrence Livermore National Laboratory, UCRL-CONF-204141.

Lamb, A.K., Kratt, C. and Calvin, W.M., 2011. Geothermal exploration using hyperspectral analysis over Dixie and Fairview Valleys, Nevada. Geothermal Resources Council Transactions, 35: 867-871.

Louie, J.N., Pullammanappallil, S.K. and Honjas, W., 2011. Advanced seismic imaging for geothermal development. New Zealand Geothermal Workshop Proceedings: 1-7.

Lutz, S.J., Caskey, S.J., Mildenhall, D.D., Browne, P.R.L. and Johnson, S.D., 2002. Dating sinter deposits in northern Dixie Valley, Nevada - the paleoseismic record and implications for the Dixie Valley geothermal system. Twenty-Seventh Workshop on Geothermal Reservoir Engineering Proceedings, SGP-TR-171: 1-14.

Lutz, S.J., Moore, J.N. and Benoit, D., 1997. Geologic framework of Jurassic reservoir rocks in the Dixie Valley geothermal field, Nevada: implications from hydrothermal alteration and stratigraphy. Twenty-Second Workshop on Geothermal Reservoir Engineering Proceedings, SGP-TR-155: 131-139.

Mankhemthong, N., 2008. Structure of the Inter-Basin Transition Zone between Dixie Valley and Fairview Valley, Nevada, USA, Thesis: University of Nevada - Reno, 120 pp.

McKee, E.H. and Stewart, J.H., 1971. Stratigraphy and potassium-argon ages of some Tertiary tuffs from Lander and Churchill Counties, central Nevada. U.S. Geological Survey Bulletin, 1311-B: B1-B128.

Nettleton, L.L., 1939. Determination of density for reduction of gravimeter observations. Geophysics, 4(3): 176-183.

Page, B.M., 1935. Basin-range faulting of 1915 in Pleasant Valley, Nevada. The Journal of Geology, 43(7): 690-707.

Page, B.M., 1965. Preliminary geologic map of a part of the Stillwater Range, Churchill County, Nevada, Nevada Bureau of Mines.

Proffett Jr., J.M., 1977. Cenozoic geology of the Yerington district, Nevada, and implications for the nature and origin of Basin and Range faulting. Geological Society of America Bulletin, 88: 247-266.

Rowan, L.C. and Wetlaufer, P.H., 1981. Relation between regional lineament systems and structural zones in Nevada. American Association of Petroleum Geologists Bulletin, 65(8): 1414-1432.

Sawyer, T.L. and Anderson, R.E., 1999. Fault numbers 1687a and 1687b, Dixie Valley fault zone. Quaternary fault and fold database of the United States: U.S. Geological Survey website, *http://earthquakes.usgs.gov/hazards/qfaults*.

Schaefer, D.H., 1983. Gravity survey of Dixie Valley, west-central Nevada, U.S. Geological Survey.

Schwering, P.C. and Karlin, R.E., 2012. Structural interpretation and modeling of the Dixie Meadows geothermal prospect using gravity and magnetic data, Abstract V13A-2811, American Geophysical Union.

Silberling, N.J. and Roberts, R.J., 1962. Pre-Tertiary stratigraphy and structure of northwestern Nevada. Geological Society of America Special Paper, 72: 1-58.

Skalbeck, J.D., Karlin, R.E., Shevenell, L. and Widmer, M.C., 2002. Geothermal reservoir volume estimation from gravity and aeromagnetic modeling of the Steamboat Hills geothermal area, Reno, Nevada. Geothermal Resources Council Transactions, 26: 443-448.

Skalbeck, J.D., Karlin, R.E., Shevenell, L. and Widmer, M.C., 2005. Gravity and aeromagnetic modeling of alluvial basins in the southern Truckee Meadows adjacent to the Steamboat Hills geothermal area, Washoe County, Nevada. Geophysics, 70(3): B1-B9.

Skord, J., Sladek, C., Coolbaugh, M.F., Cashman, P.H., Lazaro, M. and Kratt, C., 2011. Two-meter temperature surveys for geothermal exploration project at NAS Fallon. Geothermal Resources Council Transactions, 35: 1023-1027.

Slemmons, D.B., 1957. Geological effects of the Dixie Valley-Fairview Peak, Nevada, earthquakes of December 16, 1954. Bulletin of the Seismological Society of America, 47(4): 353-375.

Smith, R.P., Grauch, V.J.S. and Blackwell, D.D., 2002. Preliminary results of a high-resolution aeromagnetic survey to identify buried faults at Dixie Valley, Nevada. Geothermal Resources Council Transactions, 26: 543-546.

Smith, R.P., Wisian, K.W. and Blackwell, D.D., 2001. Geologic and geophysical evidence for intra-basin and footwall faulting at Dixie Valley, Nevada. Geothermal Resources Council Transactions, 25: 323-326.

Speed, R.C., 1976. Geologic map of the Humboldt Lopolith and surrounding terrane, Nevada, Geological Society of America Map and Chart Series.

Stockli, D.F., 1999. Regional Timing and Spatial Distribution of Miocene Extension in the Northern Basin and Range Province, Dissertation: Stanford University, 239 pp.

Surpless, B.E., Stockli, D.F., Dumitru, T.A. and Miller, E.L., 2002. Two-phase westward encroachment of Basin and Range extension into the northern Sierra Nevada. Tectonics, 21(1): 1-13.

Tester, J.W., Anderson, B.J., Batchelor, A.S., Blackwell, D.D., DiPippo, R., Drake, E.M., Garnish, J., Livesay, B., Moore, M.C., Nichols, K., Petty, S., Toksoz, M.N. and Veatch Jr., R.W., 2006. The furture of geothermal energy: impact of enhanced geothermal systems (EGS) on the United States in the 21st century, Massachusetts Institute of Technology.

Thompson, G.A. and Burke, D.B., 1973. Rate and direction of spreading in Dixie Valley, Basin and Range Province, Nevada. Geological Society of America Bulletin, 84: 627-632.

Vikre, P.G., 1994. Gold mineralization and fault evolution at the Dixie Comstock Mine, Churchill County, Nevada. Economic Geology, 89(4): 707-719.

Waibel, A.F., 1987. An overview of the geology and secondary mineralogy of the high temperature geothermal system in Dixie Valley, Nevada. Geothermal Resources Council Transactions, 11: 479-486.

Wallace, R.E., 1984. Fault scarps formed during the earthquakes of October 2, 1915, in Pleasant Valley, Nevada, and some tectonic implications.

Wallace, R.E. and Whitney, R.A., 1984. Late Quaternary history of the Stillwater Seismic Gap, Nevada. Bulletin of the Seismological Society of America, 74(1): 301-314.

Wannamaker, P.E., Doerner, W.M. and Hasterok, D.P., 2007. Integrated dense array and transect MT surveying at Dixie Valley geothermal area, Nevada; structural

controls, hydrothermal alteration and deep fluid sources. Thirty-Second Workshop on Geothermal Reservoir Engineering Proceedings, SGP-TR-183: 1-6.

Wannamaker, P.E., Maris, V., Sainsbury, J. and Iovenitti, J., 2013. Intersecting fault trends and crustal-scale fluid pathways below the Dixie Valley geothermal area, Nevada, inferred from 3D magnetotelluric surveying. Thirty-Eighth Workshop on Geothermal Reservoir Engineering Proceedings, SGP-TR-198: 1-9.

Watts, S.S., 2010. Contrasting Paleo-Seismically Induced Lateral Spreading Mechanisms and Geomorphologies in Dixie Valley, NV - A Geotechnical Analysis, Dissertation: University of Nevada – Reno, 261 pp.

Willden, R. and Speed, R.C., 1974. Geology and mineral deposits of Churchill County, Nevada, Nevada Bureau of Mines and Geology, Mackay School of Mines.

Zoback, M., 1999. Fracture permeability and in situ stress in the Dixie Valley, Nevada, geothermal reservoir, Department of Geophysics, Stanford University, Stanford, California.

~